Modeling Reaction and Transport Effects in Stereolithographic 3D Printing

by

Zachary D. Pritchard

A dissertation submitted in partial fulfillment
of the requirements for the degree of
Doctor of Philosophy
(Chemical Engineering)
in The University of Michigan
2020

Doctoral Committee:

Professor Mark A. Burns, Chair
Professor Ronald G. Larson
Associate Professor Sunitha Nagrath
Professor Albert Shih

Science is magic that works

—Kurt Vonnegut, *Cat's Cradle*

Tiger got to hunt, bird got to fly;
Man got to sit and wonder "why, why, why?"
Tiger got to sleep, bird got to land;
Man got to tell himself he understand.

—Kurt Vonnegut, *Cat's Cradle*

Zachary D. Pritchard

zdpritch@umich.edu

ORCID iD: 0000-0003-2610-4636

ACKNOWLEDGEMENTS

This work was only possible thanks to a lifetime of support from family and friends. I am immeasurably grateful to my parents, who got me to where I am today, and to my wife for seven great years together (and counting!).

I am also thankful to my advisor, Prof. Mark Burns, for his patience as I found my way to a research topic that I enjoyed, to my many labmates over the years for their advice and companionship, and to the department administrative staff for doing so much behind-the-scenes work to support graduate students.

While I want to avoid listing all of my friends individually (sorry!), I would be remiss not to directly acknowledge the contributions of my friend and labmate Martin de Beer. While I like to think I would have some sort of dissertation if I hadn't had the opportunity to work with Martin, it would undoubtedly look nothing like the one in front of you now. Martin's influence on the trajectory of my Ph.D. is undeniable and will always be appreciated.

Finally (at the risk of sounding like *Time* circa 2006), thank *you*, dear reader. Mark told me many times that no one reads dissertations, and every graduate student occasionally likes to see their advisor proven wrong.

TABLE OF CONTENTS

ACKNOWLEDGEMENTS . . . . . **ii**

LIST OF FIGURES . . . . . **v**

LIST OF APPENDICES . . . . . **xi**

LIST OF TABLES . . . . . **xii**

ABSTRACT . . . . . **xiii**

CHAPTER

I. Introduction 1

1.1 Stereolithography in Additive Manufacturing 1
1.2 Dual-Wavelength Continuous Stereolithography 2
1.3 Modelling Reaction and Transport Effects in Stereolithographic 3D Printing 5

II. Modelling and Correcting Cure-Through in Continuous Stereolithographic 3D Printing 7

2.1 Introduction 7
2.2 Materials and Methods 9
2.2.1 Modeling and Correction 9
2.2.2 3D Printing 12
2.3 Results and Discussion 14
2.3.1 Dose-Based Correction for Continuous 3D-Printing 14
2.3.2 Experimental Validation 22
2.4 Conclusion 24

III. Kinetic Curing Model for Uninhibited and Photoinhibited Stereolithography 25

3.1 Introduction 25
3.2 Materials and Methods 28
3.2.1 Materials 28
3.2.2 Exposure Setup 29
3.2.3 Cured Height Experiments 30
3.2.4 Dead Zone Experiments 30
3.3 Model Development 31
3.3.1 Uninhibited Curing Model 31
3.3.2 Photoinhibited Curing Model 35
3.4 Results and Discussion 38
3.4.1 Commercial Resins for Layer-by-Layer Projection Stereolithography 38

3.4.2 Custom Resins for Photoinhibited Continuous Stereolithography . 42
3.5 Conclusion . . . 49

IV. Resin Flow and Dead Zone Uniformity in Photoinhibited Continuous Stereolithography . . . 51

4.1 Introduction . . . 51
4.2 Model Description . . . 53
4.2.1 Model Geometry and Material Properties . . . 53
4.2.2 Resin Curing . . . 56
4.2.3 Resin Flow . . . 57
4.3 Results and Discussion . . . 58
4.3.1 Time-Dependent Print Modelling . . . 58
4.3.2 Intensity Optimization . . . 63
4.4 Conclusion . . . 69

V. Conclusions and Continuing Work . . . 71

5.1 Conclusions . . . 71
5.2 Continuing Work . . . 75
5.2.1 Reciprocity Law in Projection Stereolithography . . . 75
5.2.2 Dead Zone Control in Dual-Wavelength Continuous Stereolithography . . . 76
5.2.3 Unified Models for Dual-Wavelength Continuous Stereolithography 76

APPENDICES . . . **77**

BIBLIOGRAPHY . . . **111**

LIST OF FIGURES

Figure

1.1 **(a)** In dual-wavelength continuous stereolithography, a dead zone is generated near the window using orthogonal initiation and inhibition photochemistries. Blue light drives polymerization, while UV light inhibits it. **(b)** Absorbance spectra of 0.4 wt.% CQ and EDAB (initiator and co-initiator) and 0.06 wt.% *o*-Cl-HABI (inhibitor) in tetrahydrofuran (THF). The emission wavelength of the initiating and inhibiting light sources used in experiments are shown in with shaded blue and purple boxes. 4

2.1 **(a)** Cure-through correction is incorporated into the 3D printing workflow by computationally processing slice images. **(b–c)** Correction applied to real models, reducing the extent of cure-through while maintaining print speed. Scale bars are 5 mm. **(b)** #3DBenchy [53] printed at $800\,\mathrm{mm\,h^{-1}}$ (h_a = 1,500 µm, D_c = $230\,\mathrm{mJ\,cm^{-3}}$), and **(c)** hollow egg [54] printed at $800\,\mathrm{mm\,h^{-1}}$ (h_a = 2,000 µm, $D_\mathrm{c} = 173\,\mathrm{mJ\,cm^{-3}}$). **(d)** Vertical cross-section of printer setup showing nondimensionalized variables of interest: ζ, Ω_n, and Φ_n are the dimensionless z-position, dose, and light intensity, respectively. 10

2.2 Model results for uncorrected slices. **(a)** Test model. **(b)** Vertical stack of uncorrected grayscale projections along the plane indicated in (a). Note that only black and white ($p = 0$ and $p = 1$) are used by default. **(c)** Model prediction from slices in (b) showing areas with cure-through (*CT*, red) and undercuring (*UC*, blue). Gray regions of the part are correctly cured (*CC*, gray). **(d)** Grayscale value as a function of n and total accumulated dose as a function of ζ for the (x, y) position indicated by the dashed line in (a). $D_\mathrm{c} = 576\,\mathrm{mJ\,cm^{-3}}$, $h_\mathrm{s} = 50$ µm, $h_\mathrm{a} = 2{,}000$ µm, and $s = 1{,}000\,\mathrm{mm\,h^{-1}}$. $\zeta = 0$ corresponds to the top of the part (i.e., the surface attached to the build platform). The grayscale value p relates to the intensity of the projected pixel when $\zeta_\mathrm{w} = n$ (calibration curve in Figure A.1). Shaded areas indicate designed features. The dose curve indicates the normalized total dose Ω_T at position ζ on completion of the print, with cure errors indicated in red (cure-through) or blue (undercure). **(e)** Evolution of the total dose curve shown in (d) for n = 21 to = 50. The total dose is the sum of contributions from individual slices, each labeled and represented by a color. 17

2.3 Target dose region and dose profiles. **(a)** Three constraints which define the target dose region (shaded): *(i)* curing of features while non-features remain uncured, *(ii)* exposure at the maximum dose at the bottom of the feature, and *(iii)* exposure at the minimum dose at the top of the feature. **(b)** Valid dose profiles defined by maximum dose Ω_max with corresponding intensity profiles. Here, shading indicates the designed feature height. For a given set of parameters, the intensity profile can be tailored to achieve either a uniform dose or a high peak dose within features while still eliminating cure errors. 19

2.4 Correction for model in Figure 2.2(a) with $\Omega_{\max} = 1$. **(a)** Vertical stack of corrected grayscale projections along the plane indicated in Figure 2.2(a). **(b)** Model prediction from slices in (a) showing no cure-through (*CT*, red) or undercure (*UC*, blue). The full part is correctly cured (*CC*, gray). **(c)** Corrected grayscale value and dose for the (x, y) position indicated by the dashed line in Figure 2.2(a). Note that the correction process required additional slices beyond the original 50 to ensure the bottom of the part was fully cured. $D_c = 576\,\mathrm{mJ\,cm^{-3}}$, $h_s = 50\,\mu\mathrm{m}$, $h_a = 2{,}000\,\mu\mathrm{m}$, and $s = 1{,}000\,\mathrm{mm\,h^{-1}}$. **(d)** Contributions of individual slices to the accumulated dose curve shown in (c) for $n = 21$ to $n = 53$. 21

2.5 Experimental tuning of correction parameters. **(a)** Cured thickness versus exposure dose of blue light for two acrylate-based resins (see Table 2.1) with differing concentrations of blue light absorber. **(b)** Test model (left), uncorrected test part (center), and corrected test part printed with $D_c = 5D_{gel} = 325\,\mathrm{mJ\,cm^{-3}}$ (right). Parts printed in Resin 1 at $750\,\mathrm{mm\,h^{-1}}$. **(c)** Ratio of height errors (corrected-to-uncorrected) for a range of feature sizes and values of D_c. A ratio of zero corresponds to a perfectly corrected feature. **(d)** Parts printed at $750\,\mathrm{mm\,h^{-1}}$ using slices corrected with different values for D_c. **(e)** Corrected and uncorrected test parts for two resins with different absorber loadings (i.e., h_a) and print speeds. All scale bars are 10 mm. 23

3.1 Uninhibited and photoinhibited projection stereolithography. **(a)** General printer configuration for projection stereolithography, **(b)** In standard, uninhibited stereolithography, resin in the gap between the part and the window is cured to form discrete layers. **(c)** In dual-wavelength continuous stereolithography, a dead zone is generated near the window, preventing polymerization. As a result, resin cures from the part downward and continuous printing is enabled. **(d)** Absorbance spectra of custom resin components diluted in tetrahydrofuran (THF) to concentrations, in wt.%, of 25, 6, 0.4, 0.06, and 2.3×10^{-4} for HDDA, CN991, CQ+EDAB, *o*-Cl-HABI, and Epolight 5675 respectively. The emission wavelength of the initiating and inhibiting light sources used in experiments are shown in with shaded blue and purple boxes. 32

3.2 Comparing cured height results and model fitting for two hypothetical resins: one where the reciprocity assumption is valid and one where it is not. 39

3.3 Characterization of commercial resins. Each plot shows cured height as a function of incident dose (standard optical dose D for the Jacobs model and the dose analogue D' for the kinetic model). Parameters were fit using a least-squares regression. For Formlabs Standard Clear, the Jacobs model parameters are $D_c = 223\,\mathrm{mJ\,cm^{-2}}$ and $h_a = 260\,\mu\mathrm{m}$ ($R^2 = 0.992$). The kinetic model parameters are $D'_c = 148\,(\mathrm{mW\,cm^{-2}})^{0.91}\,\mathrm{s}$, $h_a = 238\,\mu\mathrm{m}$, and $m = 0.91$ ($R^2 = 0.994$). For MakerJuice Standard Yellow, the Jacobs model parameters are $D_c = 69\,\mathrm{mJ\,cm^{-2}}$ and $h_a = 170\,\mu\mathrm{m}$ ($R^2 = 0.983$), and the kinetic model parameters are $D'_c = 67\,(\mathrm{mW\,cm^{-2}})^{0.99}\,\mathrm{s}$, $h_a = 168\,\mu\mathrm{m}$, and $m = 0.99$ ($R^2 = 0.983$). For CPS PR57 Black, the Jacobs model parameters are $D_c = 82\,\mathrm{mJ\,cm^{-2}}$ and $h_a = 92\,\mu\mathrm{m}$ ($R^2 = 0.994$), and the kinetic model parameters are $D'_c = 117\,(\mathrm{mW\,cm^{-2}})^{1.07}\,\mathrm{s}$, $h_a = 99\,\mu\mathrm{m}$, and $m = 1.07$ ($R^2 = 0.996$). 41

3.4 Development of the curing front over time and the effect of blue intensity, blue absorbance height, UV intensity, and UV absorbance height. **(a)** Diagram showing cured part growth over time with the initiation point z_0, the backside curing front z_b, and the frontside curing front z_f indicated. **(b)** Plot of cured part growth over time. The curve itself traces the movement of the curing front, while the area inside the curve (shaded in this plot) represents cured resin. After a brief period, the frontside curing front z_f tends towards the steady-state dead zone height $z_{f,\infty}$ while the backside curing front z_b tends towards the solution from the uninhibited model. Remaining plots show the effect of **(c)** blue intensity, **(d)** blue absorbance height, **(e)** UV intensity, and **(f)** UV absorbance height on the curing front. Parameters other than the variable of interest are held constant at $I_b = 100\,\mathrm{mW\,cm^{-2}}$, $h_b = 750\,\mu\mathrm{m}$, $I_{uv} = 200\,\mathrm{mW\,cm^{-2}}$, $h_{uv} = 100\,\mu\mathrm{m}$, $\beta = 1$, $m = 1$, and $D'_c = 100\,\mathrm{mJ\,cm^{-2}}$. 43

3.5 Steady-state dead zone height (Equation 3.25) and the effect of **(a)** UV/blue intensity ratio, **(b)** blue absorbance height, and **(c)** UV absorbance height. Parameters other than the variable of interest are held constant at $I_{uv}/I_b = 2$, $h_b = 750\,\mu\mathrm{m}$, and $h_{uv} = 100\,\mu\mathrm{m}$. For (b) and (c), red dashed line indicates the asymptotic limit at which $h_b = h_{uv}$. 44

3.6 Effect of independent intensities at constant intensity ratio. Other parameters are held constant at $h_b = 750\,\mu\mathrm{m}$, $h_{uv} = 100\,\mu\mathrm{m}$, $\beta = 1$, $m = 1$, and $D' = 100\,\mathrm{mJ\,cm^{-2}}$. **(a)** The development of the curing front is significantly affected by the blue intensity, even at constant intensity ratio. **(b)** Time to the initiation point as a function of blue intensity at constant intensity ratio. **(c)** Time for z_b to reach 90% of the uninhibited solution at varying blue intensity and constant intensity ratio. **(d)** Time for z_f to reach 110% of $z_{f,\infty}$ at varying blue intensity and constant intensity ratio. $I_{uv}/I_b = 1$ is not visible since no dead zone exists for $\beta I_{uv}/I_b \leq 1$. 45

3.7 Characterization of custom resins for dual-wavelength continuous stereolithography (see Table 3.1 for compositions). **(a)** Cured height as a function of incident dose for Resin 1. A least-squares fit yielded the parameters $D'_c = 64\,(\mathrm{mW\,cm^{-2}})^{0.99}\,\mathrm{s}$, $h_b = 408\,\mu\mathrm{m}$, and $m = 0.99$ ($R^2 = 0.985$). **(b)** Dead zone height as a function of intensity ratio for Resin 1. The exposure time was 30 s, and the data was correspondingly fit to the steady-state dead zone equation, yielding the parameters $\beta = 0.73$ and $h_{uv} = 37.8\,\mu\mathrm{m}$ ($R^2 = 0.902$). **(c)** Cured height for Resin 2, with the parameters $D'_c = 238\,(\mathrm{mW\,cm^{-2}})^{1.03}\,\mathrm{s}$, $h_b = 1{,}631\,\mu\mathrm{m}$, and $m = 1.03$ ($R^2 = 0.958$). **(d)** Dead zone height at 15 s for Resin 2 with time-dependent model fit, with the parameters $\beta = 4.84$, $h_{uv} = 100\,\mu\mathrm{m}$, and $m = 1.29$ ($R^2 = 0.980$). 48

4.1 **(a)** Diagram of dual-wavelength continuous stereolithography. A resin bath filled with photopolymer resin is simultaneously exposed to blue and UV light, which respectively initiate and inhibit polymerization. The build platform ascends as cross-sections of the part are continuously exposed and cured. Dashed lines indicate the regions of the resin bath that are included in each COMSOL geometry. **(b)** Geometry for the time-dependent, axisymmetric model. **(c)** Geometry for the steady-state, axisymmetric model, which is used for intensity optimization. 54

4.2 Representative flow profile for printing of a 2 mm radius cylinder at $300\,\mathrm{mm\,h^{-1}}$. **(a)** View of resin flow throughout the resin bath at $t = 20\,\mathrm{s}$. The regions corresponding to insets (b) and (c) are indicated. Arrows indicate the direction of flow while color indicates the velocity magnitude. **(b)** Resin flow near the growing part at $t = 1.5\,\mathrm{s}$, 2.5 s, 10 s, and 20 s. Light gray under the build platform represents the growing gelled part. **(c)** Resin flow near the edge of the build platform. Times correspond to those for (b). **(d)** Streamlines and $\partial D'/\partial t$ under the growing part. . 59

4.3 The overall shape and uniformity of the curing front is affected by blue intensity, print speed, and part radius. Parameters other than the variable of interest are held constant at $I_b = 100\,\mathrm{mW\,cm^{-2}}$, $I_{uv} = 130\,\mathrm{mW\,cm^{-2}}$, $S = 300\,\mathrm{mm\,h^{-1}}$, and $R_p = 1\,\mathrm{mm}$. The curing front is identified as the $D' = D'_c$ contour. Error bars in dead zone height plots indicate dead zone uniformity and are calculated as the standard deviation of z-coordinate values for points in the dead zone curing front (see Appendix C.3). **(a–b)** Curing front and average dead zone height for blue intensities ranging from $70\,\mathrm{mW\,cm^{-2}}$ to $110\,\mathrm{mW\,cm^{-2}}$. **(c–d)** Curing front and average dead zone height for print speeds ranging from $75\,\mathrm{mm\,h^{-1}}$ to $450\,\mathrm{mm\,h^{-1}}$. **(e–f)** Curing front and average dead zone height for part radii ranging from 0.5 mm to 2 mm. 62

4.4 Exposure optimization under different intensity restrictions for cylinders with radii ranging from $R_p = 2\,\mathrm{mm}$ to $10\,\mathrm{mm}$. The first row of plots shows the incident blue intensity as a function of the r-coordinate normalized to the part radius. The blue intensity is capped at $200\,\mathrm{mW\,cm^{-2}}$. The second row shows the incident UV intensity, which is capped at $275\,\mathrm{mW\,cm^{-2}}$. The third row shows the dose at the part outlet normalized to the critical dose. **(a)** Blue and UV intensities are restricted to constant values across the part radius. The optimized value for each part radius is approximately equal. **(b)** Blue intensity is allowed to vary as a function of r, while UV is constant. **(c)** Both blue and UV intensities are allowed to vary as functions of r. 66

4.5 Experimental verification of optimized exposure parameters for a 10 mm radius cylinder. Plots show the incident blue and UV intensity as functions of the normalized r-coordinate. Insets show the images generated from the intensity functions. Blue intensities were scaled to 100%, 90%, and 80% of their optimized values for print tests. Photos of the top cylinder surface are taken in different focal planes to show the presence (indicated by a dashed circle) or absence of an interior void. Scale bars are 5 mm. **(a)** Unpatterned blue and UV. Printing attempts using 100% and 90% of the optimized blue intensity were unsuccessful as parts consistently cured to the window. Printing at 80% of the optimized blue intensity was successful, though the resulting part had a large void in the center of the cylinder. **(b)** Patterned blue and unpatterned UV. Printing was successful at 100% and 90% of the blue intensity function, while the 80% part was weakly cured. 68

A.1 Projector calibration curve. Measured blue intensity, I_0, is plotted as a function of the grayscale value, p, of the displayed image. The calibration curve is found to be a piece-wise function typical of manufacturer color balancing encoded into projector firmware. 79

A.2 Dose constraint curves *(i) – (iii)* and target dose region. ζ_U and ζ_L are the positions of the top and bottom of the feature, respectively. 88

A.3 Effect of increasing (yellow curves) and decreasing (blue curves) parameters by 50%: **(a)** Base case. $h_\mathrm{s} = 50\,\mu\mathrm{m}$, $\Delta z = 1\,\mathrm{mm}$, $h_\mathrm{a} = 2{,}000\,\mu\mathrm{m}$, $s = 1{,}000\,\mathrm{mm\,h^{-1}}$, and $I_\mathrm{max} = 100\,\mathrm{mW\,cm^{-2}}$. **(b)** Decreasing feature height. **(c)** Increasing feature height. **(d)** Varying absorbance height. **(e)** Varying print speed. From Equation A.9, varying the critical dose has an identical effect. **(f)** Varying the maximum projector intensity. 89

A.4 Maximum dose as a function of $\delta\eta = (z_\mathrm{L} - z_\mathrm{U})h_\mathrm{a}^{-1}$. As the feature height increases, the maximum dose approaches the limit Ω_∞ described in Appendix A.4. Parameters: $h_\mathrm{s} = 50\,\mu\mathrm{m}$, $h_\mathrm{a} = 2{,}000\,\mu\mathrm{m}$, $s = 1{,}000\,\mathrm{mm\,h^{-1}}$, $I_\mathrm{max} = 120\,\mathrm{mW\,cm^{-2}}$, $I_\mathrm{min} = 2\,\mathrm{mW\,cm^{-2}}$. 90

A.5 Maximum dose limits for our presented optimization (Resin 1, $s = 750\,\mathrm{mm\,h^{-1}}$, $I_{\max} \approx 75\,\mathrm{mW\,cm^{-2}}$). **(a)** Exposure height to reach the critical dose starting from zero dose. Printing at a constant speed, larger height ranges must be exposed to reach higher doses. **(b)** The maximum possible dose for a feature of a given height, as determined by the dose constraint equations (Equation A.41 in Appendix A.4). When the correction is applied, the maximum dose within a feature is the minimum of D^* and the chosen $D_{\max}$. 91

A.6 Varying $D_{\max}$ with $D_c = 5D_{gel}$. **(a)** Ratio of height errors (corrected-to-uncorrected) for a range of feature sizes and values of $D_{\max}$. A ratio of zero corresponds to a perfectly corrected feature. Error bars indicate standard error. **(b)** Parts printed at $750\,\mathrm{mm\,h^{-1}}$ using slices corrected with $D_c = 5D_{gel}$ and different values for $D_{\max}$. 92

A.7 Layer-by-layer printing of 3D model in Figure 2.2 (a). $D_c = 576\,\mathrm{mJ\,cm^{-3}}$, $h_s = 50\,\mu\mathrm{m}$, $h_a = 110\,\mu\mathrm{m}$, and $s = 1{,}000\,\mathrm{mm\,h^{-1}}$. **(a)** Vertical stack of uncorrected grayscale projections along the plane indicated in Figure 2.2(a). **(b)** Model prediction from slices in (a) showing areas with cure-through (CT, red). Gray regions of the part are correctly cured (CC). **(c)** Grayscale value and dose for the (x, y) position indicated by the dashed line in Figure 2.2(a). **(d)** Contributions of individual slices to the accumulated dose curve shown in (c) for $n = 21$ to $n = 53$. **(e—h)** Results for corrected slices. 95

B.1 Incident UV intensity versus grayscale value for the Ember 3D printer. The grayscale value for a given pixel is defined as the `[R,G,B]`/255 where `R` = `G` = `B`. $p = 1$ corresponds to white, and $p = 0$ corresponds to black. 99

B.2 Calibration data for blue and UV intensities for the two-color printer. While lines of best fit are included, only points where the intensity was explicitly measured were used in characterization experiments. **(a)** Incident blue intensity, $I_{b,0}$, versus grayscale value, p. The grayscale value for a given pixel is defined as the `[R,G,B]`/255 where `R` = `G` = `B`. $p = 1$ corresponds to white, and $p = 0$ corresponds to black. **(b)** Incident UV intensity, $I_{uv,0}$, versus analog control voltage, V_{uv}. . . . 99

B.3 Comparing initiation point z_0 and steady-state dead zone $z_{f,\infty}$ in photoinhibited model. Note that below the intensity ratio where $z_{f,\infty} = 0$ (also indicated by **x** on the z_0 line), no dead zone exists, and continuous printing is thus not possible. . . . 102

C.1 Calibration data for blue and UV intensities for the two-color printer. **(a)** Incident blue intensity, $I_{b,0}$, versus grayscale value, p. The grayscale value for a given pixel is defined as $[\mathtt{R},\mathtt{G},\mathtt{B}]/255$ where `R` = `G` = `B`. $p = 1$ corresponds to white, and $p = 0$ corresponds to black. **(b)** Incident UV intensity, $I_{uv,0}$, versus analog control voltage, V_{uv}. 105

C.2 Gap between the build platform and window at which forces resulting from the part radius and dead zone height become more significant than forces resulting from the build platform radius and build platform position. $R_{BP} = 25\,\mathrm{mm}$ and $z_f = 100\,\mu\mathrm{m}$. 106

C.3 Curing front position with varying blue and UV intensity at constant intensity ratio. The overall shape and uniformity of the curing front is affected by blue (and UV) intensity, even as the intensity ratio is held constant. Other parameters are held constant at $S = 300\,\mathrm{mm\,h^{-1}}$ and $R_p = 1\,\mathrm{mm}$. The curing front is identified as the $D' = D'_c$ contour. Error bars indicate dead zone uniformity and are calculated as the standard deviation of z-coordinate values for points in the dead zone curing front (see Appendix C.3). **(a)** Curing front and **(b)** average dead zone height for varying blue and UV intensities at a constant ratio of $I_{uv}/I_b = 1.3$. 107

C.4 UV/Blue intensity ratio for variable I_b and I_{uv} optimization. While the shape of the blue and UV intensity functions is similar and the functions for each part radius appear nearly identical, the intensity ratio is not constant with r/R_p, and the intensity ratio function varies for different part radii. 108

C.5 Geometry and optimization results for rectangular symmetry model. **(a)** Diagram of two-color continuous stereolithography. Dashed lines indicate the region of the resin bath included in the COMSOL geometry. **(b)** Geometry for the steady-state, rectangular symmetry model, which is used for intensity optimization. **(c)** Optimized blue and UV intensity for a 10 mm half-width cross-section (W_p). The incident blue intensity is allowed to vary with x and is capped at 200 mW cm^{-2}; the incident UV intensity is constant and is capped at 275 mW cm^{-2}. **(d)** Dose at the part outlet normalized to the critical dose for the optimization in (c). **(e)** Image generated from optimized intensity function in (c). **(f)** Proposed combination of cylindrical and rectangular solutions to ensure curing of edges. 110

LIST OF APPENDICES

Appendix

A. Modelling and Correcting Cure-Through in Continuous Stereolithographic 3D Printing 78

A.1 Projector Calibration Data 78
A.2 Derivation of Dose Equations 78
A.2.1 Derivation of Main Equations 78
A.2.2 Fractional Values of ζ 82
A.2.3 Critical Intensity I_c and Dimensionless Intensity Φ 84
A.2.4 Dependence of $\Omega_T(\zeta)$ on $\Omega_T(\zeta+1)$ 85
A.3 Effect of Finite Contrast Ratio 86
A.4 Equations for Target Dose Region Constraints 87
A.5 Optimizing D_c and Ω_{max} 90
A.6 Model and Correction for Non-Continuous Stereolithography 92
A.6.1 Derivation of Dose Model 93
A.6.2 Slice Correction 94

B. Kinetic Curing Model for Uninhibited and Photoinhibited Stereolithography 98

B.1 Calibration Data for Blue and UV Intensities 98
B.2 Comparing Volume- and Area-Based Dose Models 98
B.3 Initiation Point in Photoinhibited Resin 100

C. Resin Flow and Dead Zone Uniformity in Photoinhibited Continuous Stereolithography 103

C.1 Materials and Methods for Two-Color Continuous Printing 103
C.1.1 Materials 103
C.1.2 Two-Color 3D Printing 104
C.1.3 Calibration Data for Blue and UV Intensities 104
C.2 Separation Force and Build Platform Position 105
C.3 Dead Zone Calculations 106
C.4 Effect of Blue Intensity on Curing Front Profile at Constant Intensity Ratio 107
C.5 Intensity Ratio for Variable Blue/Variable UV Optimization 108
C.6 Rectangular Symmetry Optimization Model 108

LIST OF TABLES

Table

2.1 Resin formulations. 13
3.1 Custom resin formulations. 29
4.1 Resin material properties in the COMSOL models. Resin 1 is used for results in the time-dependent model, and Resin 2 is used with the optimization model. Note that the critical dose and inhibition constant are given in their volumetric forms. . 55
4.2 COMSOL model dimensions. 55
A.1 Total dose by layer (from Equation A.13). 82
C.1 Resin formulation. 104

ABSTRACT

Continuous stereolithography has recently emerged as a leading technology in additive manufacturing (3D printing). Though several methods for continuous printing have been reported, they all share the benefit of reducing forces on the growing part and eliminating adhesion to the resin bath due to the introduction of the *dead zone*, a region where polymerization does not occur. The recently developed dual-wavelength approach, in which photoinitiation and photoinhibition of polymerization are controlled via different wavelengths of light, has achieved unprecedented vertical print speeds via expansion of the dead zone. We address several limitations in dual-wavelength continuous printing (and some within continuous stereolithography more broadly) via theoretical and computational modeling and the use of spatially varying exposure patterns. First, we address the problem of *cure-through*, undesired curing along the axis of exposure, which is more significant in continuous stereolithography than in traditional layer-by-layer stereolithography. Recognizing that the use of highly absorbing resins to improve layer resolution inherently limits achievable print speeds, we developed a method to improve part fidelity in low- to moderate-absorbance resins through modification of the images projected during printing. We derive a mathematical model to describe dose accumulation during continuous printing, describe the resulting grayscale-based correction method, and experimentally verify correction performance. Using optimized parameters with a high absorbance height resin ($h_a = 2{,}000\,\mu\text{m}$), feature height errors are reduced by over 85% in a test model while maintaining a high print speed ($750\,\text{mm}\,\text{h}^{-1}$). Recognizing the limita-

tions of this model, we developed a kinetics-based curing model for dual-wavelength photoinitiation/photoinhibition under variable intensities. The model is verified via experimental characterization of two custom resins using cured height and dead zone height experiments. For the two custom resins characterized, the model achieves R^2 values of 0.985 and 0.958 for fitting uninhibited cure height data and values of 0.902 and 0.980 for fitting photoinhibited dead zone height data. The model is also applicable to resins in standard layer-by-layer stereolithography, and for commercial resin cure height data, our model performs similarly to the standard Jacobs model, with all R^2 values above 0.98. Finally, we introduce the complexities of resin flow during continuous printing. The kinetic curing model is used in a computational fluid dynamics model to analyze dead zone uniformity, which we find is greatly affected by exposure intensity ratio, while print speed and part radius have minor effects. We find that relatively small variations in the intensity ratio (25%) can have large effects, going from good printing conditions to print failure (curing to the window) or to significant nonuniformity (maximum dead zone height over three times the minimum). We optimize exposure conditions to maximize dead zone uniformity, finding that the ability to pattern light sources is critical in generating uniform dead zones: for a 10 mm radius cylinder, over 90% of the dead zone is near the optimized value when using patterned intensity functions, compared with only 18% when using constant intensity values. In printing experiments, we find that an optimized intensity function can, without modification, successfully produce difficult-to-print parts. Taken as a whole, the work advances our understanding of the dual-wavelength approach in continuous stereolithography, improves printing performance, and motivates future research into the wide range of physical phenomena affecting the system.

CHAPTER I

Introduction

1.1 Stereolithography in Additive Manufacturing

Stereolithography, or vat photopolymerization, is a branch of additive manufacturing in which parts are fabricated from photopolymer that is selectively cured by exposure to light [1]. Stereolithography is generally recognized as the first commercial 3D printing technology and was first developed in 1983 by Charles Hull [2, 3]. Hull went on to found 3D Systems, Inc., which introduced the SLA-1 in 1987. In this and other early stereolithographic systems, part are fabricated layer-by-layer from the bottom up using a scanning laser and a build platform that descends into a vat of photopolymer. In each cycle of the printing process, the build platform is positioned with a thin layer of resin above the growing part, and the laser traces out a cross-section onto the resin surface, solidifying the material and adding a layer to the part. The invention of stereolithography and other early additive manufacturing methods (e.g., selective laser sintering [4] and fused deposition modeling [5]) enabled rapid prototyping, the ability to quickly iterate through designs, by lowering the cost of producing unique and low-quantity parts.

In the decades since the SLA-1 was released, several key innovations have improved the part quality and print speed of stereolithography. Improving on the

pointwise curing mechanism of laser scanning approaches, dynamic mask projection stereolithography (or simply *projection stereolithography*) was developed using LCD [6] or DLP [7] projectors to solidify entire cross-sections concurrently. The transition from free surface approaches (in which the top *free surface* of resin is exposed) to constrained surface approaches (in which resin at the bottom of the vat is exposed through a window) improved print speeds and resolutions and reduced the volume of resin required for printing; this transition was enabled by the development of new surface coatings and separation techniques [8, 9, 10, 11]. Today, a wide range of constrained-surface DLP stereolithographic 3D printers are commercially available.

A particularly important—and relatively recent—innovation is the development of continuous printing processes. In typical layer-by-layer stereolithography, the part adheres to the window during the curing of each layer. Continuous stereolithography is premised on the introduction of a *dead zone* near the window in which polymerization does not occur. The first reported continuous stereolithography process, continuous liquid interface production (CLIP), achieved smooth, layerless parts with isotropic properties at production rates an order of magnitude larger than previous stereolithographic methods [12, 13, 14]. Since the development of CLIP, several other continuous stereolithography approaches have been reported which continue to increase print speeds and expand the range of printable parts [15, 16, 17].

1.2 Dual-Wavelength Continuous Stereolithography

While aspects of this dissertation apply broadly to stereolithography or continuous stereolithography, much of the focus of and motivation for this work is a particular approach—dual-wavelength continuous stereolithography—which was developed by Dr. Martin de Beer in the Burns research group [15, 18]. Figure 1.1(a) shows the

printer configuration for dual-wavelength continuous stereolithography. A resin bath is filled with liquid photopolymer resin and a moving build platform is positioned at the bottom of the bath. During printing, the build platform continually ascends and images are projected through a window at the bottom of the resin bath to cure cross-sections of the desired part.

Like other methods of continuous stereolithography, the dual-wavelength method introduces a region at the bottom of the resin bath where polymerization does not occur (i.e., a *dead zone*) to prevent the part from adhering to the window. Other continuous stereolithography methods have generated the dead zone via oxygen inhibition [19, 12, 17] or by using a higher-density, nonreactive fluid layer [16]. The dual-wavelength method is based on the use of orthogonal photochemistries to confine polymerization to a desired region [20, 21]. Printing resins are formulated with a blue-active photoinitator—camphorquinone, with co-initator 4-(dimethylamino)benzoate (EDAB)—and a UV-active photoinhibitor—2,2'-Bis(2-chlorophenyl)-4,4',5,5'-tetraphenyl-1,2'-biimidazole (*o*-Cl-HABI)—as well as nonreactive blue and UV light absorbers. Taking advantage of non-overlapping regions of the species' absorbance spectra (Figure 1.1(b)), initiation is controlled using blue light (455 nm) and inhibition is controlled using UV light (365 nm).

Using this system, de Beer and coworkers produced a variety of parts, demonstrated single-exposure surface patterning, and showed the technique's applicability for different oligomers [15]. The approach achieved dead zones orders of magnitude larger than those obtained in oxygen-inhibited printers, and as a result, dual-wavelength continuous stereolithography boasted the highest reported linear print speeds of any continuous printing method at the time of publication.

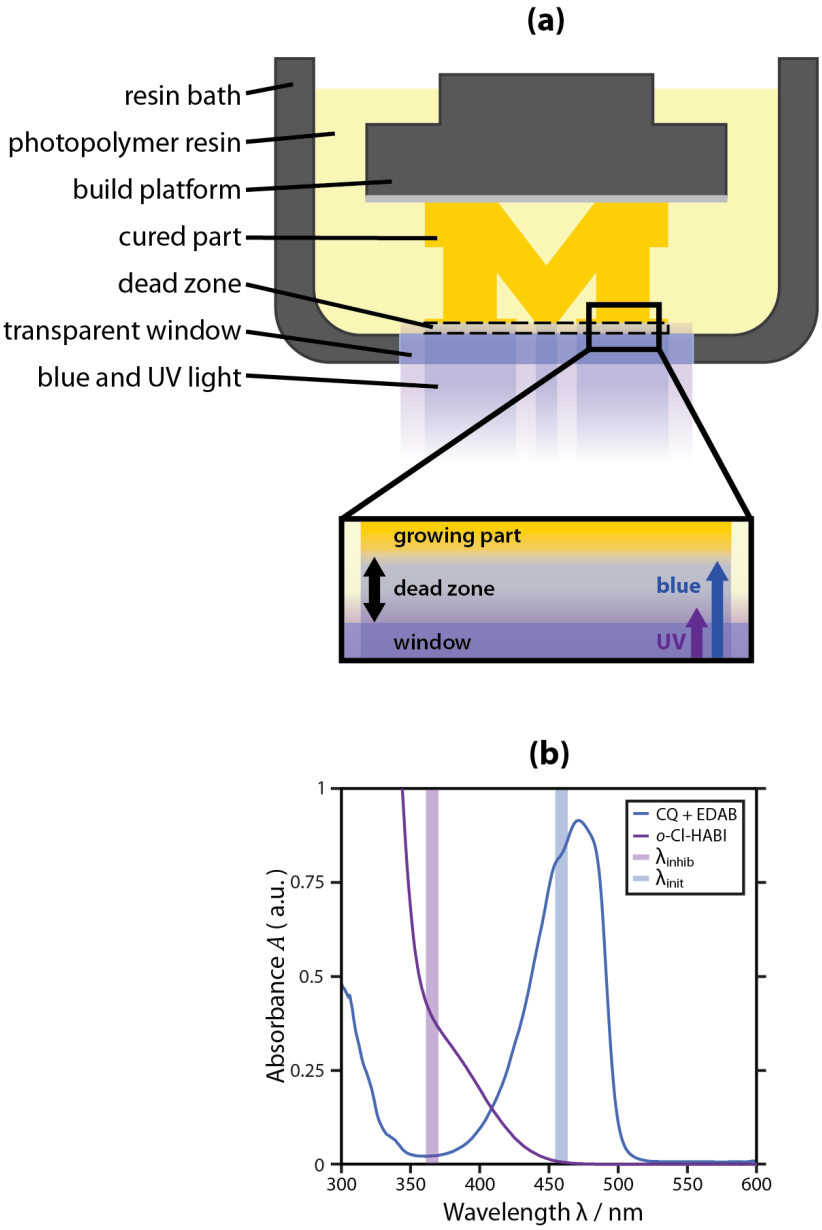

Figure 1.1. **(a)** In dual-wavelength continuous stereolithography, a dead zone is generated near the window using orthogonal initiation and inhibition photochemistries. Blue light drives polymerization, while UV light inhibits it. **(b)** Absorbance spectra of 0.4 wt.% CQ and EDAB (initiator and co-initiator) and 0.06 wt.% *o*-Cl-HABI (inhibitor) in tetrahydrofuran (THF). The emission wavelength of the initiating and inhibiting light sources used in experiments are shown in with shaded blue and purple boxes.

1.3 Modelling Reaction and Transport Effects in Stereolithographic 3D Printing

This work is largely motivated by a desire to understand and improve the dual-wavelength approach. It is characterized by numerous competing reactions, flow-dependent resin exposure histories, large deforming forces, and transience in species concentrations, temperature profiles, and material properties. This dissertation attempts to make a contribution to our understanding of this complex physical system and to lay the groundwork for future investigations.

In Chapter II, we present a method for modelling and correcting cure-through in continuous stereolithographic 3D printing. Continuous stereolithography offers significant speed improvements over traditional layer-by-layer approaches but is more susceptible to *cure-through*, undesired curing along the axis of exposure. Typically, cure-through is mitigated at the cost of print speed by reducing penetration depth in the photopolymer resin via the addition of nonreactive light absorbers. We present a mathematical approach to model the dose profile in a part produced using continuous stereolithography. From this model, a correction method is developed to modify the projected images and produce a chosen dose profile, thereby reducing cure-through while maintaining print speed. The method is verified experimentally on a continuous stereolithographic 3D printer, and the practicality of various dose profiles is investigated. Overall, we are able to reduce cure-through by over 85% in a test model while maintaining a high print speed of $750\,\mathrm{mm\,h^{-1}}$.

Drawing on questions raised during our work on cure-through correction, Chapter III focuses on dose-based curing models for standard, uninhibited projection stereolithography and dual-wavelength continuous stereolithography. We develop models for each that do not require the reciprocity assumption—that the rate of polymeriza-

tion depends on the product of intensity and exposure time (i.e., the optical dose) but not their independent values—to be valid. These models maintain the straightforward characterization experiments typically used in stereolithography (cured height experiments) while allowing for an unknown exponential intensity dependence. We experimentally verify that the models are capable of describing curing behavior across a range of intensities using commercial resins with a commercial 3D printer for the uninhibited model and custom resins with our custom dual-wavelength continuous 3D printer for the photoinhibited model. The photoinhibited model has also been successfully applied to control dead zone thickness in other work [18].

Whereas Chapter III deals with resin characterization and stationary exposures in the dual-wavelength system, in Chapter IV we begin to address the complexities introduced by resin flow during continuous printing. We develop and analyze computational fluid dynamics models to simulate dual-wavelength stereolithography and investigate how resin flow affects the development of the dead zone and the printability and fidelity of parts. While stationary experiments and the kinetic model suggest straightforward control of the dead zone thickness, our simulations suggest that dead zone thickness may not be easily controllable for a fixed resin, part, and print speed. In an optimization process, we are able to predict successful printing parameters by seeking intensity profiles that maximize dead zone uniformity in the model. We find that the ability to pattern both blue and UV exposures (rather than blue only, as in the current dual-wavelength printer) has the potential to significantly improve dead zone uniformity. Our results lay the groundwork for future computational studies of flow and deforming forces in the dual-wavelength system.

Chapter V presents conclusions and a summary of the dissertation as well as future avenues for investigation.

CHAPTER II

Modelling and Correcting Cure-Through in Continuous Stereolithographic 3D Printing

This work was completed in close collaboration with Dr. Martin de Beer. My contributions were in conceptualization of the project, derivation and programming of the model, investigation of theoretical results, writing, and data visualization. Dr. de Beer also contributed to conceptualization, writing, and visualization, as well as providing experimental validation of the model, analysis of experimental results, and many hours of fruitful discussion. This work was published in *Advanced Materials Technologies* [22] and also appears in Dr. de Beer's dissertation [18].

2.1 Introduction

Additive manufacturing (AM), commonly called 3D printing, refers to a number of technologies through which objects are created by progressive addition of material [23, 24]. With its simplicity and nearly unlimited design choice, AM is attractive for producing custom, limited-quantity, and prototype parts. AM has found numerous applications in fields including biomedical engineering [25, 26, 27, 28, 29], bio-inspired materials [30, 31, 32], functional materials [33, 34, 28, 35, 36, 37, 38], and the DIY "maker" industry [39]. In projection stereolithography, a widely-used AM method, photopolymerizable resin is exposed to patterned light to cure cross-

sections of a desired 3D part. Typically, stereolithography produces parts in discrete layers. Exposed areas are cured through the full layer height, whereupon the part is repositioned and recoated with resin before the next layer is exposed. Recently, continuous stereolithographic technologies have been developed which increase print speeds by eliminating the time-consuming repositioning and recoating steps [12, 15]. Print speed in continuous stereolithography is dependent on the resin absorbance height, with low-absorbance resins allowing extremely high print speeds of up to $2{,}000\,\mathrm{mm\,h^{-1}}$ at the cost of part fidelity.

In stereolithography, the penetration depth of light in the resin limits accuracy along the vertical axis: unaccounted-for light propagation can cause undesired curing, known as cure-through, overcure [40, 41], the back-side effect [42], or print-through error [12, 43]. This phenomenon can also contribute to cross-linking heterogeneity, introducing internal stresses which can deform the part and further reduce fidelity [44]. The prevalent strategy to mitigate cure-through is to add nonreactive light absorbers to the resin formulation [40, 45, 46, 47, 44]. Highly-absorbing resins have been widely adopted despite the slower print speeds needed to ensure fully cured layers. Alternatively, cure-through can be mitigated without sacrificing speed by modifying the projected images (*slices*) based on modelling of the curing process. Optimization-based methods to eliminate cure-through by adjusting model dimensions have been developed for external surfaces and internal voids in traditional stereolithography [41, 43, 48]. Manual adjustments to account for cure-through have also been reported [49].

Nevertheless, slice correction has not been described for continuous stereolithography, where cure-through is a more significant and complex problem. Furthermore, existing models of continuous stereolithography are not tailored to this application

[19, 50, 51].

Here, we present a curing model and a slice correction algorithm for continuous stereolithography. Previous non-continuous approaches used iterative and heuristic processes to find optimal corrections and were restricted to black and white pixels; our correction method uses grayscale, which has previously only been used to improve lateral resolution [52], along with an exact mathematical solution to precisely set the dose profile within a part. We also present experimental validation of our model and correction approach using a recently-developed two-color continuous stereolithographic 3D printer [15]. These methods are adapted for traditional layer-by-layer stereolithography in Appendix A.6.

Figure 2.1(a) shows how our correction process fits into the existing 3D printing workflow. To demonstrate the applicability of the slice correction method to typical parts, we printed corrected and uncorrected versions of two open-source models (Figure 2.1(b–c)) [53, 54]. In both cases, parts printed with uncorrected slices significantly deviate from the design as a result of cure-through. Applying slice correction to these parts significantly reduces the occurrence of cure-through, with corrected parts showing increased accuracy in the z-direction.

2.2 Materials and Methods

2.2.1 Modeling and Correction

Computational models and slice correction algorithms were implemented in MATLAB R2018b (MathWorks) and run on a desktop computer (Intel Xeon E5-1660 v4 @ 3.2 GHz, 32 GB RAM). Simulations and corrections completed within several minutes for all models.

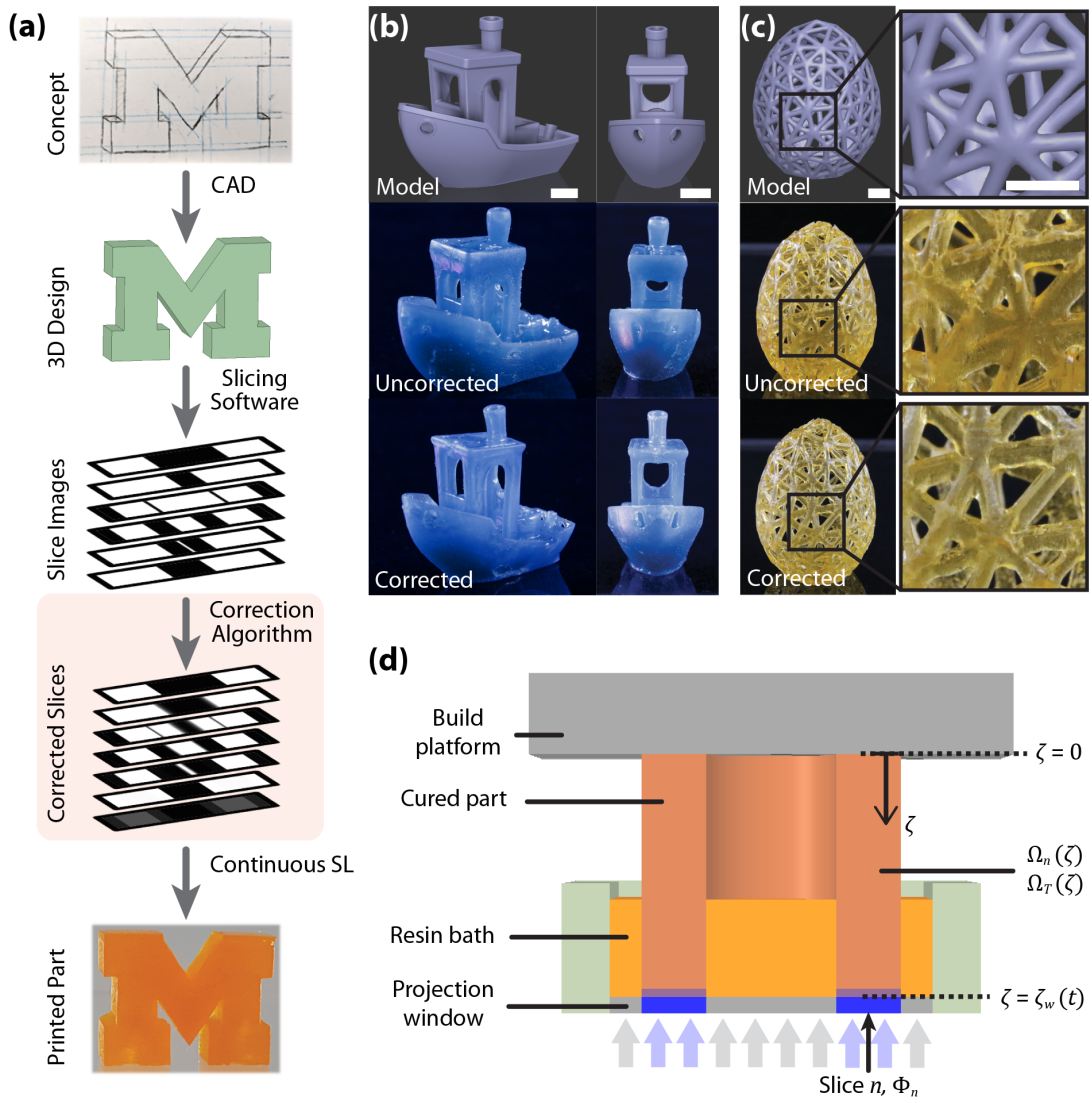

Figure 2.1. **(a)** Cure-through correction is incorporated into the 3D printing workflow by computationally processing slice images. **(b–c)** Correction applied to real models, reducing the extent of cure-through while maintaining print speed. Scale bars are 5 mm. **(b)** #3DBenchy [53] printed at 800 mm h^{-1} (h_a = 1,500 µm, D_c = 230 mJ cm^{-3}), and **(c)** hollow egg [54] printed at 800 mm h^{-1} (h_a = 2,000 µm, D_c = 173 mJ cm^{-3}). **(d)** Vertical cross-section of printer setup showing nondimensionalized variables of interest: ζ, Ω_n, and Φ_n are the dimensionless z-position, dose, and light intensity, respectively.

Dose Modeling Slice images are initially read into the program and stored as a three-dimensional array. The dimensions of this array correspond to the number of slices and their dimensions in pixels. A typical slice image is 1,280 by 800 pixels and the number of slices is equal to the height of the designed part divided by the slicing height, h_s. In cases where the model does not utilize the full slice resolution (e.g., a 200-pixel-wide model in the center of a 1,280-pixel-wide image), the excess pixels outside the model volume are trimmed from the matrix to improve computational performance. The values in this matrix are grayscale pixel values (p) ranging from zero to one and correspond to the light intensities that will be projected at each pixel during each slice; zero and one represent the minimum and maximum blue-light intensities, respectively. The relationship between pixel value and light intensity is not linear, and pixel values are converted into intensities using a calibration curve (Appendix A.1) generated with a radiometer (International Light IL1400A) with a GaAsP detector (model SEL005), a 10× attenuation neutral density filter (model QNDS1), and a quartz diffuser (model W).

Dose calculation begins at the bottom of the part, where the final slice is projected, and proceeds upward. The top cross-section of the part is exposed to every slice and each successive layer is exposed to fewer and fewer slices. By starting at the bottom of the part, we consider the cross-sections of the part exposed only to the final slice, then those exposed to the final two slices, then those exposed to the final three slices, and so on. As shown in Equation 2.6 and Table A.1, the total dose at ζ is the sum of the dose contribution from slice $n = \zeta$ and the total dose at $\zeta + 1$ multiplied by a factor of $10^{-\eta}$.

Slice Correction The unedited images from the slicing software are taken to represent the "true" model and are converted into matrix form as above. Each feature within the part is identified. As with dose modeling, slice correction begins at the bottom of the part and works upward. Pixel values at the backside of the feature are set to reach D_c as quickly as possible (i.e., using the maximum intensity), and pixel values inside the feature are set to match a desired internal dose profile using Equation 2.6. All pixel values are assumed to be zero (minimum intensity) unless specifically set otherwise. Finally, the matrix of corrected pixel values is converted back to a series of image files to be sent to the 3D printer.

2.2.2 3D Printing

Part Design Test parts were designed in DesignSpark Mechanical 2.0 (SpaceClaim Corp.) and exported as STL files. Models were sliced using Autodesk Netfabb Standard 2018 (Autodesk) with default settings for the Ember 3D Printer (Autodesk) and 10 µm slice height. Slices from Netfabb are used with the MATLAB code to model final printed parts and produce corrected slices.

3D Printer We printed test parts on a previously-described dual-color continuous stereolithographic 3D printer [15]. The DLP LED projector (Optoma ML750) was modified by removing power to the green and red LEDs and powering the blue LED by an external 0–5 A LED driver circuit controlled by a custom LabVIEW virtual instrument.

Resin Formulations Polymer resin was formulated as a mixture of oligomer, reactive diluent, photoinitiators, photoinhibitor, and light absorbers. For this work, the oligomer Sartomer CN991 (Sartomer) was used with 1,6-hexanediol diacrylate

Table 2.1. Resin formulations.

Component	Function	Concentration (wt.%)		
		Resin 1	Resin 2	Resin 3
o-Cl-HABI	Photoinhibitor	2.8	2.8	2.8
Camphorquinone	Photoinitiator	1.9	1.9	1.9
EDAB	Co-initiator	0.95	0.95	0.95
Tinuvin 328	UV absorber	0.47	0.47	0.47
Epolight 5675	Blue light absorber	0.001	0.003	–
CN991	Oligomer	56.3	56.3	56.3
HDDA	Reactive diluent	37.6	37.6	37.6
Blue pigment	Light absorber	–	–	0.002

(HDDA, TCI America) as a reactive diluent. (±)-Camphorquinone (CQ, Esstech) was used as a blue-light photoinitiator and ethyl-4-dimethylaminobenzoate (EDAB, Esstech) was used as a co-initiator. 2,2'-Bis(2-chlorophenyl)-4,4',5,5'-tetraphenyl-1,2'-biimidazole (*o*-Cl-HABI, TCI America) was used as a UV-activated photoinhibitor. Epolight 5675 (Epolin) was used as the blue light absorber and Tinuvin 328 (BASF) was used as the UV absorber. Commercial blue epoxy pigment (Makerjuice Labs) was also used as a light absorber. The compositions of resins used are given in Table 2.1.

Resin Characterization The two resin properties required for input into the correction algorithm are the absorbance height h_a and the gelation dose D_gel. These properties are fitted using the least-squares method with a cured height vs. dose working curve similar to that developed by Jacobs [55]:

$$z_\mathrm{ct} = h_\mathrm{a} \log\left(\frac{I_0 t}{D_\mathrm{gel}} \frac{\ln 10}{h_\mathrm{a}}\right) \tag{2.1}$$

Liquid photopolymer is cured into plugs by exposing to curing light of intensity I_0 for varying lengths of time t. The height of the cured plug is measured using a digital micrometer with an accuracy of 10 µm. Light intensity is determined using the calibration curve in Appendix A.1.

2.3 Results and Discussion

2.3.1 Dose-Based Correction for Continuous 3D-Printing

A schematic of the printer and coordinate system is shown in Figure 2.1(d). The coordinate system is defined with respect to the build platform, with $z = 0$ at the platform and increasing towards the projection window (i.e., downward). The coordinates x and y are omitted from our notation for simplicity; however, the presented equations must be applied at fixed (x, y) positions since the projected slices are patterned. The build platform begins in contact with the window and continuously moves upward while printing. The curing model, then, includes simultaneous continuous and discrete processes: as the build platform continuously ascends, exposure patterns change at discrete intervals with each slice projected in sequence. Below, we present a brief description of the model; a complete derivation is available in Appendix A.2.

To account for the discrete projection of slices, the total accumulated dose at a point is a sum of contributions from each slice projected. $D_{\mathrm{T}}(z)$ is the total volumetric dose delivered to position z in the final part, and the contribution of slice n to the total dose is $D_{\mathrm{n}}(z)$. Thus, $D_{\mathrm{T}}(z) = \sum_{n=0}^{N} D_{\mathrm{n}}(z)$ where slices are numbered from zero to N in order of exposure. From Beer's Law, the time-derivative of volumetric dose as a slice is projected is

$$\frac{\partial}{\partial t} D_{\mathrm{n}}(z,t) = \frac{\ln 10}{h_{\mathrm{a}}} I_{\mathrm{n,w}} 10^{-[z_{\mathrm{w}}(t)-z]h_{\mathrm{a}}^{-1}} \tag{2.2}$$

where $I_{\mathrm{n,w}}$ is the light intensity at the window, $z_{\mathrm{w}}(t)$ is the time-varying position of the window, and h_{a} is the resin absorbance height (i.e., the propagation distance over which the intensity falls to 10% of its initial value).

With the build platform continuously ascending, $D_{\mathrm{n}}(z)$ is determined for each

slice by integrating over the time period when the slice is projected. Since the coordinate system is fixed with respect to the build platform, time-dependence can be incorporated via the continuously increasing value of $z_{\mathrm{w}}(t)$ and the print speed $s = \mathrm{d}z_{\mathrm{w}}/\mathrm{d}t$. Integrating Equation 2.2 over the exposure of slice n yields Equation 2.3:

$$D_{\mathrm{n}}(z) = \frac{I_{\mathrm{n,w}}}{s}\left\{10^{-(nh_{\mathrm{s}}-z)h_{\mathrm{a}}^{-1}} - 10^{-[(n+1)h_{\mathrm{s}}-z]h_{\mathrm{a}}^{-1}}\right\} \tag{2.3}$$

where h_{s} is the slicing height. Equation 2.3 applies if the cross-section at height z is exposed to slice n (i.e., when $z \leq nh_{\mathrm{s}}$); otherwise, $D_{\mathrm{n}}(z) = 0$. The total accumulated dose at a point, $D_{\mathrm{T}}(z)$, is obtained by summing Equation 2.3 over all slices to which z is exposed:

$$D_{\mathrm{T}}(z) = \sum_{n=zh_{\mathrm{s}}^{-1}}^{N} \frac{I_{\mathrm{n,w}}}{s}\left\{10^{-(nh_{\mathrm{s}}-z)h_{\mathrm{a}}^{-1}} - 10^{-[(n+1)h_{\mathrm{s}}-z]h_{\mathrm{a}}^{-1}}\right\} \tag{2.4}$$

or, in dimensionless form,

$$\Omega_{\mathrm{T}}(\zeta) = \sum_{n=\zeta}^{N} \Phi_{\mathrm{n}}\left\{10^{-(n-\zeta)\ eta} - 10^{-[(n+1)-\zeta)]\eta}\right\} \tag{2.5}$$

with dimensionless variables $\Omega \equiv DD_{\mathrm{c}}^{-1}$ (where D_{c} is the experimentally determined critical dose), $\zeta \equiv zh_{\mathrm{s}}^{-1}$, $\Phi \equiv I_{\mathrm{w}}I_{\mathrm{c}}^{-1}$ (where I_{c} is the minimum intensity needed to reach D_{c}), and $\eta \equiv h_{\mathrm{s}}h_{\mathrm{a}}^{-1}$. Equation 2.5 allows calculation of Ω_{T} for any integer value of ζ in the final printed part.

Equation 2.5 can be simplified to quickly perform dose calculations and slice corrections by writing $\Omega_{\mathrm{T}}(\zeta)$ as a function of $\Omega_{\mathrm{T}}(\zeta+1)$:

$$\Omega_{\mathrm{T}}(\zeta) = \Omega_{\zeta}\left(1 - 10^{-\eta}\right) + \Omega_{\mathrm{T}}(\zeta+1)\,10^{-\eta} \tag{2.6}$$

Starting at the bottom of the part (i.e., $\zeta = N$) and moving upwards, the total dose may be calculated for each integer value of ζ by considering only the current layer

and the preceding layer. Expressions for Ω_T at several values of ζ, along with a full derivation, are available in Appendix A.2.

The above mathematical model allows calculation of the accumulated optical dose at any position in the part and any time in the printing process. Since D_c defines the threshold for curing, an accurate dose profile has $\Omega_T \geq 1$ within designed features and $\Omega_T < 1$ outside features. At points where these conditions are not met, the printed part will exhibit undercure or cure-through artifacts.

Figure 2.2 shows modeled results for a ladder-like part printed using the default slicing approach, in which the maximum intensity is projected whenever an intended feature is adjacent to the window. There is significant cure-through into the gaps, and the bottom of the second feature is undercured. Rather than producing the desired two features, the conventional approach yields a single, large feature.

The total dose profile shown in Figure 2.2(d) is the result of contributions from all slices projected, as expressed in Equation 2.5. A closer look at the bottom feature highlights the causes of cure-through and undercure: Figure 2.2(e) shows the contribution of each slice to the total dose for this feature and, thus, the evolution of the dose curve during the continuous printing process. The uncorrected slices use only the maximum and minimum projector intensities ($p = 1$ and $p = 0$, respectively). While the maximum intensity is projected ($n = 31$ to 40), the accumulated dose rapidly increases for all $\zeta \leq n$. The nonzero minimum intensity results from light scatter in the projection system and is related to the projector contrast ratio (see Appendix A.3). Dose contributions while the minimum intensity is projected ($n = 21$ to 30 and $n = 41$ to 50) are relatively small. In the gap from $\zeta = 21$ to 30, the small contributions from minimum-intensity slices are overwhelmed by the contributions from maximum-intensity slices, resulting in cure-through. The feature

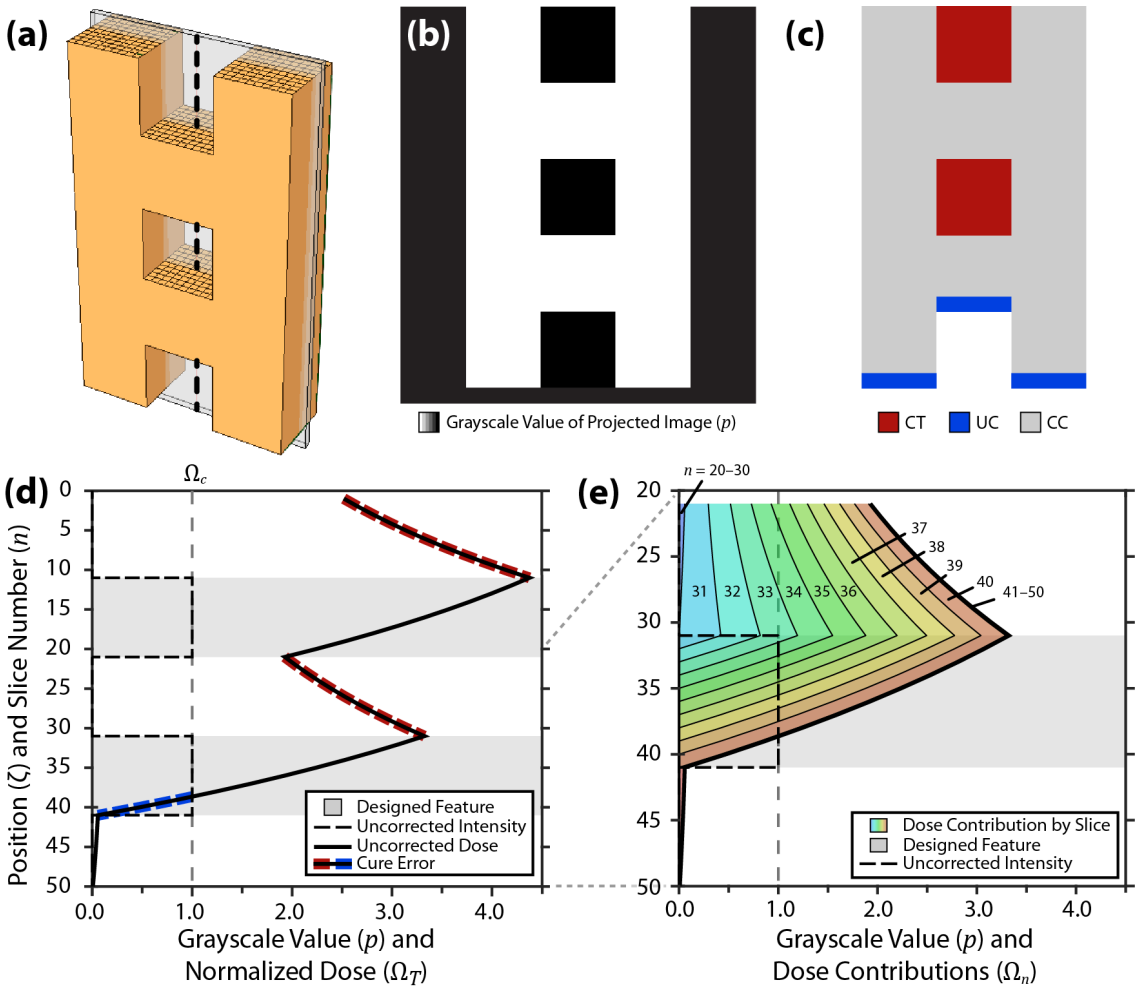

Figure 2.2. Model results for uncorrected slices. **(a)** Test model. **(b)** Vertical stack of uncorrected grayscale projections along the plane indicated in (a). Note that only black and white ($p = 0$ and $p = 1$) are used by default. **(c)** Model prediction from slices in (b) showing areas with cure-through (*CT*, red) and undercuring (*UC*, blue). Gray regions of the part are correctly cured (*CC*, gray). **(d)** Grayscale value as a function of n and total accumulated dose as a function of ζ for the (x, y) position indicated by the dashed line in (a). $D_c = 576\,\mathrm{mJ\,cm^{-3}}$, $h_s = 50\,\mu\mathrm{m}$, $h_a = 2{,}000\,\mu\mathrm{m}$, and $s = 1{,}000\,\mathrm{mm\,h^{-1}}$. $\zeta = 0$ corresponds to the top of the part (i.e., the surface attached to the build platform). The grayscale value p relates to the intensity of the projected pixel when $\zeta_w = n$ (calibration curve in Figure A.1). Shaded areas indicate designed features. The dose curve indicates the normalized total dose Ω_T at position ζ on completion of the print, with cure errors indicated in red (cure-through) or blue (undercure). **(e)** Evolution of the total dose curve shown in (d) for $n = 21$ to $= 50$. The total dose is the sum of contributions from individual slices, each labeled and represented by a color.

is correctly cured from $\zeta = 31$ to approximately 38 then undercured through its designed bottom edge at $\zeta = 41$, highlighting that a point must be exposed over several slices to fully cure—even when projecting the maximum intensity. Finally, the gap below the feature correctly remains uncured. From this simple example, it is apparent that cure-through and undercure are inevitable when using unmodified slices with low-absorbance resins. This analysis also suggests that carefully designed slice images could achieve the desired geometry.

The primary requirement for correcting cure-through and undercure is that the full height of each feature is cured without gelling non-features. However, as has been recently discussed with respect to tomographic printing, it is not possible to deliver exactly the critical dose within features and exactly zero dose outside features: to do so requires the ability to effectively "subtract" dose using negative intensities [56]. Clearly, not all dose profiles are achievable. Physically attainable dose profiles must be continuous and are limited by resin properties and printing parameters. These considerations define a set of three constraints, illustrated in Figure 2.3 and derived in Appendix A.4:

(i) For all points within a feature, $\Omega_T \geq 1$; for all other points, $\Omega_T < 1$. Since Ω_T varies continuously with ζ, features will only be reproduced accurately if $\Omega_T = 1$ along edges.

(ii) The maximum projector intensity, print speed, and resin absorbance height determine the maximum rate at which the dose can increase. With $\Omega_T = 1$ fixed at the bottom edge of the feature, these parameters define a maximum dose within the feature and a minimum dose below the feature.

(iii) From Equation 2.5, the minimum dose at point ζ is limited by the minimum

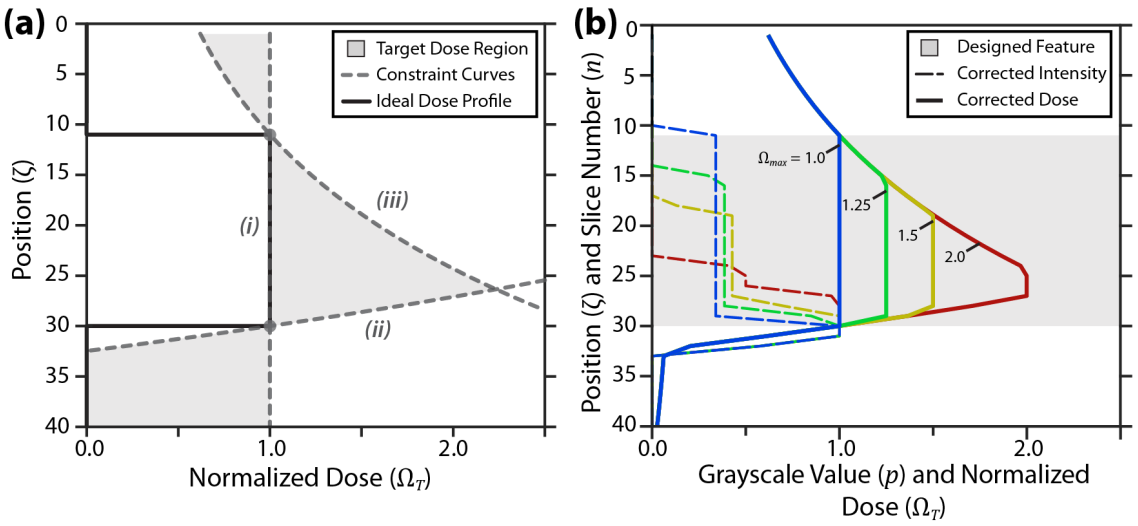

Figure 2.3. Target dose region and dose profiles. **(a)** Three constraints which define the target dose region (shaded): *(i)* curing of features while non-features remain uncured, *(ii)* exposure at the maximum dose at the bottom of the feature, and *(iii)* exposure at the minimum dose at the top of the feature. **(b)** Valid dose profiles defined by maximum dose $\Omega_{\max}$ with corresponding intensity profiles. Here, shading indicates the designed feature height. For a given set of parameters, the intensity profile can be tailored to achieve either a uniform dose or a high peak dose within features while still eliminating cure errors.

projector intensity, the print speed, the resin absorbance height, and the dose at point $\zeta + 1$. With the dose at the top edge set at the critical dose, these parameters define a maximum dose within the feature and a minimum dose above the feature.

If any of these constraints are violated, the feature's edges will shift from their designed positions.

The three constraints define *target dose regions*, indicated by shading in Figure 2.3(a). These regions are demonstrated here for a particular feature, but they can be generated for any feature height by shifting curves *(ii)* and *(iii)* along the ζ-axis such that the edges of the feature remain at the critical dose. Since the doses at adjacent points are interrelated, it is not possible to generate arbitrary dose profiles within the regions. However, there are an infinite number of achievable profiles which fall entirely within the target dose regions and thus produce an accurate part.

To implement slice correction, a valid dose profile is determined for the feature, and Equation 2.6 is solved for each pixel of each slice (starting from the bottom of the part) to determine the intensity required to reach the desired dose. One approach to designing dose profiles is in terms of a *maximum dose*, $\Omega_{\max}$. Constraint curves *ii* and *iii* are traced up to the prescribed $\Omega_{\max}$, which is maintained within the center of the feature. Figure 2.3(b) shows a collection of these dose profiles and the intensities needed to achieve them.

For the important case of $\Omega_{\max} = 1$, the critical dose is uniformly delivered throughout the feature. We applied this correction to the model in Figure 2.2(a), with results illustrated in Figure 2.4. A comparison of Figure 2.4(a) and 2.2(b) shows how the correction process modifies slices. For the rung-like inner features, the intensity is reduced through most of the feature and a high-intensity burst is delivered at the bottom. Since there is no possibility of cure-through for the outer features, they are exposed at the maximum intensity. Figure 2.4(b) indicates that the correction has completely eliminated cure-through and undercure in our modeled result. Figure 2.4(c–d) show how the corrected slices achieve the desired dose profile. The high intensity burst at the bottom of the feature ensures all layers reach the critical dose. From the bottom-up perspective of the correction calculations, a constant intensity maintains the dose from one layer to the next after the critical dose is achieved at the bottom of the feature. From Equation 2.6, the intensity required to maintain a dose between two layers is $\Phi_{\mathrm{n}} = \Omega_{\mathrm{T}}$. Thus, to maintain the critical dose $\Phi_{\mathrm{n}} = \Omega_{\mathrm{c}} = 1$.

To achieve higher maximum doses, features must be exposed at higher intensities for shorter periods, as shown in Figure 2.3(b); a smaller fraction of the feature is exposed so that constraint *(iii)* is not violated. Though the edges of the feature are at the critical dose for each intensity profile, the interior dose varies considerably. As

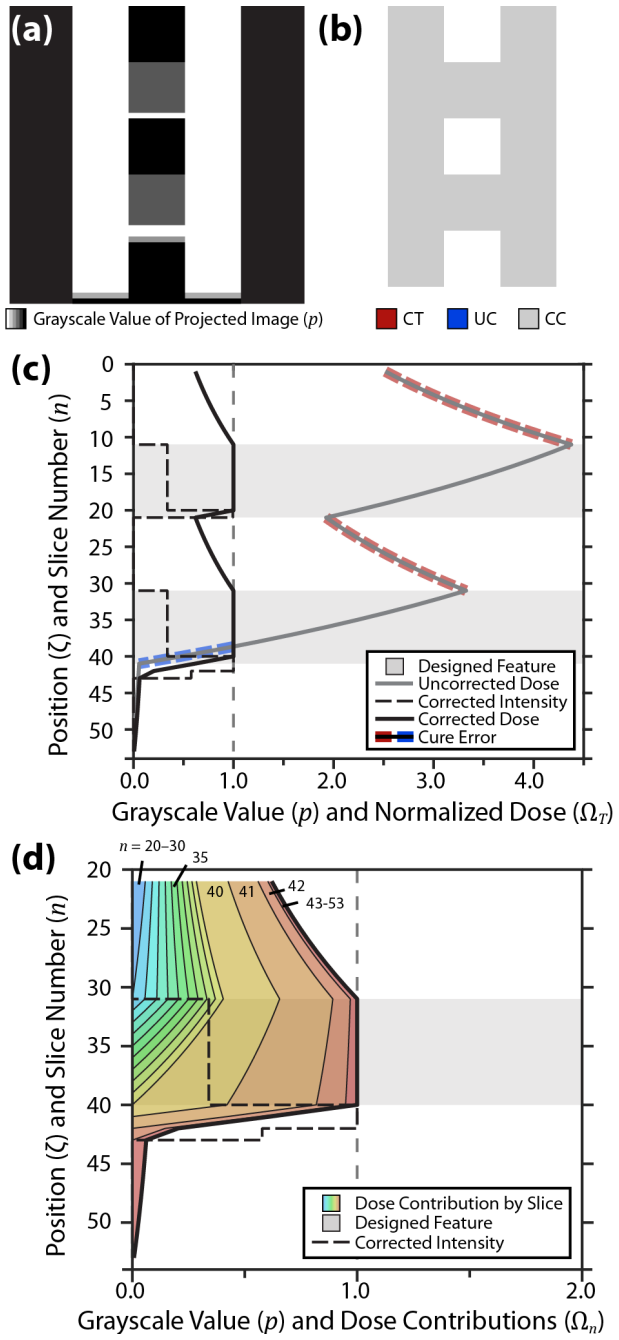

Figure 2.4. Correction for model in Figure 2.2(a) with $\Omega_{\max} = 1$. **(a)** Vertical stack of corrected grayscale projections along the plane indicated in Figure 2.2(a). **(b)** Model prediction from slices in (a) showing no cure-through (CT, red) or undercure (UC, blue). The full part is correctly cured (CC, gray). **(c)** Corrected grayscale value and dose for the (x, y) position indicated by the dashed line in Figure 2.2(a). Note that the correction process required additional slices beyond the original 50 to ensure the bottom of the part was fully cured. $D_c = 576\,\mathrm{mJ\,cm^{-3}}$, $h_s = 50\,\mu\mathrm{m}$, $h_a = 2{,}000\,\mu\mathrm{m}$, and $s = 1{,}000\,\mathrm{mm\,h^{-1}}$. **(d)** Contributions of individual slices to the accumulated dose curve shown in (c) for $n = 21$ to $n = 53$.

a result, it is important to optimize $\Omega_{\max}$ as well as D_c to ensure good part quality: high doses drive additional cross-linking, improving the part's green strength (i.e., its tensile strength before post-processing) to ensure a rigid and printable structure but also introducing heterogeneous internal stresses that can deform the part. Conversely, low maximum doses with long exposure times might not sufficiently cure the part since flow is not perfectly uniaxial and the resin bath is not infinitely deep. The optimal correction parameters depend in some degree on the irradiation system, the geometry of the part, the flow profile in the resin bath, and the chemical and mechanical properties of the resin.

2.3.2 Experimental Validation

To test the correction algorithm and optimize its parameters, low-absorbance photopolymer resins were prepared (Table 2.1) for use with a previously-described two-color continuous stereolithographic 3D printer [15]. Experimental results are shown in Figure 2.5. The absorbance height h_a and gelation dose D_{gel} were determined from the resin working curves (Figure 2.5(a)), and the test geometry in Figure 2.5(b) was used to investigate the effect of the critical dose parameter on print fidelity. We printed test parts using several values of D_c and an unconstrained maximum dose ($\Omega_{\max} = \infty$), with results shown in Figure 2.5(b–d). Supplying exactly the measured gelation dose (i.e., $D_c = D_{gel}$) results in missing features and poor fidelity; feature sizes increase as D_c increases, and at higher values of D_c cure-through is observed (Figure 2.5(c)). As discussed above, a critical dose higher than the gelation dose is likely required due to the simplifying assumptions used in the correction algorithm and the need for a part of sufficient green strength. For the geometry, resin, and print conditions considered, $D_c = 5D_{gel} = 748\,\mathrm{mJ\,cm^{-3}}$ is the optimal critical dose, achieving a marked improvement in fidelity without reducing print speed (see Figure

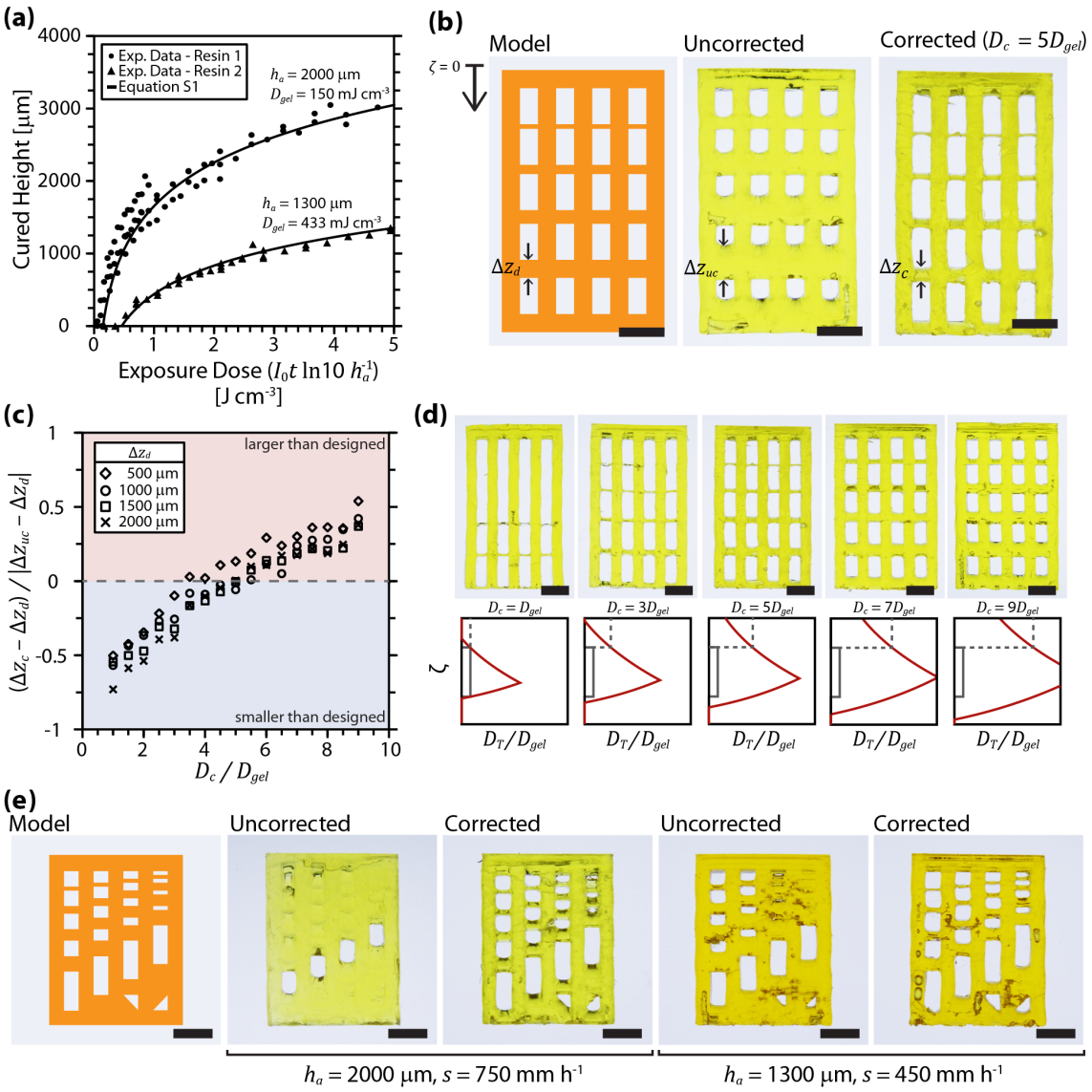

Figure 2.5. Experimental tuning of correction parameters. **(a)** Cured thickness versus exposure dose of blue light for two acrylate-based resins (see Table 2.1) with differing concentrations of blue light absorber. **(b)** Test model (left), uncorrected test part (center), and corrected test part printed with $D_c = 5D_{gel} = 325\,\mathrm{mJ\,cm^{-3}}$ (right). Parts printed in Resin 1 at $750\,\mathrm{mm\,h^{-1}}$. **(c)** Ratio of height errors (corrected-to-uncorrected) for a range of feature sizes and values of D_c. A ratio of zero corresponds to a perfectly corrected feature. **(d)** Parts printed at $750\,\mathrm{mm\,h^{-1}}$ using slices corrected with different values for D_c. **(e)** Corrected and uncorrected test parts for two resins with different absorber loadings (i.e., h_a) and print speeds. All scale bars are 10 mm.

2.5(b)). Additional optimization details are available in Appendix A.5.

To further improve fidelity, the traditional approach of adding dyes or pigments to reduce light propagation can be used in conjunction with slice correction (Figure 2.5(e)). As previously reported, the addition of dyes necessitates slower print speeds [12, 15]. Regardless, applying slice correction at any dye loading or print speed improves the resolution, with higher dye loadings enabling printing of small features with less cure-through.

2.4 Conclusion

In summary, we have demonstrated a method for improving print fidelity on a two-color continuous stereolithographic 3D printer using resins with moderate to high absorbance heights. The approach analyzes and modifies the slice images for a model, using grayscale to precisely tune the dose profile throughout the final printed part. Furthermore, this approach allows control over the dose delivered within features, enabling continuous 3D printing of parts with dose-dependent functionality [57]. Though not demonstrated here, this technique is applicable to other continuous stereolithographic technologies such as CLIP; these methods could also be applied to noncontinuous stereolithography, as outlined in Appendix A.6. Practically, this approach is limited by the resin green strength and the fluid dynamics of resin flow. Models that consider these effects or that vary critical dose with feature height might further improve fidelity. Nevertheless, this approach has afforded significant improvement in print quality for our system while maintaining high print speeds. Slice correction opens the door for the use of less-absorbing resins in stereolithographic systems, enabling faster print speeds and expanding the range of applications for additive manufacturing.

CHAPTER III

Kinetic Curing Model for Uninhibited and Photoinhibited Stereolithography

Parts of this work were completed in collaboration with Dr. Martin de Beer. The work was motivated both by a desire to better characterize our printing resins and to enable single-step fabrication of complex microfluidic devices. My contributions (and this chapter) focus on development and analysis of a curing model for the dual-wavelength system, while the corresponding chapter in Dr. de Beer's dissertation [18] focuses on the fabrication of microfluidic devices. While the majority of the work here is my own, Dr. de Beer contributed some writing, figures, and—as always—provoking discussion. Some elements of this chapter appear in Dr. de Beer's dissertation and will appear in one or more forthcoming co-authored publications on the curing model and dual-wavelength microfabrication.

3.1 Introduction

Much of additive manufacturing research over the past decade has focused on expanding material palettes and developing new applications, and projection stereolithography research is no exception. In projection stereolithography, parts are fabricated by exposing photopolymer resin to a series of cross-sectional images using an LCD or DLP projector [6, 7]. The technique is widely used due to the high

resolution and potential complexity of resulting parts, the diverse range of polymer materials available, and—with the recent development of continuous printing technologies [12, 15, 16]—its rapid production rates. Typically, printing is conducted at the light source's maximum intensity to maximize production rates. However, applications are increasingly being reported that use spatially variable intensity to improve part fidelity [22, 58], enable surface patterning [15], or produce parts with spatially-varying material properties [57, 59, 60]. For this expanding application area, it is critical for resin curing models to accurately capture the relationship between intensity, exposure time, and reaction progress.

The most ubiquitous curing model was initially described by Jacobs in 1992 to characterize resins for laser scanning stereolithography, a predecessor to projection stereolithography [55]. In this framework, the progress of the photopolymerization reaction is assumed to be a function of optical dose, the product of light intensity and exposure time. Resin exposed to an incident dose D cures to a depth z_c, given by

$$z_c = h_a \ln \frac{D}{D_c} \tag{3.1}$$

The model is parameterized by the critical dose D_c, the dose at which resin transitions from a liquid to an insoluble gel, and the absorbance height h_a, the distance over which light is attenuated by a factor of e (or a factor of 10 if the base-10 form of the Beer-Lambert Law is used). These parameters are determined from cured height experiments, in which samples of resin are exposed at a constant intensity for varying lengths of time. Plotting the height of each cured sample as a function of incident dose yields the Jacobs working curve for the resin.

While the Jacobs model is still widely used in projection stereolithography, its accuracy may be limited in applications using variable intensities. By treating cur-

ing as a function of optical dose, the Jacobs model implicitly accepts the validity of the *reciprocity law*, the assumption that the reaction rate, and thus material properties of the resin, depends on the product of light intensity and exposure time but not the parameters' independent values. Work by Wydra, *et al.* [61], however, has argued that its use in photopolymerization is flawed: while the reciprocity law is valid for primary photochemical reactions (e.g., initiator cleavage), secondary reactions (e.g., termination)—or processes that depend on them (e.g., the overall rate of polymerization)—can vary nonlinearly with light intensity. In the most general form, the rate of polymerization is taken to vary with I^m, where I is light intensity and m is a parameter reflecting the radical termination mechanism(s) and is fit from experimental data. The power-law relationship would not be apparent in experiments conducted at constant intensity; however, in a resin where the reciprocity assumption is invalid, variable intensity experiments could not be accurately described using the Jacobs model.

A number of curing models have been used in the literature for layer-by-layer stereolithography [62, 63, 64], CLIP [19, 12, 56, 65], and dual-wavelength continuous stereolithography [15, 66, 20, 21]. However, to our knowledge, none have maintained the simple cured-height characterization method of the Jacobs approach (complex kinetic models, for example, tend to rely on FTIR spectroscopy or require knowledge of the reaction rate constants) while allowing for an unknown nonlinear dependence on light intensity. Here, we propose such a model for uninhibited photopolymerization (as used in layer-by-layer projection stereolithography) and photoinhibited photopolymerization (as used in dual-wavelength continuous stereolithography). As with the Jacobs working curve, resin is characterized via straightforward cured height experiments, with the cured height varying as a function of light intensity and expo-

sure time. In addition to theoretical results, we provide experimental verification of the model for both uninhibited and photoinhibited resins.

3.2 Materials and Methods

3.2.1 Materials

Commercial resins for layer-by-layer projection stereolithography were chosen to represent a range of manufacturers, printing resolutions, and colors. The resins used are Standard Clear (Formlabs), Standard Yellow (MakerJuice, equivalent to MakerJuice G+ used in Ref. [57]), and PR57-Black (Colorado Polymer Solutions). Resins were ordered directly from the manufacturer and used as received.

Custom resins for photoinhibited continuous stereolithography were formulated according to the compositions in Table 3.1. Resins were formulated as a mixture of oligomer, reactive diluent, initiator, inhibitor, and light absorbers. The oligomer used was a proprietary acrylate blend CN991 (Sartomer), with 1,6-hexanedioldiacrylate (HDDA, TCI America) as a reactive diluent. DL-Camphorquinone (CQ, Fisher Scientific) and ethyl 4-(dimethylamino)benzoate (EDAB, ACROS Organics) were used as the blue-light initiator and co-initiator, respectively. 2,2'-Bis(2-chlorophenyl)-4,4',5,5'-tetraphenyl-1,2'-biimidazole (*o*-Cl-HABI, Hampford Research Inc.) was used as the UV-light inhibitor. Resins were prepared by dissolving CQ, EDAB, and *o*-Cl-HABI in a small amount of tetrahydrofuran (THF, ACROS Organics) and combining with the oligomer and reactive diluent. Solvent was removed by evaporation under airflow followed by degassing under vacuum. Uncured resin is rinsed away in cured height and dead zone experiments using isopropanol (IPA, laboratory grade, Fisher Scientific).

Table 3.1. Custom resin formulations.

Component	Function	Concentration (wt.%) Resin 1	Resin 2
CQ	photoinitiator	1.9	1
EDAB	co-initiator	0.94	0.5
o-Cl HABI	photoinhibitor	2.8	2.5
Tinuvin 328	UV absorber	0.46	–
Epolight 5675	blue light absorber	0.004	0.01
CN991	oligomer	55.7	40
HDDA	reactive diluent	37.2	55
TMSPM	adhesion promoter	–	0.01

3.2.2 Exposure Setup

Cured height experiments for commercial resins were conducted using an Ember 3D printer (Autodesk). Cured height and dead zone experiments for custom resins were conducted using a custom dual-wavelength continuous 3D printer [15]. Blue light is produced from a DLP projector (Optoma ML750), which has been modified by removing the red and green channels. UV light is produced from a light emitting diode (Thorlabs, M365LP1) and passes through an adjustable collimation adapter (Thorlabs, SM2F) and an aspheric condenser lens (Thorlabs, ACL50832U). Blue and UV light is superimposed using a longpass dichroic mirror (Thorlabs, DMLP425L), and the setup is controlled using a custom LabVIEW virtual instrument.

For each light source, a calibration curve for incident light intensity was produced using a digital radiometer (International Light Technologies, ILT2400) with a UV-Vis GaAsP detector (International Light Technologies, SED005/U) and a 10× attenuation filter (International Light Technologies, QNDS2). For the Ember, UV intensity (365 nm) was calibrated as a function of grayscale pixel value. For the dual-wavelength printer, blue intensity (460 nm) was calibrated as a function of grayscale pixel value and LED input voltage, and UV intensity was calibrated as a function of LED input voltage. Calibration curves are available in Appendix B.1.

3.2.3 Cured Height Experiments

Cured height experiments were conducted to determine the cured height as a function of time and incident intensity for each resin. Wells were constructed by affixing a 3D printed enclosure to 50-by-75-mm glass microscope slides. For each experiment, the well was filled with resin and exposed to a series of constant-intensity images designed such that each region of a grid would be exposed for a different time interval. Between experiments, the intensity was varied using a MATLAB script to modify the image files. For experiments at the maximum intensity, time intervals ranging from 1 s to 32 s were used. At lower intensities, time intervals were chosen such that the incident doses were constant for each grid point across all intensities (e.g., if Δt for a grid point at $I = I_1$ is 1 s, Δt for that grid point at $I = \frac{1}{2}I_1$ is 2 s). Uncured resin was rinsed from the part using IPA, and the height of the cured resin was measured using a digital micrometer (Tormach) with an accuracy of $\pm 2\,\mu$m. Cured height experiments were conducted in triplicate.

For the custom continuous-printing resins, cured height experiments were conducted using blue (initiating) light only. These samples were post-cured under white light for 60 s after rinsing with IPA.

3.2.4 Dead Zone Experiments

Dead zone experiments were conducted for custom photoinhibited resins to determine the steady-state dead zone height as a function of the blue-UV intensity ratio. Two 50-by-75-mm glass microscope slides were separated by spacers of known thickness, and the gap between slides was filled with resin. Samples were exposed for 30 s to variable intensity images designed such that each region of a grid would be exposed to a different blue intensity while UV intensity was held constant. As

a result, each region of the grid was exposed at a different blue-UV intensity ratio. Uncured resin was rinsed from between the slides using IPA, and the sample was post-cured under white light for 30 s. The thickness of the cured resin was measured as above, and the dead zone height is determined by subtracting the measured resin thickness from the known spacer thickness.

3.3 Model Development

Here, we present derivations for the uninhibited and inhibited curing models. Curing models are developed assuming a single, stationary exposure—that is, under resin characterization conditions, not printing conditions.

3.3.1 Uninhibited Curing Model

The standard configuration for a projection stereolithography 3D printer is shown in Figure 3.1(a) and (b). Light is projected into the bottom of the resin bath while the build platform is stationary. Resin is cured in the gap between the window and the resin to form a layer before the part is separated and repositioned for the next layer. Following a common approach for free radical photopolymerization [67, 19], the following simplified reaction scheme is used for uninhibited exposure:

$$\text{photolysis} \qquad \mathrm{PI} \xrightarrow{h\nu} \mathrm{R}^{\bullet} \tag{R 3.1}$$

$$\text{chain initiation} \qquad \mathrm{R}^{\bullet} + \mathrm{M} \longrightarrow \mathrm{RM}^{\bullet} \tag{R 3.2}$$

$$\text{chain propagation} \qquad \mathrm{RM}_n^{\bullet} + \mathrm{M} \xrightarrow{k_p} \mathrm{RM}_{n+1}^{\bullet} \tag{R 3.3}$$

$$\text{chain termination} \qquad \mathrm{RM}_n^{\bullet} + \mathrm{RM}_m^{\bullet} \xrightarrow{k_t} \mathrm{RM}_n\mathrm{M}_m \tag{R 3.4}$$

In Reaction R 3.1, incident light ($h\nu$) photolyzes the photoinitiator (PI) to produce primary radicals ($\mathrm{R}^{\bullet}$). In Reaction R 3.2, primary radicals initiate growing polymer chains ($\mathrm{RM}^{\bullet}$) by reacting with a double bond in the monomer (M). In Reaction R 3.3,

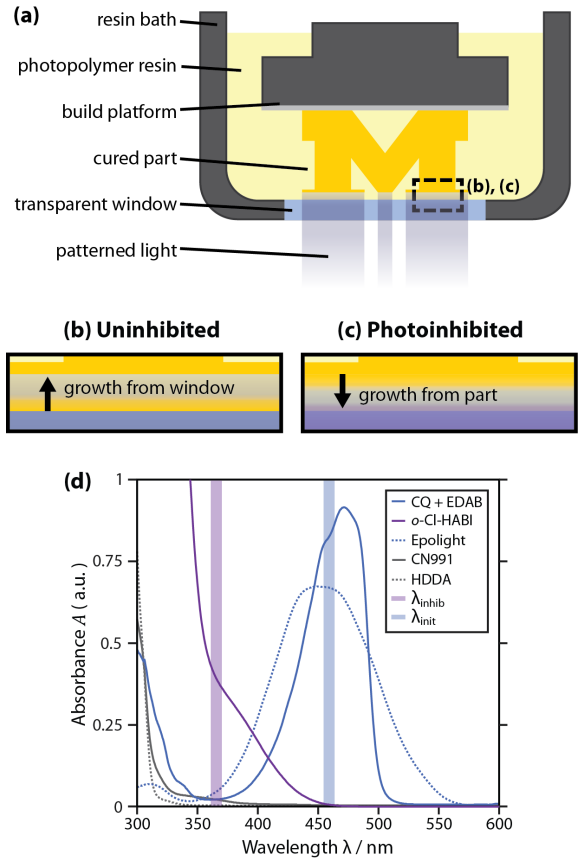

Figure 3.1. Uninhibited and photoinhibited projection stereolithography. **(a)** General printer configuration for projection stereolithography, **(b)** In standard, uninhibited stereolithography, resin in the gap between the part and the window is cured to form discrete layers. **(c)** In dual-wavelength continuous stereolithography, a dead zone is generated near the window, preventing polymerization. As a result, resin cures from the part downward and continuous printing is enabled. **(d)** Absorbance spectra of custom resin components diluted in tetrahydrofuran (THF) to concentrations, in wt.%, of 25, 6, 0.4, 0.06, and 2.3×10^{-4} for HDDA, CN991, CQ+EDAB, *o*-Cl-HABI, and Epolight 5675 respectively. The emission wavelength of the initiating and inhibiting light sources used in experiments are shown in with shaded blue and purple boxes.

chains continue to grow by reacting with monomer. In Reaction R 3.4, termination occurs as two growing chains combine. For Reactions R 3.3 and R 3.4, k_p and k_t (respectively) are the reaction rate constants.

Two primary simplifications are made in deriving the model. First, rather than considering growing chains of different lengths individually, we lump all radical species into a single term, $X^{\bullet}$. All radical species are thus assumed to have similar reactivity. Second, we assume the radical concentration quickly settles at a constant value (i.e., the steady-state approximation [67]). Radicals are generated in Reaction R 3.1 and consumed in Reaction R 3.4; Reactions R 3.2 and R 3.3 result in no net generation or consumption of radicals. Thus,

$$\frac{\partial[X^{\bullet}]}{\partial t} = R_{3.1} - 2R_{3.4} = 0 \tag{3.2}$$

where $[X^{\bullet}]$ is the radical concentration, $R_{3.1}$ is the rate of Reaction R 3.1 and $R_{3.4}$ is the rate of Reaction R 3.4.

The rate of radical generation is proportional to the rate of photon absorption:

$$R_{3.1} = -\varphi\frac{\partial I(z)}{\partial z} \tag{3.3}$$

where φ is the quantum yield and $I(z)$ is the light intensity as a function of depth into the resin. From the Beer-Lambert Law,

$$\frac{\partial I(z)}{\partial z} = -I_0 h_a^{-1} e^{-z/h_a} \tag{3.4}$$

where h_a is the absorbance height, the distance over which intensity is attenuated by a factor of e, and I_0 is the incident light intensity. For clarity, it is worth noting that the absorbance height is sometimes reported as the distance over which the intensity is attenuated by a factor of 10; the appropriate value depends on whether the base-e or base-10 form of the Beer-Lambert Law is used. Substituting Equation 3.4 into

Equation 3.3,

$$R_{3.1} = \varphi I_0 h_a^{-1} e^{-z/h_a} \tag{3.5}$$

In Reaction R 3.4, two radicals are consumed to produce a dead polymer chain; however, in reality a range of termination mechanisms exist. To account for the unknown mixture of mechanisms occurring for each resin composition, we replace the coefficient 2 with the termination parameter m [61, 20]. The rate of radical consumption is thus:

$$R_{3.4} = k_t[\mathrm{X}^\bullet]^{1/m} \tag{3.6}$$

Substituting Equations 3.5 and 3.6 into Equation 3.2 and rearranging,

$$[\mathrm{X}^\bullet] = \left(\frac{\varphi I_0 e^{-z/h_a}}{m k_t h_a}\right)^m \tag{3.7}$$

Equation 3.7 gives the steady-state concentration of radicals while the resin is exposed to initiating light.

Ultimately, our goal is to relate the degree of curing to the incident intensity and exposure time. The threshold for curing is generally set at the gelation point, which is assumed to occur at a critical double bond conversion. $\xi \equiv [\mathrm{M}]/[\mathrm{M}]_0$ gives the fraction of double bonds which remain unreacted and can be written from the rate of Reaction R 3.3:

$$\frac{\partial[\mathrm{M}]}{\partial t} = -k_p[\mathrm{X}^\bullet][\mathrm{M}] \tag{3.8}$$

$$\frac{\partial \xi}{\partial t} = -k_p[\mathrm{X}^\bullet]\xi \tag{3.9}$$

Next, we substitute $[\mathrm{X}^\bullet]$ from Equation 3.7, combine constants into $K \equiv k_p(\varphi h_a^{-1}/m k_t)^m$, and solve the differential equation:

$$\frac{\partial \xi}{\partial t} = -K\left(I_0 e^{-z/h_a}\right)^m \xi \tag{3.10}$$

$$\xi = \exp\left[-K\left(I_0 e^{-z/h_a}\right)^m t\right] \tag{3.11}$$

Rearranging,

$$-\frac{\ln \xi}{K} = \left(I_0 e^{-z/h_a}\right)^m t \tag{3.12}$$

Equation 3.12 appears to be a good candidate as an expression relating the degree of curing to intensity and exposure time: the left-hand side is a function of the double bond conversion, and the right-hand side resembles the standard definition for dose, $D = I(z)t$, albeit with the expected power-law dependence on intensity. Thus, we define the dose analogue $D' \equiv -\ln \xi / K$:

$$D'(z) = \left(I_0 e^{-z/h_a}\right)^m t \tag{3.13}$$

The dose analogue D' has units of $(\mathrm{mW\,cm^{-2}})^m\,\mathrm{s}$.

The Jacobs model is generally used in the form of the cured height equation, Equation 3.1. A similar expression can be obtained from Equation 3.13. Assuming that the gelation point occurs at the critical dose D'_c (corresponding to a critical double-bond conversion) and solving for the cured height z_c,

$$D'_c = \left(I_0 e^{-z/h_a}\right)^m t \tag{3.14}$$

$$z_c = \frac{h_a}{m} \ln\left(\frac{I_0^m t}{D'_c}\right) \tag{3.15}$$

Equation 3.15 is analogous to the Jacobs cured height equation and can similarly be used to generate working curves and characterize resins. Unlike the Jacobs expression, it accommodates resins for which the reciprocity assumption is invalid by introducing the termination parameter m.

3.3.2 Photoinhibited Curing Model

In dual-wavelength continuous stereolithography, initiation and inhibition are effected by orthogonal radical-generating reactions active at different wavelengths on the electromagnetic spectrum. The printer configuration is shown in Figure 3.1(a)

and (c). In this system, camphorquinone (CQ) and ethyl 4-(dimethylamino) benzoate (EDAB) readily generate initiating radicals under visible light irradiation. When irradiated with ultraviolet (UV) light, *o*-Cl-HABI (2,2'-Bis(2-chlorophenyl)-4,4',5,5'-tetraphenyl-1,2'-biimidazole) generates stable, non-reactive radicals, which have been demonstrated to inhibit curing in a wide range of (meth)acrylate resins by recombining with propagating carbon-centered radicals during polymerization. Concurrent irradiation of visible and UV light into a vat of photopolymer (formulated with CQ, EDAB, and *o*-Cl-HABI), results in a photoinhibited dead zone above the incident surface. Initiation and inhibition are controllable with two independent wavelengths (here we use $\lambda_{\text{init}} = 455\,\text{nm}$ and $\lambda_{\text{inhib}} = 365\,\text{nm}$) due, not only to favourable chemistry [68, 15], but also to complementary absorbance spectra (Figure 3.1(d)). *o*-Cl-HABI absorbs strongly below 400 nm and, fortuitously, CQ/EDAB has a region of exceptionally low absorbance from 350–375 nm while absorbing strongly from 450–500 nm allowing chemically orthogonal processes to be activated under irradiation with visible light and UV light. The thickness of this dead zone is dependent on the resin properties and, more importantly, the intensity of the incident visible and ultraviolet light.

To model curing in the dual-wavelength system, we extend the uninhibited model to describe gelation under concurrent initiation and inhibition. Under concurrent exposure from blue and UV light, inhibitor photolysis and chain inhibition are added

to the reaction scheme:

initiator photolysis	$\mathrm{PI} \xrightarrow{h\nu} \mathrm{R}^\bullet$	(R 3.5)
inhibitor photolysis	$\mathrm{PZ} \xrightarrow{h\nu} \mathrm{Z}^\bullet$	(R 3.6)
chain initiation	$\mathrm{R}^\bullet + \mathrm{M} \longrightarrow \mathrm{RM}^\bullet$	(R 3.7)
chain propagation	$\mathrm{RM}_n^\bullet + \mathrm{M} \xrightarrow{k_p} \mathrm{RM}_{n+1}^\bullet$	(R 3.8)
chain termination	$\mathrm{RM}_n^\bullet + \mathrm{RM}_m^\bullet \xrightarrow{k_t} \mathrm{RM}_n\mathrm{M}_m$	(R 3.9)
chain inhibition	$\mathrm{RM}_n^\bullet + \mathrm{Z}^\bullet \xrightarrow{k_z} \mathrm{RM}_n\mathrm{Z}$	(R 3.10)

The dual-wavelength derivation will follow the same pattern as the blue-only derivation above. The steady state approximation is applied to both $\mathrm{X}^\bullet$ and $\mathrm{Z}^\bullet$:

$$\frac{\partial[\mathrm{X}^\bullet]}{\partial t} = R_{3.5} - 2R_{3.9} - R_{3.10} = 0 \tag{3.16}$$

$$\frac{\partial[\mathrm{Z}^\bullet]}{\partial t} = R_{3.6} - R_{3.10} = 0 \tag{3.17}$$

Subtracting Equation 3.17 from Equation 3.16 and substituting for the reaction rates,

$$\varphi_b I_{b,0} h_b^{-1} e^{-z/h_b} - \varphi_{uv} I_{uv,0} h_{uv}^{-1} e^{-z/h_{uv}} - m k_t [\mathrm{X}^\bullet]^{1/m} = 0 \tag{3.18}$$

$$[\mathrm{X}^\bullet] = \left(\frac{\varphi_b I_{b,0} h_b^{-1} e^{-z/h_b} - \varphi_{uv} I_{uv,0} h_{uv}^{-1} e^{-z/h_{uv}}}{m k_t} \right)^m \tag{3.19}$$

As above, the differential equation for $\xi \equiv [\mathrm{M}]/[\mathrm{M}]_0$ can be solved to find the dose analogue $D' \equiv -\ln \xi / K$. Here, we will substitute the previously defined constant $K = k_p(\varphi_b h_b^{-1}/m k_t)^m$ as well as the newly defined inhibition constant $\beta \equiv \varphi_{uv} h_{uv}^{-1} / \varphi_b h_b^{-1}$.

$$\frac{\partial \xi}{\partial t} = -K \left(I_{b,0} e^{-z/h_b} - \beta I_{uv,0} e^{-z/h_{uv}} \right)^m \xi \tag{3.20}$$

$$\xi = \exp\left[-K \left(I_{b,0} e^{-z/h_b} - \beta I_{uv,0} e^{-z/h_{uv}} \right)^m t \right] \tag{3.21}$$

$$D'(z) = \left(I_{b,0} e^{-z/h_b} - \beta I_{uv,0} e^{-z/h_{uv}} \right)^m t \tag{3.22}$$

D' again has units of $(\mathrm{mW\,cm^{-2}})^m\,\mathrm{s}$. Here, we see that UV exposure, which drives inhibition, effectively acts as "negative dose," and thus requires additional blue exposure, which drives initiation, to reach the critical dose. We note also that Equation 3.20 is suggestive of the previously reported relationship between reaction rate and intensities for a photoinhibited system [20].

Note that Equation 3.25 has two solutions at each time: the frontside and backside curing fronts (z_f and z_b, respectively). It is not possible to isolate z_c in the concurrent exposure equations, and parameters generally must be fit to Equation 3.22. However, an analytical solution can be found in the limit $t \to \infty$. In the case of the frontside curing front (i.e., the dead zone height) the solution must remain finite. Examining Equation 3.22, D' can only remain finite as t approaches infinity if the expression in parentheses approaches zero. Thus,

$$I_{b,0}e^{-z_{f,\infty}/h_b} - \beta I_{uv,0}e^{-z_{f,\infty}/h_{uv}} = 0 \tag{3.23}$$

$$e^{z_{f,\infty}(h_{uv}^{-1}-h_b^{-1})} = \frac{\beta I_{uv,0}}{I_{b,0}} \tag{3.24}$$

$$z_{f,\infty} = \frac{\ln\left(\frac{\beta I_{uv,0}}{I_{b,0}}\right)}{h_{uv}^{-1} - h_b^{-1}} \tag{3.25}$$

Equation 3.25 matches the previously reported steady-state dead zone equation [15] and is the position where the rate of initiator photolysis $R_{3.5}$ is equal to the rate of inhibitor photolysis $R_{3.6}$. The frontside curing front asymptotically approaches the steady-state position; the backside curing front continues to grow indefinitely.

3.4 Results and Discussion

3.4.1 Commercial Resins for Layer-by-Layer Projection Stereolithography

Figure 3.2 conceptually illustrates the behavior for hypothetical resins where the reciprocity assumption is or is not valid. When the reciprocity law applies, cured

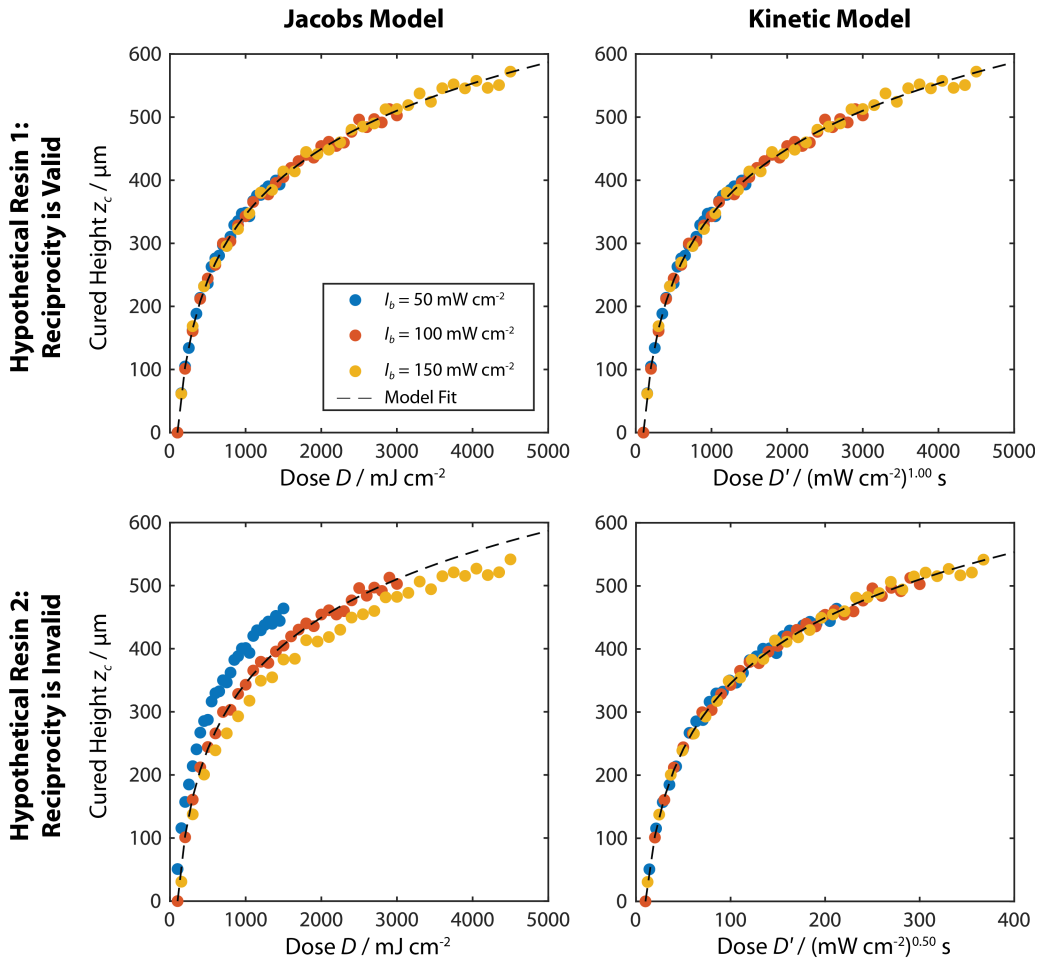

Figure 3.2. Comparing cured height results and model fitting for two hypothetical resins: one where the reciprocity assumption is valid and one where it is not.

heights for a wide range of intensities fall along a single curve when plotted against incident dose (i.e., in the Jacobs working curve). A fit of the kinetic model to this data results in a very similar curve, with $m \approx 1$. Note that for $m = 1$, the cured height expression for the kinetic model (Equation 3.15) reduces to the Jacobs model expression (Equation 3.1).

In cases where the reciprocity assumption is invalid, cured height data for different intensities *do not* collapse onto a single curve when plotted against dose; however, the kinetic model accurately captures the effect of intensity and collapses the data onto a single curve. Note that the resulting "dose equivalent" has unusual units that depend on the value of m: $(\mathrm{mW\,cm^{-2}})^m\,\mathrm{s}$. For this hypothetical resin $m = 0.5$, a value which is within the reported range for acrylates [61].

Experimental cured height results for commercial resins are shown in Figure 3.3. For each of the resins considered, both the standard Jacobs model and our kinetic model provide good fits for the data. Because the Jacobs model fits the data well and $m \approx 1$ for the kinetic model (varying from about 0.9 to 1.1), the reciprocity assumption is valid for these resins. These limited results suggest that the Jacobs model may be sufficient for many commercial 3D printing resins; however, while the selected resins represent a range of manufacturers, printing resolutions, and colors, they are all general-purpose resins and were used promptly after delivery from the manufacturer. Since the value of m is known to vary for different oligomers, these results should not be extrapolated to specialized resins, which are formulated using different oligomer blends to achieve particular material properties (e.g., flexibility, temperature resistance, or biocompatibility). In our experience, we have also noticed that expired or otherwise degraded resins do not adhere to the reciprocity law.

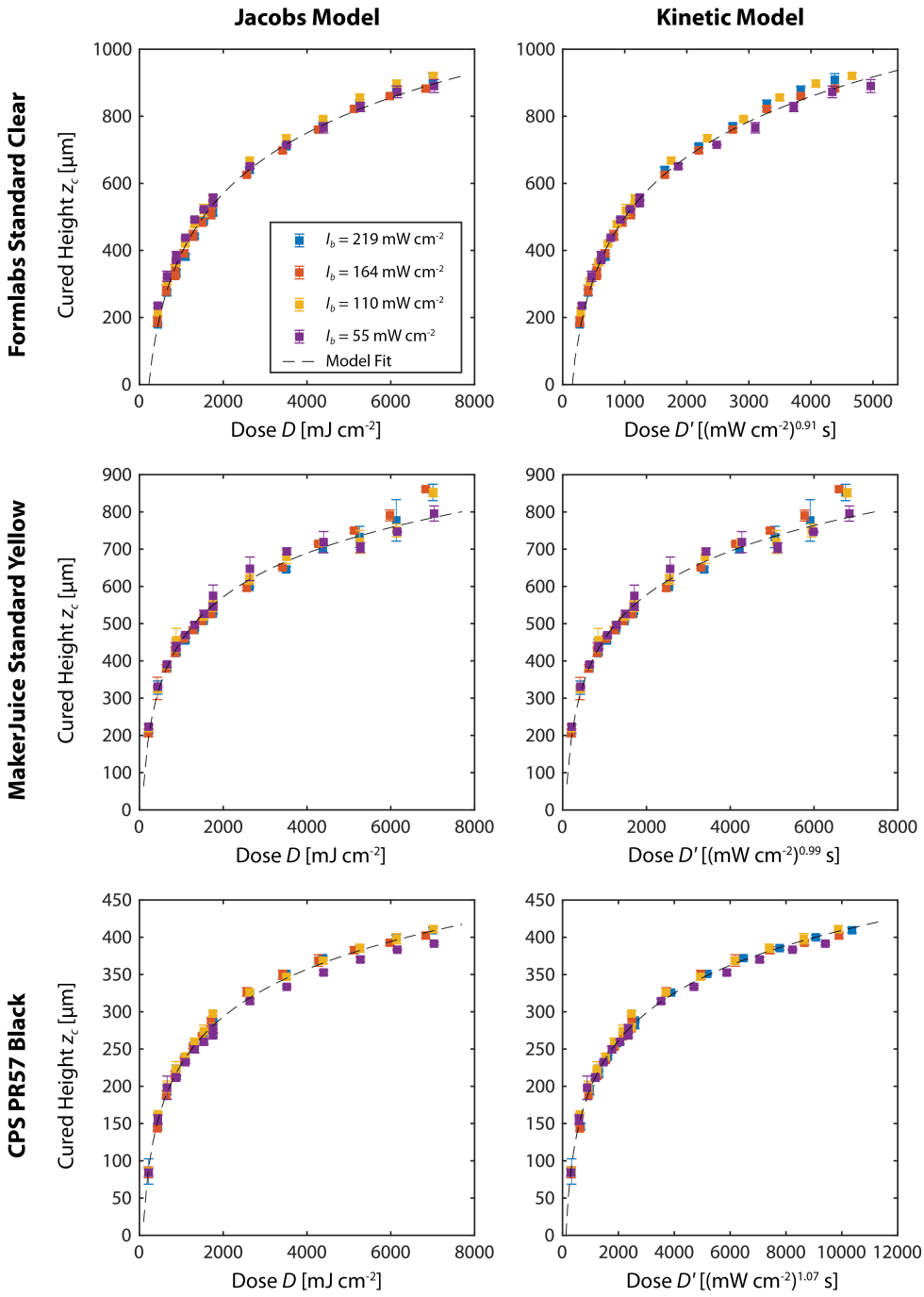

Figure 3.3. Characterization of commercial resins. Each plot shows cured height as a function of incident dose (standard optical dose D for the Jacobs model and the dose analogue D' for the kinetic model). Parameters were fit using a least-squares regression. For Formlabs Standard Clear, the Jacobs model parameters are $D_c = 223\,\mathrm{mJ\,cm^{-2}}$ and $h_a = 260\,\mu\mathrm{m}$ ($R^2 = 0.992$). The kinetic model parameters are $D'_c = 148\,(\mathrm{mW\,cm^{-2}})^{0.91}\,\mathrm{s}$, $h_a = 238\,\mu\mathrm{m}$, and $m = 0.91$ ($R^2 = 0.994$). For MakerJuice Standard Yellow, the Jacobs model parameters are $D_c = 69\,\mathrm{mJ\,cm^{-2}}$ and $h_a = 170\,\mu\mathrm{m}$ ($R^2 = 0.983$), and the kinetic model parameters are $D'_c = 67\,(\mathrm{mW\,cm^{-2}})^{0.99}\,\mathrm{s}$, $h_a = 168\,\mu\mathrm{m}$, and $m = 0.99$ ($R^2 = 0.983$). For CPS PR57 Black, the Jacobs model parameters are $D_c = 82\,\mathrm{mJ\,cm^{-2}}$ and $h_a = 92\,\mu\mathrm{m}$ ($R^2 = 0.994$), and the kinetic model parameters are $D'_c = 117\,(\mathrm{mW\,cm^{-2}})^{1.07}\,\mathrm{s}$, $h_a = 99\,\mu\mathrm{m}$, and $m = 1.07$ ($R^2 = 0.996$).

3.4.2 Custom Resins for Photoinhibited Continuous Stereolithography

Theoretical Model Results

From Equation 3.22, we can examine the photoinhibited model's equivalent of a cured height plot: the curing front plot. Figure 3.4 shows the development of the curing front over time and the effects of model parameters. In dual-wavelength stereolithography, liquid resin is simultaneously exposed to blue and UV light (Figure 3.4(a)). At time t_0, the critical dose is reached at height z_0 and the first infinitesimally thin volume of resin is gelled, corresponding to the leftmost point of the curing front curve in Figure 3.4(b). This is comparable to the critical time t_c in the traditional Jacobs model. At $t = t_c$ in an uninhibited resin, the first spot of resin gels on the surface of the window; in inhibited resins, this initiation point is above the surface of the resin due to the existence of a dead zone. The location of the initiation point can be determined from Equation 3.22 and is discussed in Appendix B.3. As exposure continues, the backside curing front z_b rapidly progresses as the frontside curing front z_f slowly approaches its steady-state value.

It has been previously noted that Equation 3.22 cannot be directly solved for z_c; however, it is apparent from Figure 3.4(b) that after an initial period, the frontside curing front can be approximated by the steady-state dead zone solution (Equation 3.25) and the backside curing front can be approximated by the uninhibited model solution (Equation 3.15). Figure 3.5 shows the steady-state dead zone solution (uninhibited model solutions are discussed in the previous section). The steady-state dead zone height depends on the log of the intensity ratio (Figure 3.5(a)) and so while $z_{f,\infty}$ is theoretically unbounded as the ratio increases, diminishing returns place a practical limit on the dead zones achievable by increasing the UV/blue ratio. At the other extreme, an effective minimum intensity ratio arises because for $\beta I_{uv}/I_b \leq 1$,

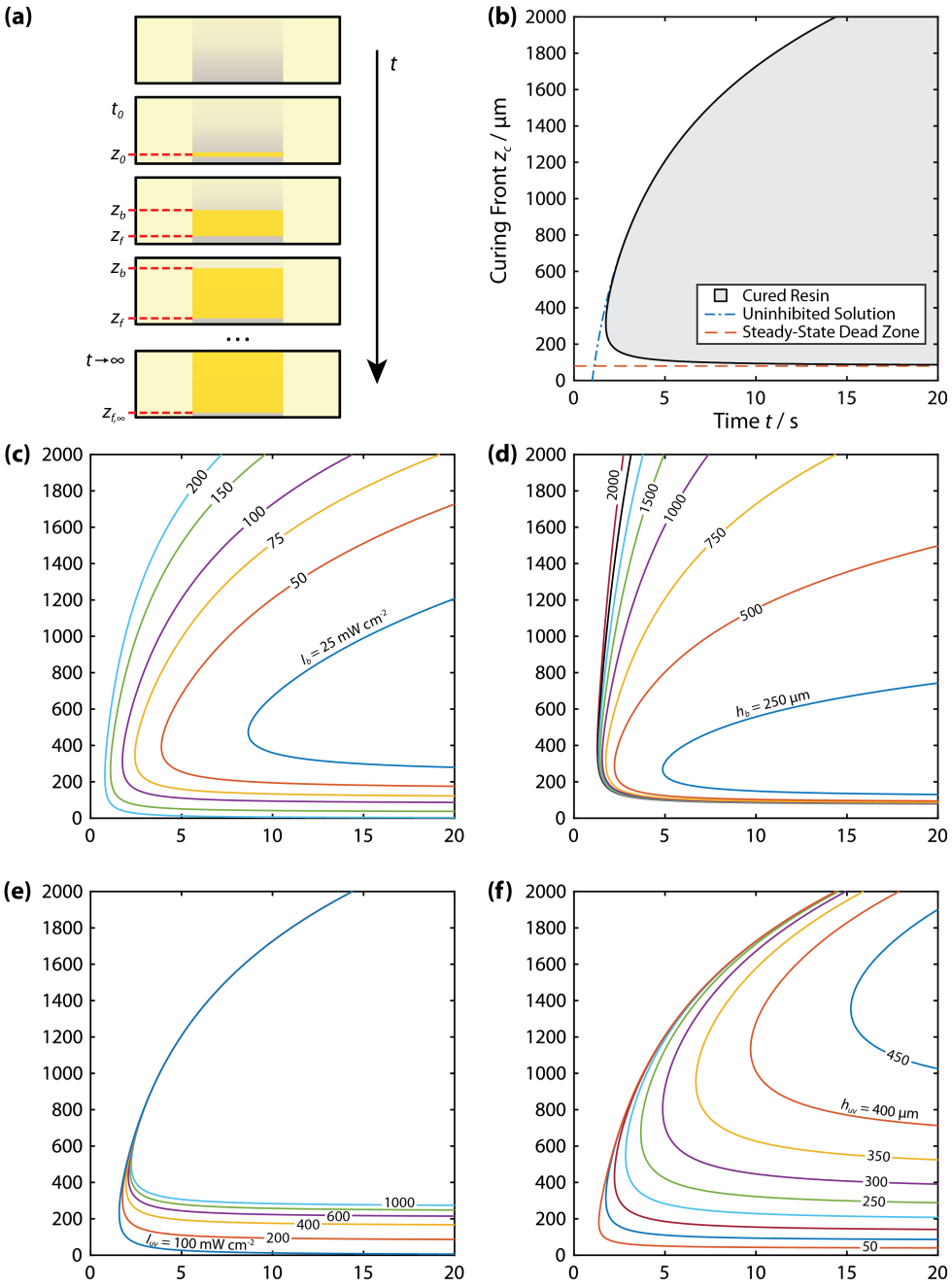

Figure 3.4. Development of the curing front over time and the effect of blue intensity, blue absorbance height, UV intensity, and UV absorbance height. **(a)** Diagram showing cured part growth over time with the initiation point z_0, the backside curing front z_b, and the frontside curing front z_f indicated. **(b)** Plot of cured part growth over time. The curve itself traces the movement of the curing front, while the area inside the curve (shaded in this plot) represents cured resin. After a brief period, the frontside curing front z_f tends towards the steady-state dead zone height $z_{f,\infty}$ while the backside curing front z_b tends towards the solution from the uninhibited model. Remaining plots show the effect of **(c)** blue intensity, **(d)** blue absorbance height, **(e)** UV intensity, and **(f)** UV absorbance height on the curing front. Parameters other than the variable of interest are held constant at $I_b = 100\,\mathrm{mW\,cm^{-2}}$, $h_b = 750\,\mu\mathrm{m}$, $I_{uv} = 200\,\mathrm{mW\,cm^{-2}}$, $h_{uv} = 100\,\mu\mathrm{m}$, $\beta = 1$, $m = 1$, and $D_c' = 100\,\mathrm{mJ\,cm^{-2}}$.

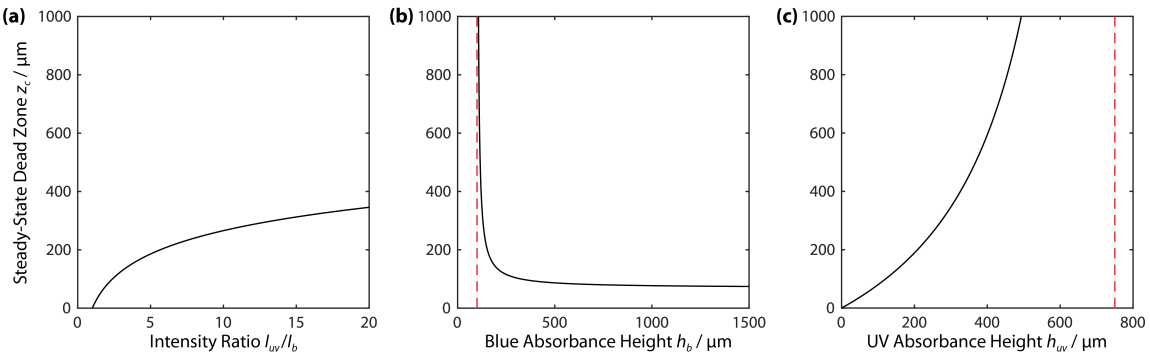

Figure 3.5. Steady-state dead zone height (Equation 3.25) and the effect of **(a)** UV/blue intensity ratio, **(b)** blue absorbance height, and **(c)** UV absorbance height. Parameters other than the variable of interest are held constant at $I_{uv}/I_b = 2$, $h_b = 750\,\mu\text{m}$, and $h_{uv} = 100\,\mu\text{m}$. For (b) and (c), red dashed line indicates the asymptotic limit at which $h_b = h_{uv}$.

$z_{f,\infty} = 0$ and resin cures to the window, thus preventing continuous printing. A more effective route to increase the dead zone thickness is by varying the blue and UV absorbance heights via the addition of light absorbers to the resin formulation. By adding blue light absorbers or reducing UV light absorbers, $z_{f,\infty}$ can be significantly increased (though the overall curing time is also increased, as shown in Figures 3.4(d) and (f)). For continuous printing, it is necessary that $h_b \geq h_{uv}$, indicated by red dashed lines in Figures 3.5(b) and (c). In the case where both $h_{uv} > h_b$ and $I_b > \beta I_{uv}$, a dead zone again exists—albeit on the "wrong" side of (above) the curing region.

Yet while the steady-state dead zone solution depends only on the ratio of blue and UV intensities, the independent values of the blue *and* UV intensities are important in determining the time-dependent approach to the asymptotic solutions. As shown in Figure 3.6(a), the curing front is significantly affected by the blue intensity even at a constant intensity ratio. The time to the initiation point t_0 is significantly longer at low blue intensities, though it only weakly varies with the intensity ratio (Figure 3.6(b)). The effect is similar on the time to reach the uninhibited solution (calculated as the time at which z_b is 90% of the uninhibited value—the actual approach is asymptotic). The time to reach the steady-state dead zone (the time at

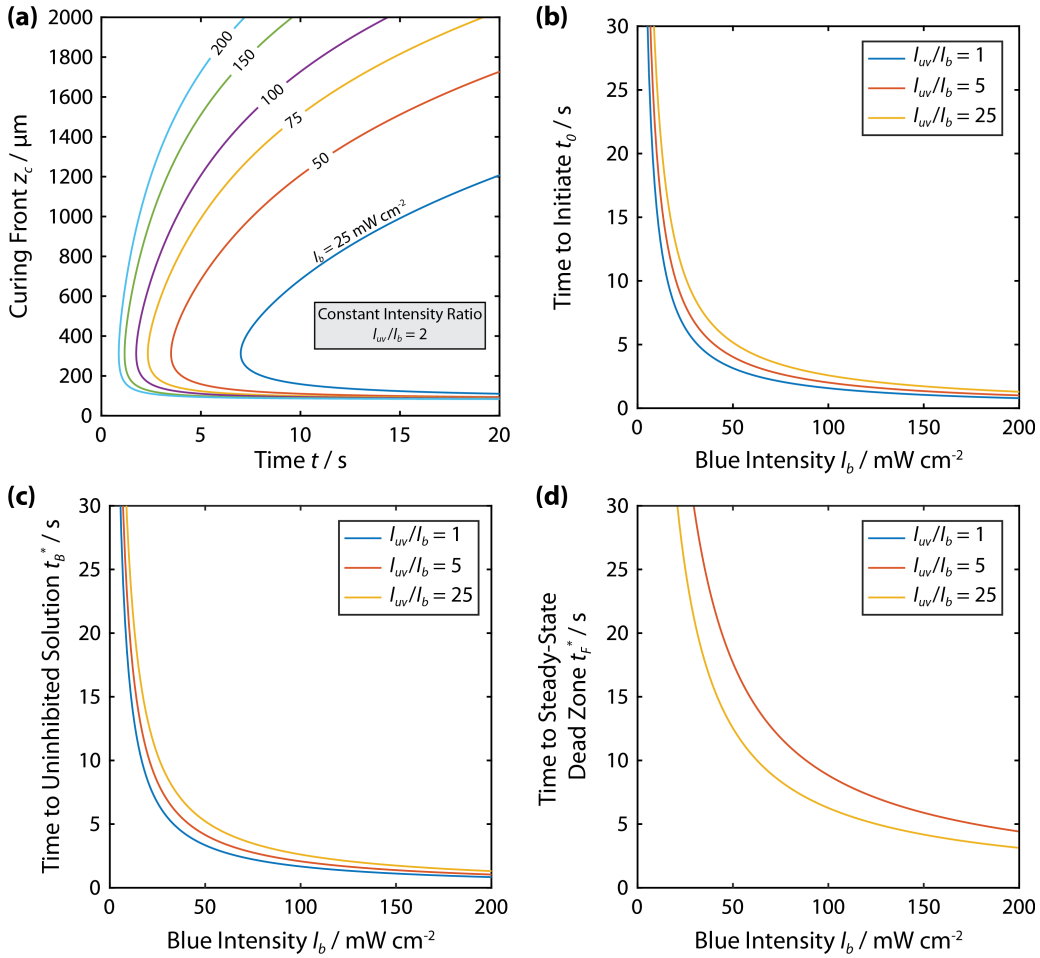

Figure 3.6. Effect of independent intensities at constant intensity ratio. Other parameters are held constant at $h_b = 750\,\mu\text{m}$, $h_{uv} = 100\,\mu\text{m}$, $\beta = 1$, $m = 1$, and $D' = 100\,\text{mJ}\,\text{cm}^{-2}$. **(a)** The development of the curing front is significantly affected by the blue intensity, even at constant intensity ratio. **(b)** Time to the initiation point as a function of blue intensity at constant intensity ratio. **(c)** Time for z_b to reach 90% of the uninhibited solution at varying blue intensity and constant intensity ratio. **(d)** Time for z_f to reach 110% of $z_{f,\infty}$ at varying blue intensity and constant intensity ratio. $I_{uv}/I_b = 1$ is not visible since no dead zone exists for $\beta I_{uv}/I_b \leq 1$.

which z_f is 110% of $z_{f,\infty}$) is highly dependent on the UV intensity (Figure 3.6(d)). As a result, the time decreases when I_b is increased at a constant intensity ratio (since I_{uv} also increases) and when the intensity ratio increases at constant I_b. Note that since an intensity ratio of one produces a dead zone thickness of zero, the time to reach 110% is infinite.

Resin Characterization Results

We prepared two custom photoinhibited resins to demonstrate model's capability in resin characterization. The identity, concentration, and function of resin components is summarized in Table 3.1. Resin 1 is a fairly typical printing resin for dual-wavelength continuous stereolithography, while Resin 2 is optimized for dual-wavelength microfabrication [18].

The CQ, EDAB, and *o*-Cl-HABI photoinitiation/photoinhibition system is applicable to a wide range of acrylate and methacrylate monomers. However, monomer choice is not arbitrary: properties such as viscosity, reactivity, susceptibility to inhibition, and optical transparency must be carefully considered. The viscosity of CN991 (660 cP at 60 °C) makes working with it difficult, necessitating the addition of reactive diluent (HDDA) to decrease the viscosity. HDDA is particularly susceptible to photo-inhibition with *o*-Cl-HABI while having high reactivity when compared with other diluents tested [18]. Furthermore, polymerization shrinkage—a well known problem in (meth)acrylate photopolymerization [69]—was found to be particularly problematic in highly functionalized diluents (e.g., trimethylolpropane triacrylate (TMPTA)). While monomers typically do not have meaningful absorbance in the visible range, they may have significant UV absorbance, which reduces h_{uv}. The high optical transparency of CN991 and HDDA in the UV and visible region, as seen by the low absorbances in Figure 3.1(d), are therefore desirable in this application.

To determine the reactivity, absorbance height, and intensity dependence of the resin we conducted cured height experiments in which photopolymer resin was irradiated with visible light ($\lambda_{\max} = 458\,\text{nm}$) at various intensities for different times and the gelled height measured. This experiment yields the uninhibited working curve (Figure 3.7(a) and (c)). By fitting Equation 3.15 to experimental data at different intensities, we obtain the parameters for each resin. For Resin 1, $D_c' = 64\,(\text{mW}\,\text{cm}^{-2})^{0.99}\,\text{s}$, $h_b = 408\,\mu\text{m}$, and $m = 0.99$. For Resin 2, $D_c' = 238\,(\text{mW}\,\text{cm}^{-2})^{1.03}\,\text{s}$, $h_b = 1{,}631\,\mu\text{m}$, and $m = 1.03$. Two considerations related to the dual-wavelength printing apparatus are worth noting. First, while it is possible to determine h_b (and h_{uv}) from UV-Vis spectroscopy, the value obtained differs slightly to that from a cured height experiment. The difference is most likely attributed to the broad emission spectrum of LEDs in the dual-wavelength printing apparatus. Second, intensity variation in the system (as with all DLP projection systems) is achieved by pulse width modulation of a digital micromirror device. This is not strictly an "intensity variation," and it is unclear how this affects our results.

To determine the effect of UV light on these resins, we conducted dead zone height experiments under both steady-state and transient conditions (Figure 3.7(b) and (d)). In each case, resin was sandwiched between two glass microscope slides and exposed to concurrent blue and UV irradiation. Subtracting the height of cured resin from the gap between the slides yields the dead zone height. For Resin 1, exposures were over a 30 s period and the dead zone was assumed to be approximated by the steady-state solution (Equation 3.25). A least-squares fit yielded the parameters $\beta = 0.73$ and $h_{uv} = 37.8\,\mu\text{m}$. For Resin 2, exposures were over a 15 s period and the time-dependent model was used (Equation 3.22). A least-squares fit yielded the parameters $\beta = 4.84$ and $h_{uv} = 100\,\mu\text{m}$. The time-dependent model also provides an

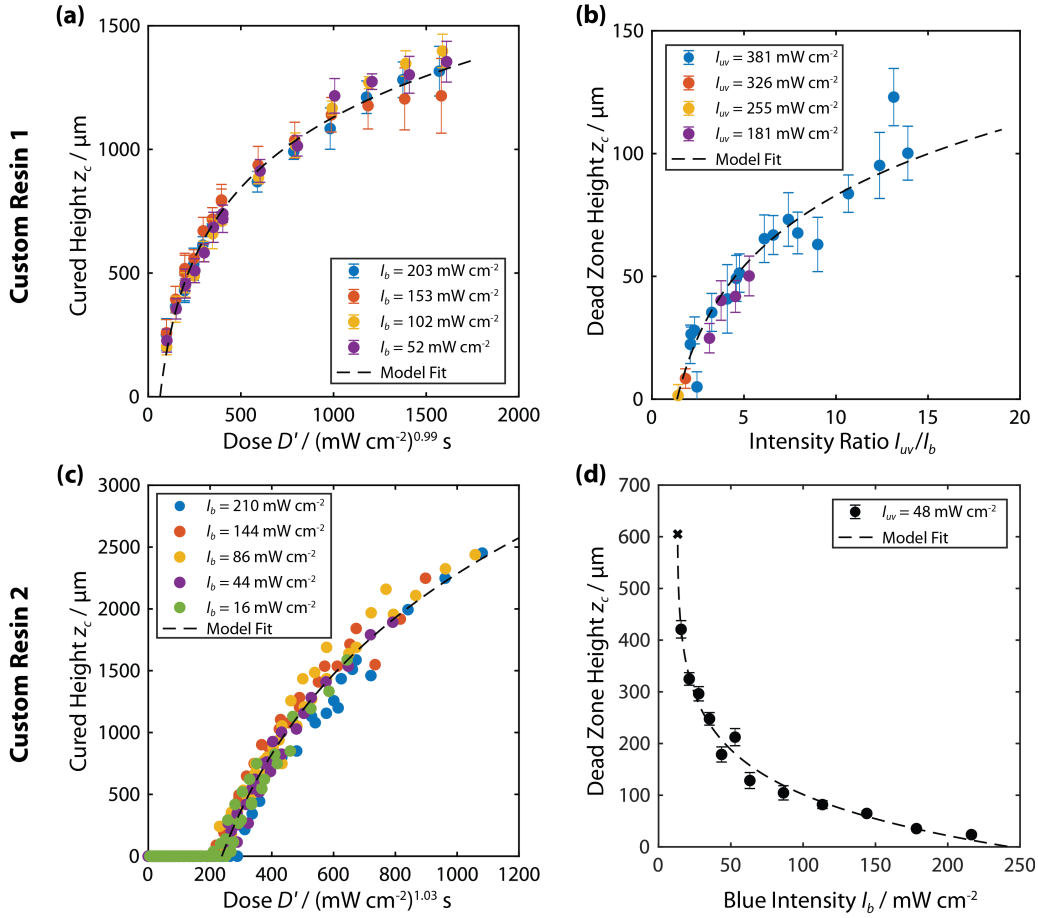

Figure 3.7. Characterization of custom resins for dual-wavelength continuous stereolithography (see Table 3.1 for compositions). **(a)** Cured height as a function of incident dose for Resin 1. A least-squares fit yielded the parameters $D_c' = 64\,(\mathrm{mW\,cm^{-2}})^{0.99}\,\mathrm{s}$, $h_b = 408\,\mu\mathrm{m}$, and $m = 0.99$ ($R^2 = 0.985$). **(b)** Dead zone height as a function of intensity ratio for Resin 1. The exposure time was 30 s, and the data was correspondingly fit to the steady-state dead zone equation, yielding the parameters $\beta = 0.73$ and $h_{uv} = 37.8\,\mu\mathrm{m}$ ($R^2 = 0.902$). **(c)** Cured height for Resin 2, with the parameters $D_c' = 238\,(\mathrm{mW\,cm^{-2}})^{1.03}\,\mathrm{s}$, $h_b = 1{,}631\,\mu\mathrm{m}$, and $m = 1.03$ ($R^2 = 0.958$). **(d)** Dead zone height at 15 s for Resin 2 with time-dependent model fit, with the parameters $\beta = 4.84$, $h_{uv} = 100\,\mu\mathrm{m}$, and $m = 1.29$ ($R^2 = 0.980$).

opportunity to re-fit the termination constant m, which may be reasonably expected to vary from uninhibited to inhibited conditions, as the relative frequency of termination mechanisms may change with the introduction of photoinhibition. For Resin 2 under photoinhibition, $m = 1.29$.

3.5 Conclusion

In conclusion, we have developed a pair of curing models for uninhibited photopolymer resins (in standard projection stereolithography) and photoinhibited resins (in dual-wavelength continuous stereolithography). Compared to the standard Jacobs model, our uninhibited model offers an improved ability to characterize resins for variable-intensity printing—an expanding application—while maintaining the simple characterization method of cured height experiments. Though the resins we tested did not exhibit significant disagreement with the reciprocity assumption, they represent a small subset of resin varieties and future work should more broadly investigate the applicability of the reciprocity assumption in 3D printing resins.

Our photoinhibited curing model allows straightforward characterization of resins for dual-wavelength continuous stereolithography and provides a powerful tool in choosing resin and printing parameters. Resins are characterized using two straightforward experiments (measuring the cured height and the dead zone), and we verified that the model could fit the curing behavior of two custom resins. The ability to easily manipulate the front- and backside curing fronts by varying intensity has significant potential applications in dual-wavelength fabrication of microfluidic devices, as demonstrated in recent work by de Beer [18]. For a well-designed resin, the blue intensity, UV intensity, and exposure time can be chosen to produce layers of overlapping and intersecting channels, significantly reducing the time and equipment needed

to produce microfluidic devices.

CHAPTER IV

Resin Flow and Dead Zone Uniformity in Photoinhibited Continuous Stereolithography

4.1 Introduction

Stereolithography (or vat photopolymerization) is a branch of additive manufacturing with applications including nanomaterials [70], microfluidics [71, 72], biomaterials [73], ceramics [74], and aerospace manufacturing [75]. In stereolithography, liquid photopolymer resin is solidified using light to form sequential cross-sections of a desired part. Many of the technological developments in stereolithography throughout its history have been driven by theoretical, computational, and experimental investigations of the physical interactions among the moving build platform, the growing gelled part, flowing liquid resin, and the resin bath. The significant forces required to separate the part from the resin bath in layer-by-layer stereolithography drove the development of new separation methods and surface treatments [8, 9, 10, 11]. A paradigm shift came in 2015 with the introduction of continuous liquid interface production (CLIP) [12]. By introducing a *dead zone* (a region in which polymerization does not occur) between the growing part and the resin bath, CLIP further reduced separation forces and enabled continuous printing; however, separation forces within CLIP still impose limits related to print speed, part size, and resin viscosity [50, 76, 56]. More recent continuous printing approaches in stereolithography have

continued address the limitations imposed by separation forces [15, 16, 17].

In one of these new continuous printing approaches, dual-wavelength continuous stereolithography [15], resin is formulated with orthogonal photochemistries for initiation and inhibition—that is, initiation and inhibition are driven by independent wavelengths of light. By varying the intensities of projected light as well as the concentrations of photoinitiator, photoinhibitor, and light absorbers, a dead zone of controllable thickness is generated. By printing with thick dead zones, existing limitations resulting from limited resin reflow rates and large separation forces under the build platform were addressed. As a result, this method offered the highest reported linear print speeds of any continuous 3D printing method when published. However, while dead zone control provides a powerful avenue to increase production rates and has been clearly demonstrated in stationary resin characterization experiments (see Refs. [15] and [18] as well as Chapter III of this work), the exact nature of the dead zone during continuous printing—driven by the complex interplay of resin flow and competing photoinitiation and photoinhibition reactions—has yet to be elucidated.

Here, we develop and analyze computational fluid dynamics (CFD) models to investigate how resin flow affects the development of the dead zone and the printability and fidelity of parts in dual-wavelength continuous stereolithography. We report flow profiles in the resin bath and find that, in our model, dead zone uniformity and part fidelity are significantly affected by light intensities, moderately affected by print speed, and slightly affected by part radius. We hypothesize that dead zone uniformity is a contributor to the printability and quality of parts and that good printing conditions result in a uniform dead zone. To that end, we develop a model to maximize dead zone uniformity by spatially varying light intensities and verify the effectiveness of this approach by printing actual parts.

4.2 Model Description

4.2.1 Model Geometry and Material Properties

Figure 4.1(a) shows the printing set-up for dual-wavelength continuous stereolithography. A bath with a rigid, transparent window in the bottom is filled with photopolymer resin. A build head is initially positioned adjacent to the window, then moves upward continuously as cross-sections of the desired part are sequentially projected through the window and cured onto the growing part. Resin is prevented from curing onto the window through the generation of a *dead zone* near the window in which polymerization is inhibited. Initiation and inhibition of polymerization are achieved using orthogonal photochemistries. In the approach used by de Beer [15], which forms the basis of this model, resins are formulated with photoinitiators activated by blue light and photoinhibitors activated by UV light. By judiciously choosing the light intensities and the concentrations of resin components (including blue and UV light absorbers), the thickness of the dead zone can be controlled (as demonstrated in Ref. [15] and in Chapter III of this work).

Finite element models of the dual-wavelength stereolithography system were constructed in COMSOL Multiphysics 5.5 (COMSOL, Inc.). While the intensities were varied in simulations, the resin properties were maintained constant and are shown in Table 4.1. Results from two models, with geometries shown in Figure 4.1(b) and (c) and dimensions in Table 4.2, are presented here. In each case, the yellow region labelled "photopolymer resin" is the only domain directly included in the model. Other non-flowing regions are excluded and their role in the model is effected via boundary conditions.

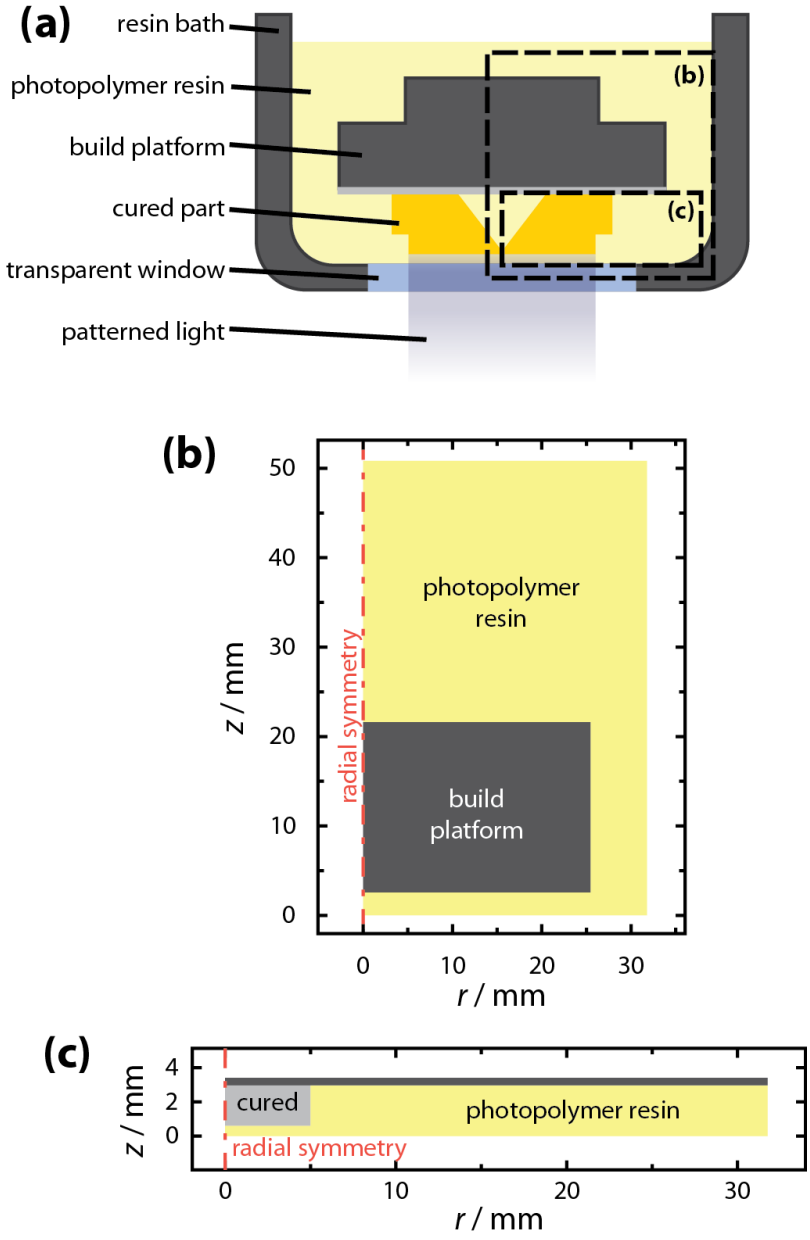

Figure 4.1. **(a)** Diagram of dual-wavelength continuous stereolithography. A resin bath filled with photopolymer resin is simultaneously exposed to blue and UV light, which respectively initiate and inhibit polymerization. The build platform ascends as cross-sections of the part are continuously exposed and cured. Dashed lines indicate the regions of the resin bath that are included in each COMSOL geometry. **(b)** Geometry for the time-dependent, axisymmetric model. **(c)** Geometry for the steady-state, axisymmetric model, which is used for intensity optimization.

Table 4.1. Resin material properties in the COMSOL models. Resin 1 is used for results in the time-dependent model, and Resin 2 is used with the optimization model. Note that the critical dose and inhibition constant are given in their volumetric forms.

Property	Symbol	Resin 1	Resin 2	Unit
density	ρ	1.05×10^3	1.05×10^3	$\mathrm{kg\,m^{-3}}$
dynamic viscosity	μ	0.3	0.3	$\mathrm{Pa\,s}$
diffusion coefficient	c	1.0×10^{-10}	1.0×10^{-10}	$\mathrm{m^2\,s^{-1}}$
critical dose	D_c	1.5×10^3	1.6×10^3	$\mathrm{mJ\,cm^{-3}}$
blue absorbance height	h_b	600	408	µm
UV absorbance height	h_{uv}	50	38	µm
inhibition constant	β	7.58×10^{-2}	7.45×10^{-2}	–
termination constant	m	1	1	–

Table 4.2. COMSOL model dimensions.

Dimension	Time-Dependent Model	Steady-State Model	Unit
resin bath			
radius	32	–	mm
height	51	–	mm
build platform			
radius	25	25	mm
height	19	–	mm
initial gap	25	3,000	µm

Time-Dependent Model This radially symmetric model, shown in Figure 4.1(b), drives flow in the resin bath by including a moving build platform. In the model geometry, the resin bath is 32 mm by 76 mm. The build platform is represented by a 25 mm-by-19 mm void in the geometry that begins 25 µm above the window and ascends at the print speed using a moving mesh interface. As fluid elements reach the critical dose, their velocity is forced to match that of the build platform, resulting in the cohesive movement of the cured part (discussed in greater detail below). Since interfacial effects as the cured part exits the liquid resin into air are not in the scope of this model, the upper boundary is treated as open—allowing flow in or out—to represent an infinitely deep resin bath.

Steady-State Model This radially symmetric model, shown in Figure 4.1(c), is used for intensity optimization and includes only the area under the build platform. Since the model is steady-state, movement of the build platform and growth of the cured part are not included; the build platform is positioned 3 mm above the window, where it is expected that flow underneath the part is affected primarily by the size of the dead zone rather than movement of the build platform. The cured part is represented by a void in the geometry. Resin flows in at the edge of the build platform (with the z-dependent flow direction approximated from the time-dependent model); the build platform and the bottom of the part are outlets, with resin velocity equal to the print speed.

4.2.2 Resin Curing

Resin curing was modeled using a previously derived dose-based model (see Chapter III):

$$\frac{\partial D'}{\partial t} = \left(I_{b,0}e^{-z/h_b} - \beta I_{uv,0}e^{-z/h_{uv}}\right)^m \tag{4.1}$$

where D' is the dose equivalent, t is time, $I_{b,0}$ is the incident blue intensity, h_b is the blue absorbance height, β is the inhibition efficiency, $I_{uv,0}$ is the incident UV intensity, h_{uv} is the UV absorbance height, and m is the termination constant. To combine this model with resin flow, the dose was treated as a conserved quantity described by the convection-diffusion equation, with the right-hand side of Equation 4.1 as a source term:

$$\frac{\partial D'}{\partial t} - \vec{\nabla} \cdot (c\vec{\nabla} D') + \vec{u} \cdot \vec{\nabla} D' = \left(I_{b,0} h_b^{-1} e^{-z/h_b} - \beta I_{uv,0} h_{uv}^{-1} e^{-z/h_{uv}} \right)^m \tag{4.2}$$

where c is the diffusion coefficient for dose, which must be nonzero due to the computational difficulty of convection-dominated problems [77], and $\vec{u}$ is the velocity vector. The dose at all points has an initial value of zero and the diffusive flux goes to zero at all boundaries. The incident intensities vary with position and are zero for $r > R_p$, where R_p is the part radius.

The phase transition from liquid to gelled resin is tracked using the Heaviside step function $H(x)$ and the critical dose D'_c:

$$\alpha = H\left(\frac{D'_c - D'}{D'_c} \right) \tag{4.3}$$

As the dose in a fluid element approaches the critical dose, the phase variable α of that element decreases from one (liquid) to zero (gelled).

4.2.3 Resin Flow

Resin flow is modeled using the Navier-Stokes equation assuming laminar flow. With maximum velocities on the order of $10^{-2}\,\mathrm{m\,s^{-1}}$, lengths on the order of $10^{-2}\,\mathrm{m}$, and a kinematic viscosity of approximately $10^{-4}\,\mathrm{m^2\,s^{-1}}$, the maximum possible Reynolds number is $\mathrm{Re} \sim 1$. Since the highest velocities correspond to the smallest length scales (at the beginning of printing when the build platform is near the

window), the Reynolds number is expected to be smaller. Thus, the laminar flow assumption is reasonable for this model.

Since cured resin should cohere and move together as a solid object, an arbitrarily large volume force is introduced in the model to drive the gelled resin velocity to the speed of the build platform, to which the growing part is attached.

$$F_r = -u\left[\frac{A(1-\alpha)^2}{\alpha^3+\epsilon}\right] \tag{4.4}$$

$$F_z = -(w-S)\left[\frac{A(1-\alpha)^2}{\alpha^3+\epsilon}\right] \tag{4.5}$$

where F_r and F_z are the r- and z-components of the force, u and w are the r- and z-components of the velocity vector, S is the vertical print speed, A is an arbitrarily chosen constant to dictate the magnitude of the force, α is the previously defined phase variable, and ϵ is an arbitrarily small constant to avoid division by zero. When $\alpha = 1$ (in the liquid resin), $\vec{F} = 0$. However, as $\alpha \to 0$ the force ramps up and is proportional to the difference between the current resin velocity and the desired resin velocity ($u = 0$ and $w = S$). To achieve cohesive motion of the gelled part, we use the constants $A = 10^8\,\mathrm{N\,s\,m^{-4}}$ and $\epsilon = 10^{-3}$.

4.3 Results and Discussion

4.3.1 Time-Dependent Print Modelling

The time-dependent axisymmetric model was used to simulate the printing of cylinders of various diameters and to explore the effects of print speed and blue light intensity on the dead zone during printing. Figure 4.2 shows representative velocity profiles during continuous printing. Resin flow is driven by vertical movement of the build platform. While printing, resin is displaced from above the build platform and drawn underneath to fill the expanding gap between the build platform and the window. A volumetric flow rate of $A_{BP}S$ is required during printing, where A_{BP} is

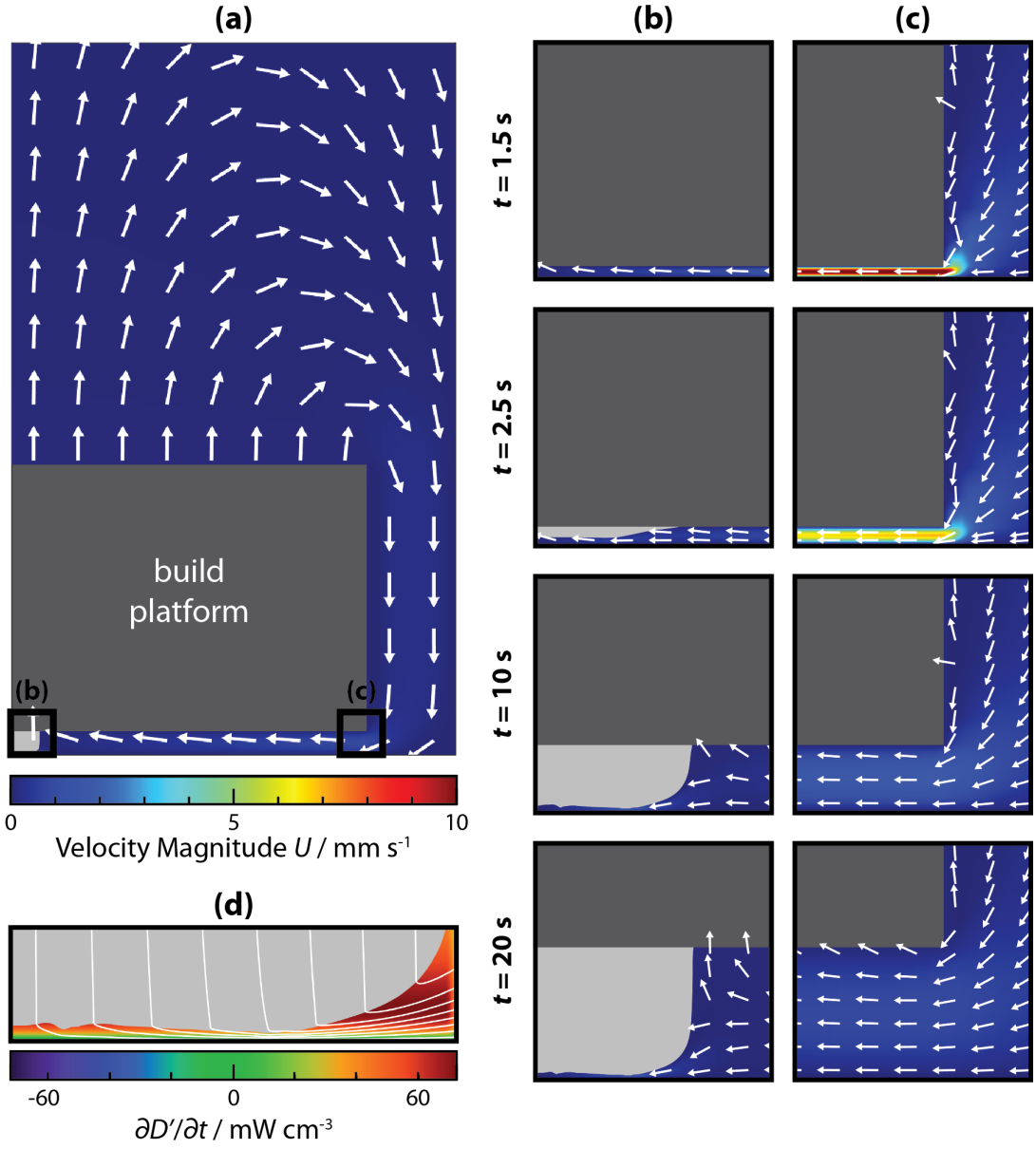

Figure 4.2. Representative flow profile for printing of a 2 mm radius cylinder at 300 mm h^{-1}. **(a)** View of resin flow throughout the resin bath at $t = 20$ s. The regions corresponding to insets (b) and (c) are indicated. Arrows indicate the direction of flow while color indicates the velocity magnitude. **(b)** Resin flow near the growing part at $t = 1.5$ s, 2.5 s, 10 s, and 20 s. Light gray under the build platform represents the growing gelled part. **(c)** Resin flow near the edge of the build platform. Times correspond to those for (b). **(d)** Streamlines and $\partial D'/\partial t$ under the growing part.

the surface area of the build platform and S is the print speed. Since this flow rate is constant through the printing process, flow velocities are highest in the initial stages of printing when the gap between the build platform and window are small (Figure 4.2(c)). It is also at this point that deforming forces are the highest. The force resulting from movement of the build platform is that of a viscous Newtonian fluid between two separating parallel plates, known as the Stefan adhesion force. This force can be derived from the lubrication approximation and is given by

$$F_{\text{Stefan}} = \frac{-3\pi\mu S R^4}{2h^3} \tag{4.6}$$

where μ is the resin dynamic viscosity, R is the plate radius, and h is the separation distance. At early print times, the force is dominated by the effect of the build platform, while at later times, the force is relevant primarily in the gap between the cured part and the window.

Flow patterns near the center of the build platform are shown in Figure 4.2(b). Resin starts with $D' = 0$. The cured part is initiated and grows as resin reaches the critical dose. Because the blue and UV intensities—and consequently, $\partial D'/\partial t$—vary with depth into the resin, it is clear that resin flowing to different regions of the cured part will experience vastly different exposure histories. Figure 4.2(d) shows streamlines under the part with $\partial D'/\partial t$. Resin traveling to the center of the part flows closer to the window (where inhibition is higher) and spends more time in the exposure region than resin traveling to the outer edge of the part. As noted above, as the gap between the build platform and the window expands, forces in the gap between the cured part and the window (i.e., the dead zone) become more significant. For a build platform radius of 25 mm, a part radius of 5 mm, and a dead zone height of 100 µm, this changeover occurs when the gap between the build platform and the window is 855 µm (see Appendix C.2).

To investigate the effect of printing parameters on dead zone uniformity, we ran simulations while varying blue intensity, part radius, and print speed, with results shown in Figure 4.3. In these plots, the curing front is defined by the $D' = D'_c$ contour; the procedure for calculating the dead zone height is described in Appendix C.3. Parameters other than the variable of interest are held constant at $I_b = 100\,\mathrm{mW\,cm^{-2}}$, $I_{uv} = 130\,\mathrm{mW\,cm^{-2}}$, $S = 300\,\mathrm{mm\,h^{-1}}$, and $R_p = 1\,\mathrm{mm}$, and simulations were run for 40 s based on results showing that the dead zone profile does not change significantly from 40 s to 60 s. As shown in Figure 4.3(a–b), changes in the blue intensity significantly affect the dead zone uniformity. At $I_b = 100\,\mathrm{mW\,cm^{-2}}$, the dead zone is reasonably uniform; however, as the intensity is moderately reduced, the average dead zone thickness increases due to significant nonuniformity. At $I_b = 70\,\mathrm{mW\,cm^{-2}}$, the dead zone height at the center of the part (399 µm) is nearly five times the minimum value near $r = 0.5\,\mathrm{mm}$ (83 µm). As the blue intensity increases above $110\,\mathrm{mW\,cm^{-2}}$, the part adheres to the window (the model is halted if D' on the bottom boundary exceeds the critical dose). These results suggest that, contrary to predictions from the stationary exposure model (Chapter III), uniform dead zones of arbitrary thickness cannot be generated in continuous printing simply by adjusting the UV/blue intensity ratio. Outside of a small range of intensities, two outcomes are seen: significant nonuniformity in the dead zone height or adhesion to the window.

In Figure 4.3(c–d), the print speed is also seen to affect the curing front, albeit not as dramatically as the blue intensity: a 30% change in the blue intensity more significantly affects the dead zone height than scaling the print speed by a factor of six (from $75\,\mathrm{mm\,h^{-1}}$ to $450\,\mathrm{mm\,h^{-1}}$). However, while the curvature at the edge of the part was fairly constant as the blue intensity changed, the part edge is notably sharper at low speeds than it is at high speeds.

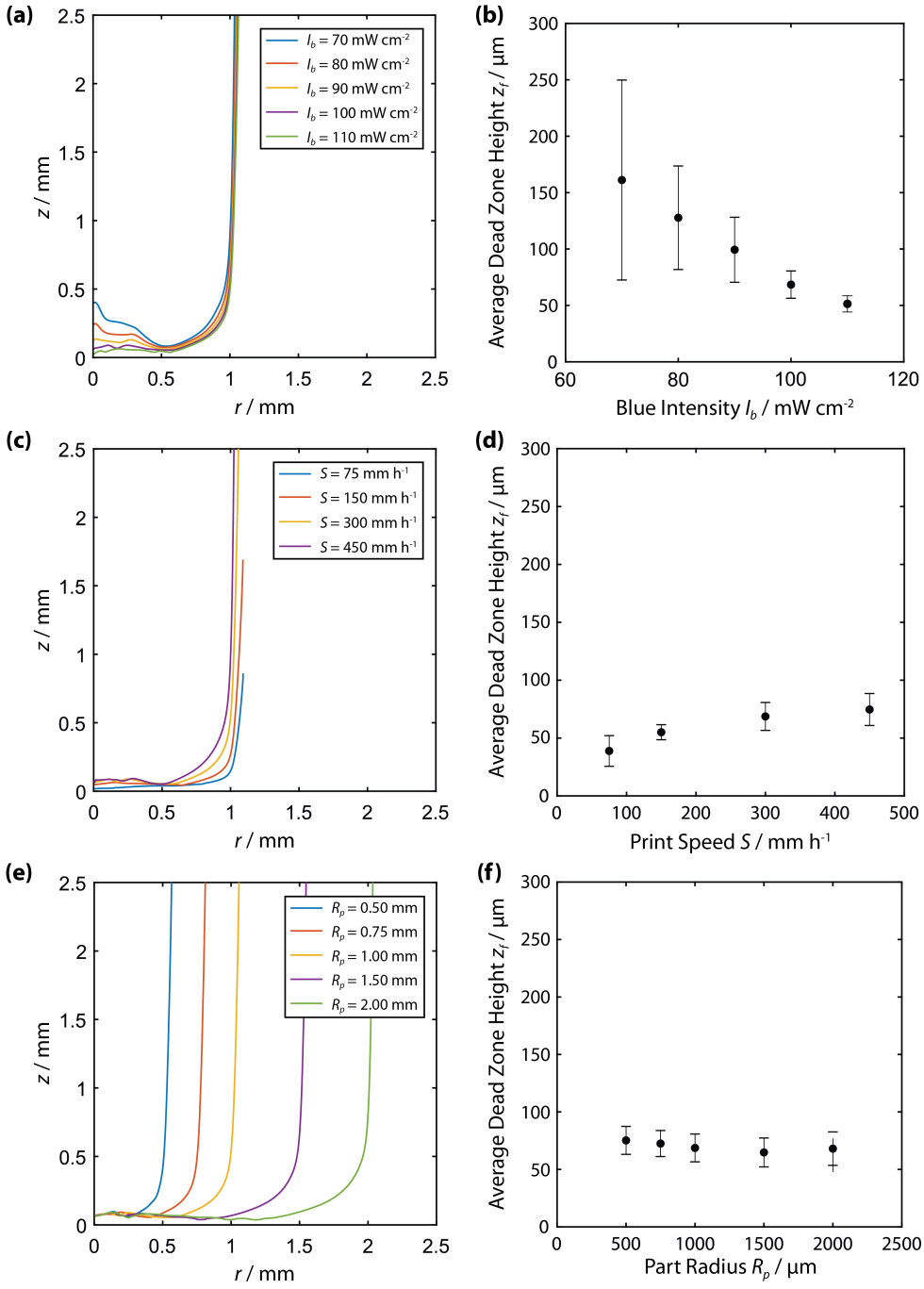

Figure 4.3. The overall shape and uniformity of the curing front is affected by blue intensity, print speed, and part radius. Parameters other than the variable of interest are held constant at $I_b = 100\,\mathrm{mW\,cm^{-2}}$, $I_{uv} = 130\,\mathrm{mW\,cm^{-2}}$, $S = 300\,\mathrm{mm\,h^{-1}}$, and $R_p = 1\,\mathrm{mm}$. The curing front is identified as the $D' = D'_c$ contour. Error bars in dead zone height plots indicate dead zone uniformity and are calculated as the standard deviation of z-coordinate values for points in the dead zone curing front (see Appendix C.3). **(a–b)** Curing front and average dead zone height for blue intensities ranging from $70\,\mathrm{mW\,cm^{-2}}$ to $110\,\mathrm{mW\,cm^{-2}}$. **(c–d)** Curing front and average dead zone height for print speeds ranging from $75\,\mathrm{mm\,h^{-1}}$ to $450\,\mathrm{mm\,h^{-1}}$. **(e–f)** Curing front and average dead zone height for part radii ranging from 0.5 mm to 2 mm.

As the part radius increases (Figure 4.3(e) and (f)), the dead zone height in the center remains nearly constant, though it pushes downward some some near the edge. While increases in the blue intensity for larger parts might improve uniformity by reducing the dead zone height in the center, this will result in an overall thinner dead zone than in smaller parts, exacerbating the effect of increased separation forces, which scale with R_p^4 / z_f^3.

4.3.2 Intensity Optimization

We also developed a simplified steady-state model to programmatically optimize blue and UV exposure intensities for a given part radius and print speed (geometry shown in Figure 4.1(c)). While flow in the time-dependent model is directly driven by build platform movement, the steady-state model simulates only the area under the build platform, with an inlet defined at the outer edge and outlets on the build platform and cured part (henceforth the "part outlet"). To accurately represent flow in this simplified model, the velocity profile at the edge of the build platform (while 3 mm from the window) was extracted from the time-dependent model and used to set the flow direction as a function of z at the inlet of the steady-state model. At the outlets, resin was constrained to flow in the z-direction at the print speed (i.e., $u = 0$ and $w = S$).

Exposure occurs in the region from $r = 0$ to $r = R_p$, and three restrictions on intensity were considered: constant blue and UV intensities, varying blue and constant UV intensities, and varying both blue and UV intensities. The first case corresponds to exposure using unpatterned light sources and a physical mask. The second case corresponds to exposure from a patterned blue light source and unpatterned UV light source. This case applies to our current dual-wavelength continuous printing apparatus, in which blue light is provided by a DLP projector (which can be patterned using

grayscale images) and UV light is provided by an unpatterned LED source [15]. The third case corresponds to exposure from patterned blue and UV sources. Practically this could be achieved using a single projector containing both blue and UV LEDs or by superimposing images from independent blue and UV projectors. When constant, the intensity was allowed to take on any single intensity within the practical range of our light sources (0 to 200 mW cm^{-2} for blue and 0 to 275 mW cm^{-2} for UV). When varying, the coefficients of a fifth-order Bernstein polynomial were optimized and the intensity was capped at the previously noted limits.

$$\begin{aligned} I_0(r) = I_{\max}[&b_0(1-\bar{r})^5 + b_1\bar{r}(1-\bar{r})^4 + b_2\bar{r}^2(1-\bar{r})^3 \\ &+ b_3\bar{r}^3(1-\bar{r})^2 + b_4\bar{r}^4(1-\bar{r}) + b_5\bar{r}^5] \end{aligned} \tag{4.7}$$

where $I_{\max}$ is the maximum allowable intensity (200 mW cm^{-2} for blue and 275 mW cm^{-2} for UV), b_n are the Bernstein coefficients subject to optimization, and $\bar{r} \equiv r/R_p$.

Additionally, the gap height under the part outlet (the dead zone height) is included as an optimized parameter. While this dimension can be set explicitly to optimize the intensities for a uniform dead zone of the desired height, here we focused on achieving the most uniform dead zone possible (regardless of height). The dead zone height was allowed to vary from 10 µm to 300 µm.

Two objective functions are used: one at the part outlet to optimize for dead zone uniformity and a second at the window to restrict the solution from attaching the growing part to the window. These functions are:

$$\int_{\substack{\text{part}\\\text{outlet}}} (D' - D'_c)^2 \mathrm{d}r \tag{4.8}$$

$$\int_{\text{window}} (1-\alpha) C_0 \mathrm{d}r \tag{4.9}$$

The first objective function penalizes solutions if outflowing resin is not at exactly the critical dose. In areas where the exiting resin is above the critical dose, the actual dead zone height is expected to be below the part outlet height; where the exiting resin is below the critical dose, the dead zone will be higher. In the second objective function, C_0 is an arbitrary large constant to penalize (and ideally exclude) solutions where the phase variable at the window surface is zero, indicating cured resin.

Figure 4.4 shows optimization results for the three sets of intensity restrictions. Comparing the three cases, it clear that the ability to spatially vary intensity enables significantly more uniform dead zones. Variable blue intensity with constant UV improves on the constant blue and UV case, and variable blue and UV achieves the most uniform dead zones. Interestingly, when both intensities are unpatterned (Figure 4.4(a)), the optimized values are effectively constant across the range of part radii considered. This result adds some support to our conclusions from the time-dependent model (Figure 4.3): the part radius does not significantly affect the form of the dead zone. It is also noteworthy that the UV intensity takes its maximum allowable value, ensuring that the part does not adhere to the window. For the most lax intensity restriction—when blue and UV are both allowed to vary spatially—the solution for each part radius again appears similar, with the curves essentially overlapping (Figure 4.4(c)). Although the similar curve shapes suggest that the UV/blue intensity ratio I_{uv}/I_b might remain constant throughout the part, it in fact varies considerably (see Appendix C.5); furthermore, the peak intensity ratio ranges from approximately 2.8 for $R_p = 10\,\text{mm}$ to 4.9 for $R_p = 6\,\text{mm}$. The latter effect may be an artifact of imperfect optimization since there is no clear pattern in the intensity ratio function as part radius increases and the differences among the intensity curves are quite small. However, the former effect persists across part radii,

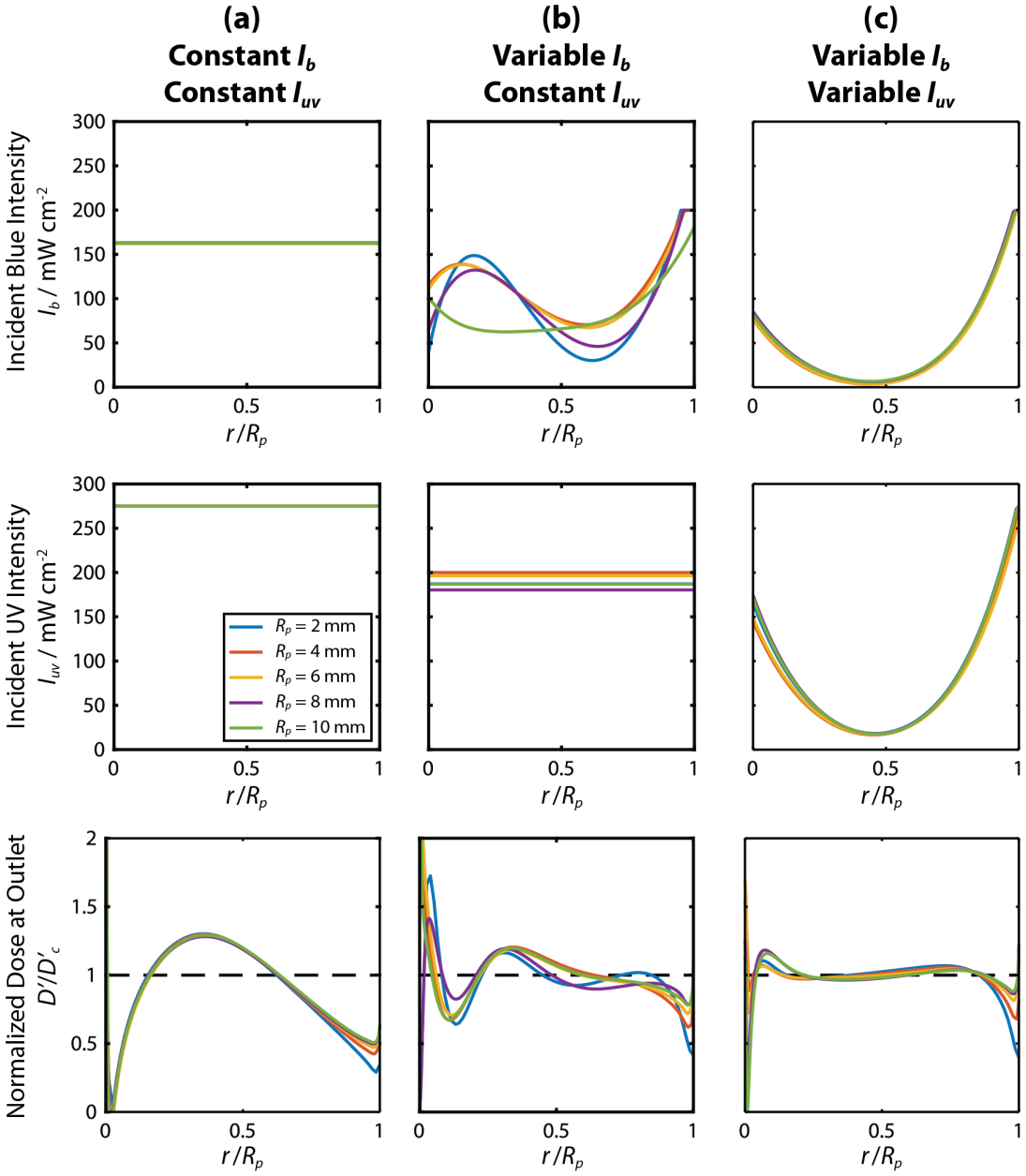

Figure 4.4. Exposure optimization under different intensity restrictions for cylinders with radii ranging from $R_p = 2\,\text{mm}$ to $10\,\text{mm}$. The first row of plots shows the incident blue intensity as a function of the r-coordinate normalized to the part radius. The blue intensity is capped at $200\,\text{mW cm}^{-2}$. The second row shows the incident UV intensity, which is capped at $275\,\text{mW cm}^{-2}$. The third row shows the dose at the part outlet normalized to the critical dose. **(a)** Blue and UV intensities are restricted to constant values across the part radius. The optimized value for each part radius is approximately equal. **(b)** Blue intensity is allowed to vary as a function of r, while UV is constant. **(c)** Both blue and UV intensities are allowed to vary as functions of r.

with each intensity ratio curve having a similar form.

To verify functionality of the optimization model, we attempted to print cylinders (10 mm radius, 30 mm height) using the optimized intensities predicted by the model, with results shown in Figure 4.5. Since our current exposure setup is not capable of UV patterning, only the constant blue/constant UV and variable blue/constant UV solutions were considered. A description of the materials and methods for dual-wavelength continuous 3D printing is available in Appendix C.1. For each of the two solutions, we attempted printing at 100%, 90%, and 80% of the optimized blue intensity value; the inset in the corner of each plot shows the grayscale image corresponding to each intensity function at 100%. The optimized UV intensity value was not adjusted and was $275\,\mathrm{mW\,cm^{-2}}$ when the blue intensity was constant and $187\,\mathrm{mW\,cm^{-2}}$ when the blue intensity was allowed to vary. In testing the constant blue intensity function (Figure 4.5(a)), we found that the computationally optimized value was too high for successful printing: at both 100% ($I_b = 164\,\mathrm{mW\,cm^{-2}}$) and 90% ($I_b = 146\,\mathrm{mW\,cm^{-2}}$), the part attached to the window during early stages of printing, causing the print to fail. At 80% ($I_b = 130\,\mathrm{mW\,cm^{-2}}$), we were able to print the 30 mm tall cylinder, though it contained an observable void in the center. Such voids can result from insufficient resin reflow rates, which occur when the gap between the part and the window is too small, or from uptake of highly inhibited resin, which can occur if the blue and UV intensities are not properly balanced in a region of the part. As the results of our time-dependent model showed, for large-radius parts at constant blue and UV intensity, the dead zone tends to be smaller near the outer edge than at the center (Figure 4.3(e)). The effects of this nonuniformity are seen here: it is difficult to produce a part which prints successfully (i.e., does not cure to the window) but that is solid in the center.

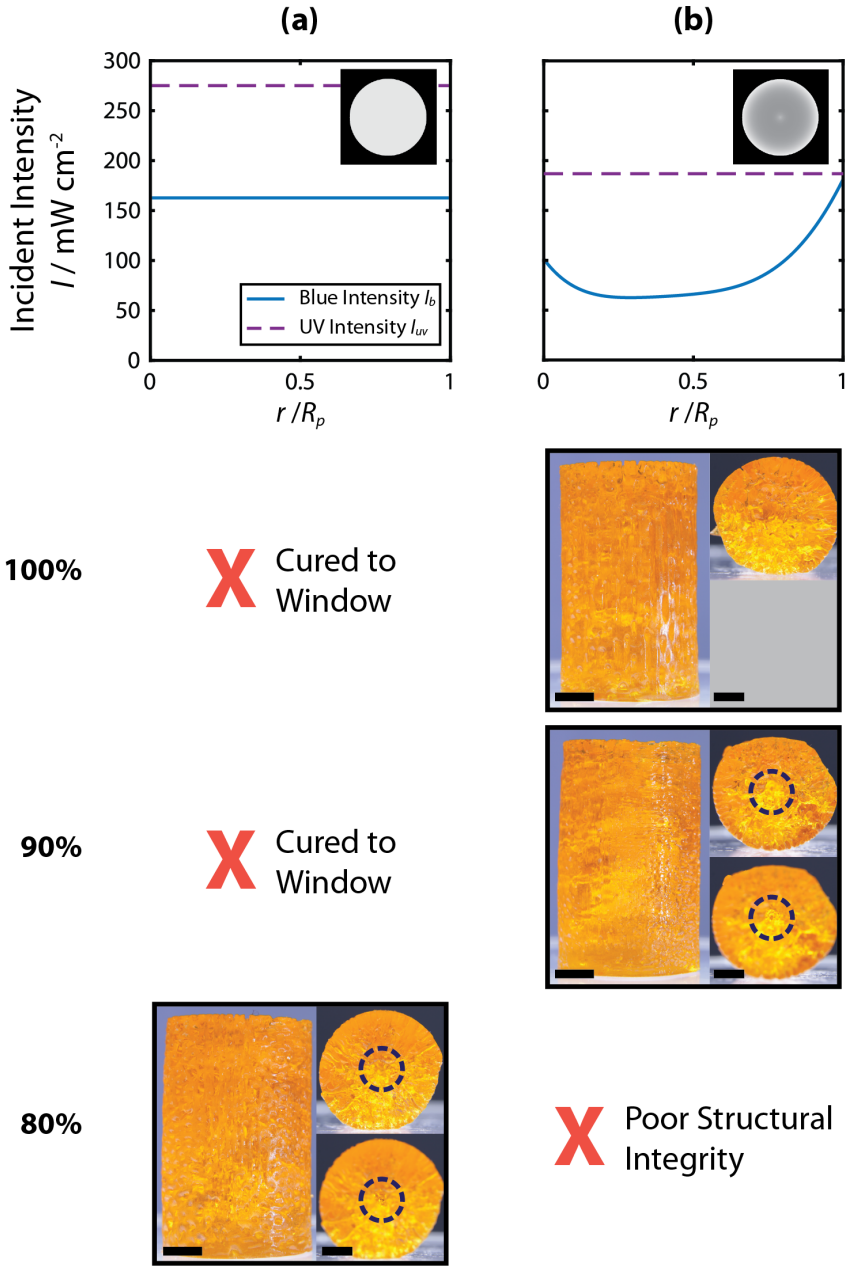

Figure 4.5. Experimental verification of optimized exposure parameters for a 10 mm radius cylinder. Plots show the incident blue and UV intensity as functions of the normalized r-coordinate. Insets show the images generated from the intensity functions. Blue intensities were scaled to 100%, 90%, and 80% of their optimized values for print tests. Photos of the top cylinder surface are taken in different focal planes to show the presence (indicated by a dashed circle) or absence of an interior void. Scale bars are 5 mm. **(a)** Unpatterned blue and UV. Printing attempts using 100% and 90% of the optimized blue intensity were unsuccessful as parts consistently cured to the window. Printing at 80% of the optimized blue intensity was successful, though the resulting part had a large void in the center of the cylinder. **(b)** Patterned blue and unpatterned UV. Printing was successful at 100% and 90% of the blue intensity function, while the 80% part was weakly cured.

When allowing the blue intensity to spatially vary, we found that the part could be successfully printed without significant internal voids using the unmodified optimized intensity function ($I_{b,\max} = 181\,\mathrm{mW\,cm^{-2}}$). At 90% ($I_{b,\max} = 163\,\mathrm{mW\,cm^{-2}}$), the part printed successfully but again contained a noticeable internal void.

One challenge in using the prototype dual-wavelength printer and a variety of custom photoinhibitable resin formulations is the inability to know *a priori* the appropriate printing parameters (i.e., speed, blue intensity, UV intensity) for a given part, resulting in a sometimes lengthy trial and error process. This optimization approach is able to alleviate some of that challenge by identifying effective settings without requiring any printing.

4.4 Conclusion

In summary, we have developed a pair of CFD models for simulating the dual-wavelength continuous stereolithography printing process and optimizing blue and UV light intensities to maximize dead zone uniformity. Our results suggest that dead zone thickness may not be easily controllable for a fixed resin, part, and print speed. Our intensity optimization model was reasonably successful in predicting effective printing conditions for a 20 mm diameter test model: when intensities were restricted to only constant values, the optimized blue intensity needed to be reduced by 20%, and when the blue intensity was allowed to vary spatially, the optimized function could be used without modification.

Many physically relevant factors, such as part deformability and interfacial effects at the resin surface, were not considered here, and the model could be expanded to consider these. Furthermore, many potential routes for print optimization are suggested by our findings but remain unexplored. Future efforts might further in-

vestigate the ability to control dead zone thickness by varying UV intensity and considering the role of light absorbers in the resin. Experimentally, the efficacy of applying intensity functions from cylindrical parts to individual features in more complex parts could be considered. Additionally, variable intensity could be applied to both blue and UV with a suitable light source. Ultimately, this study lays the groundwork for future computational investigations and optimizations of dual-wavelength continuous stereolithography, which will continue to drive the technology forward.

CHAPTER V

Conclusions and Continuing Work

5.1 Conclusions

Dual-wavelength printing technology—including future multi-wavelength methods using additional independent photochemistries—is well-positioned to increase production rates in stereolithography and produce parts that are difficult to create via other methods. However, progress in dual-wavelength printing will be slow without deeper understanding of the complex web of physical phenomena that drive and limit the process. In this dissertation, I have attempted to address some of these challenges. To that end, I have presented three modeling approaches to improve dual-wavelength continuous stereolithography, with a focus on using spatially variable exposures to improve part fidelity and unlock new applications.

In Chapter II, we identified the use of highly absorbing resins as a limit on print speed and developed a method to improve print fidelity for less-absorbing resins. We developed a mathematical model for optical dose to calculate the total accumulated dose as a function of position in continuous printing and used that model to "correct" slices projected during the printing process. Slice images for a model are analyzed and modified using grayscale to precisely set the dose profile in the final printed part, and we outlined an approach to designing dose profiles. We validated

slice correction using a dual-wavelength continuous printer and achieved a nearly 90% reduction in cure-through for the test parts considered. Our results suggest that typical slicing methods—which are optimized for traditional stereolithography and highly-absorbing resins—are insufficient to realize the highest possible speeds in continuous stereolithography.

Our model and correction algorithm for cure-through nearly eliminated cure-through artifacts in test parts on the dual-wavelength printer, but this approach also has potential to reduce cure-through and facilitate higher print speeds in other continuous printing methods (e.g., CLIP [12]) or in layer-by-layer methods, which to our knowledge do not generally implement any form of cure-through correction. When implementing cure-through correction in other printers, consideration must be given to the resin depth in the bath. The model assumes an infinitely deep resin bath, and our experiments used larger-than-usual resin volumes to accommodate this assumption; however, bottom-up (surface-constrained) projection stereolithography typically uses small resin volumes to reduce material waste. The use of the existing model with shallow resin baths could result in undercuring of features, and increasing D_c or adjusting the model to account for resin depth could result in unavoidable cure-through. In general, correction performance will suffer if the resin depth is too small relative to the resin absorbance height. Thus, resin depth, absorbance height, and correction parameters must all be considered together to optimize part fidelity, print speed, and material waste.

Our cure-through work did not consider the role of inhibition—despite its necessity for continuous printing—or the potential invalidity of the reciprocity assumption for stereolithography resins. Thus, we sought to develop a more descriptive curing model for the dual-wavelength system. In Chapter III, we derived and verified kinetics-based

curing models for both uninhibited and photoinhibited stereolithography. Both models maintain the simple characterization method of the predominant curing model while offering an improved ability to characterize resins for variable-intensity printing, and the photoinhibited model is a necessary step in the development of more complex simulations of dual-wavelength continuous stereolithography. The photoinhibition model we developed allows prediction of both front- and backside curing fronts as a function of time, incident intensities, and resin properties. This model has been successfully applied in dual-wavelength fabrication of microfluidic devices and has the potential to reduce financial and technical barriers in the field of microfluidics.

While the kinetics-based curing models are useful in their own right, revisiting our cure-through work to incorporate these models could improve the utility of slice correction. Firstly, the photoinhibited curing model might reduce or eliminate the need for parameter tuning for our dual-wavelength printer. Parameter tuning experiments allow for effective correction despite the fact that the curing model does not account for resin flow or UV inhibition; however, these experiments are time-consuming and it is inconvenient to perform them in addition to the standard resin characterization experiments. Secondly, combining the uninhibited model with slice correction could be highly impactful in the burgeoning literature on dose-dependent functionality in stereolithography by enabling precise delivery of prescribed dose profiles, with corresponding variations in material properties.

In our own dual-wavelength system, resin characterization and application of the model are limited by the installed light sources. Blue light is supplied by a modified DLP projector, and the light intensity is observed to decrease over the course of a continuous exposure. UV light is supplied by a constant LED source, and the

light intensity is observed to vary radially. These inconsistencies increase variability between experiments, thus requiring large numbers of trials to reduce error; a suitable light source will alleviate these challenges.

Adding another layer of complexity onto our previous curing models, in Chapter IV we developed computational fluid dynamics simulations to investigate interactions between resin flow and exposure parameters during continuous printing. These results complicate our understanding of dead zone control in dual-wavelength continuous stereolithography and suggest that attempts to adjust the dead zone thickness can adversely affect dead zone uniformity. We developed a model to optimize exposure patterns, and our printing experiments confirm the predictive ability of the model. Our results support the hypothesis that dead zone uniformity in the computational model is connected to the ability to print successfully and suggest several future routes to optimize the performance of dual-wavelength continuous stereolithography.

Though the model is specific to the dual-wavelength system, our core findings—that exposure history and dead zone height vary throughout cured features and that this nonuniformity can be reduced using optimized exposure patterns—are important beyond our printing technology. While exposure in layer-by-layer stereolithography occurs only in stationary resin, all continuous stereolithography technologies expose resin as it is drawn across the window by the continuously ascending cured part and can benefit from exposure optimization. "Full print" simulation is likely to be impractical outside of high-production-volume parts (due to long computation times); however, optimized intensity functions for cylinders and other simple geometries may be applicable to individual features in more complex parts.

The overall goal of this work was to better understand the physical phenomena

underlying dual-wavelength continuous stereolithography and to harness that understanding to improve printer performance and enable new applications. We have successfully used spatially variable exposure optimization to improve print speed, part fidelity, and dead zone uniformity and to enable concept-to-device fabrication of complex microfluidic devices in a matter of hours rather than days. Though we focused on the dual-wavelength system, our work also impacts the field of stereolithography more broadly. We developed a kinetics-based curing model and slice modification algorithm that can be used in both continuous and layer-by-layer stereolithography to improve part fidelity and precisely map dose-dependent material properties, and we highlighted the need for resin flow modeling and exposure optimization in all continuous stereolithography technologies. It is my hope that this dissertation lays the groundwork for future theoretical and computational studies in stereolithography and accelerates developments in the field.

5.2 Continuing Work

While our efforts have enhanced understanding of dual-wavelength continuous stereolithography, there is still ample research to be done on this nascent technology. Dual-wavelength continuous stereolithography as well as stereolithography and additive manufacturing more broadly sit at the intersection of chemistry, fluid dynamics, heat transfer, and mass transfer; it is a field awaiting the contributions of chemical engineers.

5.2.1 Reciprocity Law in Projection Stereolithography

In verifying our kinetics-derived curing models, the resins we tested did not exhibit significant disagreement with the reciprocity assumption, despite evidence in the literature that it is unlikely to apply for 3D printing resins. Even the "default"

assumption of exclusively bimolecular termination in polymerization kinetics would suggest an exponential dependence of $m = 0.5$, not $m = 1$. The resins we considered represent a small subset of commercially available varieties, and future work could more broadly investigate the applicability of the reciprocity assumption in 3D printing resins and any potential effects of using DLP light sources.

5.2.2 Dead Zone Control in Dual-Wavelength Continuous Stereolithography

In addressing dead zone uniformity during continuous printing, we considered only a small subset of the optimization space. Future efforts might investigate the dead zone uniformity when using optimized patterned blue and UV intensities. Additionally, the role of UV intensity and nonreactive light absorbers were not investigated in our work. Experimentally, the efficacy of applying intensity functions from cylindrical parts to individual features in more complex parts could be considered, and variable intensity could be applied to both blue and UV with a suitable light source.

5.2.3 Unified Models for Dual-Wavelength Continuous Stereolithography

As I have suggested elsewhere, the printing process is affected by many variables and physical phenomena. Other physically relevant factors, such as part deformability, interfacial effects at the resin surface, and polymerization-driven variability in material properties and temperature could be considered in expanded models. Additionally, integration of cure-through correction and modeling of more complex parts could provide additional insights and corrective ability.

APPENDICES

APPENDIX A

Modelling and Correcting Cure-Through in Continuous Stereolithographic 3D Printing

A.1 Projector Calibration Data

Blue intensity calibration data for the dual-wavelength printer is shown in Figure A.1. The relationship between pixel value and light intensity is not linear and is found to be a piecewise function.

A.2 Derivation of Dose Equations

A.2.1 Derivation of Main Equations

The build platform begins in contact with the window and moves upward as the print proceeds. The coordinate system is defined with respect to the build platform, with $z = 0$ at the platform and increasing in the direction of the window (downward). Since the projected slices are patterned and intensity degrades as the light propagates, dose and intensity are functions of x, y, and z; however, for simplicity our notation will only include z with the understanding that each equation applies at a particular (x, y) position. Printing consists of both continuous and discrete processes: as the build platform continuously ascends, exposure patterns change at discrete intervals with each slice projected in sequence. To account for the discrete projection of slices, the total accumulated dose at a point is a sum of contributions

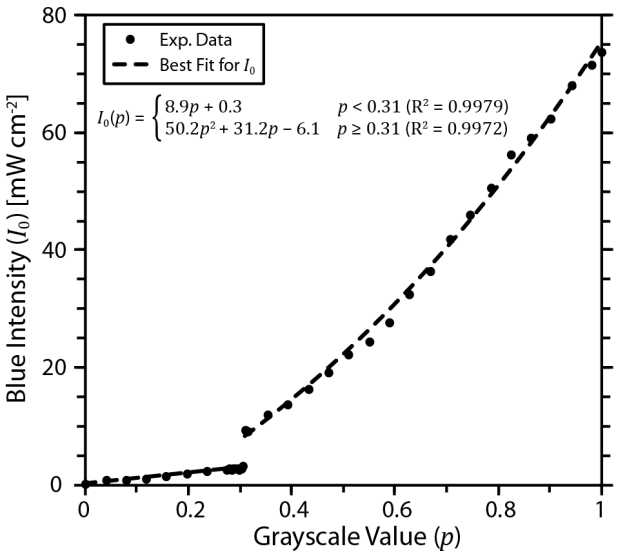

Figure A.1. Projector calibration curve. Measured blue intensity, I_0, is plotted as a function of the grayscale value, p, of the displayed image. The calibration curve is found to be a piece-wise function typical of manufacturer color balancing encoded into projector firmware.

from each slice projected. $D_{\mathrm{T}}(z)$ is the total dose delivered to position z in the final part; the contribution of slice n to the total dose is denoted as $D_{\mathrm{n}}(z)$. Thus,

$$D_{\mathrm{T}}(z) = \sum_{n=0}^{N} D_{\mathrm{n}}(z) \tag{A.1}$$

where slices are numbered from 0 to N in the order of exposure.

To determine the dose contribution from each slice as the build platform continuously ascends, we integrate over the time period when the slice is projected. The change in dose at a point is given by:

$$\frac{\partial}{\partial t} D_{\mathrm{n}}(z,t) = -\frac{\partial}{\partial z} I_{\mathrm{n}}(z,t) \tag{A.2}$$

where t is time and I_{n} is the light intensity for slice n. The light intensity at any depth in the resin bath, $I_{\mathrm{n}}(z)$, is given by Beer's Law. Recalling that $z = 0$ at the build platform, $z_{\mathrm{w}} - z$ gives the distance from the position of the window (z_{w}) to the position of interest (z). From Beer's Law,

$$\frac{\partial}{\partial z} I_{\mathrm{n}}(z,t) = -\frac{\ln 10}{h_{\mathrm{a}}} I_{\mathrm{n,w}} 10^{-[z_{\mathrm{w}} t - z] h_a^{-1}} \tag{A.3}$$

where $I_{\mathrm{n,w}} = I_{\mathrm{n}}(z_{\mathrm{w}})$ is the incident intensity and h_{a} is the resin absorbance height (the inverse of the absorption coefficient). Movement of the build platform is included via the print speed. Since the coordinate system is defined with respect to the build platform, the print speed s is represented in terms of the ever-increasing value of $z_{\mathrm{w}}(t)$:

$$s = \frac{dz_{\mathrm{w}}}{dt} \tag{A.4}$$

Substituting Equation A.4 and A.3 into Equation A.2,

$$\frac{\partial}{\partial z_{\mathrm{w}}} D_{\mathrm{n}}(z, z_{\mathrm{w}}) = \frac{\ln 10}{s h_{\mathrm{a}}} I_{\mathrm{n,w}} 10^{-[z\mathrm{w}(t)-z]h_{\mathrm{a}}^{-1}} \tag{A.5}$$

To calculate the dose contribution from slice n, Equation A.5 is integrated with respect to z_{w}. The limits of integration are the values of z_{w} when slice n is first projected and when the next slice, $n+1$, is projected: nh_{s} and $(n+1)h_{\mathrm{s}}$, respectively, where h_{s} is the slicing height. Thus,

$$\begin{aligned} D_{\mathrm{n}}(z) &= \int_{nh_{\mathrm{s}}}^{(n+1)h_{\mathrm{s}}} \frac{\ln 10}{s h_{\mathrm{a}}} I_{\mathrm{n,w}} 10^{-[z_{\mathrm{w}}(t)-z]h_{\mathrm{a}}^{-1}} \\ &= \frac{I_{\mathrm{n,w}}}{s} \left\{ 10^{-(nh_{\mathrm{s}}-z)h_{\mathrm{a}}^{-1}} - 10^{-[(n+1)h_{\mathrm{s}}-z]h_{\mathrm{a}}^{-1}} \right\} \end{aligned} \tag{A.6}$$

If the cross-section at height z is exposed to slice n (i.e., $z \leq nh_{\mathrm{s}}$), Equation A.6 gives the contribution of slice n to the total dose at that point. If the cross-section is not exposed to slice n (i.e., $z \geq (n+1)h_{\mathrm{s}}$), the dose contribution is zero. As a simplification, we will consider only values of z which are multiples of h_{s} (i.e., z-values of simulated slices). For a treatment of all real values of z, see Appendix A.3 below. Note that this model implicitly assumes that a packet of resin tends to stay in the same (x, y, z)-position as the print progresses.

Combining Equation A.1 and A.6,

$$D_{\mathrm{T}}(z) = \sum_{n=0}^{N} \frac{I_{\mathrm{n,w}}}{s} \left\{ 10^{-(nh_{\mathrm{s}}-z)h_{\mathrm{a}}^{-1}} - 10^{-[(n+1)h_{\mathrm{s}}-z]h_{\mathrm{a}}^{-1}} \right\} \tag{A.7}$$

Equation A.7 allows calculation of the total accumulated dose at any point in the final printed part.

For convenience we may define several dimensionless variables. The dimensionless dose, Ω, is normalized by the critical dose, D_c:

$$\Omega_n \equiv \frac{D_n}{D_c} \tag{A.8}$$

The critical dose is experimentally determined for each resin formulation and is related to the dose at which the resin becomes insoluble in the rinse solvent, IPA (i.e., reaches the gelation point). A resin packet with $\Omega_T < 1$ is considered uncured, while resin with $\Omega_T \geq 1$ is considered cured. The dimensionless light intensity at the window, Φ, is normalized by a critical intensity; I_c is the minimum intensity at which it is possible to reach D_c for h_a and s (for additional discussion, see Appendix A.3 below).

$$\Phi_n \equiv \frac{I_{n,w}}{I_c} = \frac{I_{n,w}}{D_c s} \tag{A.9}$$

The dimensionless z-position, ζ, is normalized by the slice height:

$$\zeta \equiv \frac{z}{h_s} \tag{A.10}$$

With this normalization, slice n is first projected when $\zeta_w = n$. Finally, the dimensionless constant η is the ratio of the slicing height to the absorbance height:

$$\eta \equiv \frac{h_s}{h_a} \tag{A.11}$$

Rewriting Equation A.7 in dimensionless terms,

$$\Omega_T(\zeta) = \sum_{n=\zeta}^{N} \Phi_n \left(10^{-(n-\zeta)\eta} - 10^{-[(n+1)-\zeta]\eta}\right) \tag{A.12}$$

As derived in Appendix A.2.4 below, Equation A.12 can be simplified such that $\Omega_T(\zeta)$ is a function of $\Omega_T(\zeta+1)$:

$$\Omega_T(\zeta) = \Phi_\zeta(1 - 10^{-\eta}) + \Omega_T(\zeta+1)10^{-\eta} \tag{A.13}$$

Table A.1. Total dose by layer (from Equation A.13).

ζ	$\Omega_{\mathrm{T}}(\zeta)$
N	$\Phi_{\mathrm{N}}(1-10^{-\eta})$
$N-1$	$\Phi_{\mathrm{N}-1}(1-10^{-\eta})+\Omega_{\mathrm{T}}(N)10^{-\eta}$
...	...
0	$\Phi_0(1-10^{-\eta})+\Omega_{\mathrm{T}}(1)10^{-\eta}$

In Equation A.13, we find the relationship that will allow quick dose calculation and slice correction. Starting at the end of the part (i.e., $\zeta = N$), we may calculate the total dose in each layer sequentially by considering only the current layer and the preceding layer. Table A.1 gives expressions for Ω_{T} at several values of ζ.

A.2.2 Fractional Values of ζ

When non-integer values of ζ are considered, there are three important cases for determining the value of $\Omega_{\mathrm{n}}(\zeta)$. Recalling that ζ_{w}, the window position, increases constantly as the build platform ascends, these cases are delineated by the value of ζ and the values of ζ_{w} while the slice n is projected. As noted above, $\zeta_{\mathrm{w}} = n$ when slice n is first projected, and the next slice is projected at $\zeta_{\mathrm{w}} = n + 1$.

With the ζ_{w} values for each slice known, we may consider the three cases for $\Omega_{\mathrm{n}}(\zeta)$. In the first case, the cross-section at ζ is never exposed while slice n is projected (i.e., $\zeta_{\mathrm{w}} < \zeta$ during the entire period slice n is projected). Here, the value of $\Omega_{\mathrm{n}}(\zeta)$ is simply zero.

$$\Omega_{\mathrm{n}}(\zeta) = 0, \quad n+1 < \zeta \leq N \tag{A.14}$$

with N corresponding to the final slice.

In the second case, the cross-section at ζ is first exposed during slice n (i.e., $\zeta_{\mathrm{w}} = \zeta$ at some point while the slice is projected). To handle this case will require a more generic form of Equation A.6. Considering a constant exposure from $z_{\mathrm{w}} = z_{\mathrm{w},1}$ to

$z_{\mathrm{w}} = z_{\mathrm{w},2}$:

$$\frac{\partial}{\partial z_{\mathrm{w}}} D(z, z_{\mathrm{w}}) = \frac{\ln 10}{s h_{\mathrm{a}}} I_{\mathrm{n,w}} 10^{-[z_{\mathrm{w}}(t)-z]h_{\mathrm{a}}^{-1}} \tag{A.15}$$

$$\begin{aligned} D(z) &= \int_{z_{\mathrm{w},1}}^{z_{\mathrm{w},2}} \frac{\ln 10}{s h_{\mathrm{a}}} I_{\mathrm{n,w}} 10^{-[z_{\mathrm{w}}(t)-z]h_{\mathrm{a}}^{-1}} \mathrm{d}z_{\mathrm{w}} \\ &= \frac{I_{\mathrm{n,w}}}{s} \left[10^{-(z_{\mathrm{w},1}-z)h_{\mathrm{a}}^{-1}} - 10^{-(z_{\mathrm{w},2}-z)h_{\mathrm{a}}^{-1}} \right] \end{aligned} \tag{A.16}$$

$$\Omega(\zeta) = \Phi \left[10^{-(\zeta_{\mathrm{w},1}-\zeta)\eta} - 10^{-(\zeta_{\mathrm{w},2}-\zeta)\eta} \right] \tag{A.17}$$

For this case, the dose contribution is zero while $\zeta_{\mathrm{w}} < \zeta$. Integrating Equation A.17 with limits $\zeta_{\mathrm{w},1} = \zeta$ and $\zeta_{\mathrm{w},2} = n + 1$,

$$\begin{aligned} \Omega_n(\zeta) &= \Phi_n \left\{ 10^{-(\zeta-\zeta}\eta - 10^{-[(n+1)-\zeta]\eta} \right\}, \quad n < \zeta \leq n+1 \\ &= \Phi_n \left\{ 1 - 10^{-[(n+1)-\zeta]\eta} \right\} \end{aligned} \tag{A.18}$$

In the final case, ζ is exposed for the entire duration of the slice (i.e., $\zeta_{\mathrm{w}} > \zeta$ during the entire period slice n is projected). Here, Equation A.17 applies with $\zeta_{\mathrm{w},1} = \zeta$ and $\zeta_{\mathrm{w},2} = n + 1$.

$$\Omega_n(\zeta) = \Phi_n \left\{ 10^{-(n-\zeta)\eta} - 10^{-[(n+1)-\zeta]\eta} \right\}, \quad 0 \leq \zeta \leq n \tag{A.19}$$

Combining Equation A.14, A.18, A.19 into a single expression for $\Omega_n(\zeta)$,

$$\Omega_n(\zeta) = \begin{cases} 0, & n+1 < \zeta \leq N \\ \Phi_n \left\{ 1 - 10^{-[(n+1)-\zeta]\eta} \right\}, & n < \zeta \leq n+1 \\ \Phi_n \left\{ 10^{-(n-\zeta)\eta} - 10^{-[(n+1)-\zeta]\eta} \right\}, & 0 \leq \zeta \leq n \end{cases} \tag{A.20}$$

Equation A.20 allows us to determine the contribution of any particular slice to the dose at any point.

To use Equation A.1 with a non-integer value of ζ, it is necessary to rewrite the conditions in Equation A.20. Using floor bracket notation, where $\lfloor \zeta \rfloor$ indicates the value of ζ rounded down to the nearest integer, the first case occurs for $0 \leq n < \lfloor \zeta \rfloor$,

the second case occurs only for $n = \lfloor \zeta \rfloor$, and the third case occurs for $\lfloor \zeta \rfloor < n \leq N$. Rewriting Equation A.20 with these conditions:

$$\Omega_n(\zeta) = \begin{cases} 0, & 0 \leq n < \lfloor \zeta \rfloor \\ \Phi_n \left\{ 1 - 10^{-[(n+1)-\zeta]\eta} \right\}, & n = \lfloor \zeta \rfloor \\ \Phi_n \left\{ 10^{-(n-\zeta)\eta} - 10^{-[(n+1)-\zeta]\eta} \right\}, & \lfloor \zeta \rfloor < n \leq N \end{cases} \tag{A.21}$$

Applying Equation A.21 to Equation A.1,

$$\Omega_{\mathrm{T}}(\zeta) = \Phi_{\lfloor \zeta \rfloor} \left[1 - 10^{-(\lfloor \zeta \rfloor - \zeta)\eta} \right] + \sum_{n=\lfloor \zeta \rfloor + 1}^{N} \Phi_n \left\{ 10^{-(n-\zeta)\eta} - 10^{-[(n+1)-\zeta]\eta} \right\} \tag{A.22}$$

Equation A.22 allows calculation of the total dose at non-integer values of ζ.

A.2.3 Critical Intensity I_{c} and Dimensionless Intensity Φ

I_c is defined as the minimum intensity for which it is possible to reach the critical dose. This theoretical limit is reached for an infinitely long exposure—that is, when exposure occurs over a z_{w} range from z to ∞. Integrating Equation A.15 with these limits,

$$\begin{aligned} D_{\mathrm{c}} &= \int_z^{\infty} \frac{\ln 10}{s h_{\mathrm{a}}} I_{\mathrm{n,w}} 10^{-(z_{\mathrm{w}} - z) h_{\mathrm{a}}^{-1}} \mathrm{d}z_{\mathrm{w}} \\ &= \frac{I_{\mathrm{c}}}{s} \left[10^{-(z-z) h_{\mathrm{a}}^{-1}} \right] \\ &= \frac{I_{\mathrm{c}}}{s} (1 - 0) \\ &= \frac{I_{\mathrm{c}}}{s} \end{aligned} \tag{A.23}$$

Rearranging and substituting into Φ,

$$I_{\mathrm{c}} = D_{\mathrm{c}} s \tag{A.24}$$

$$\Phi_n \equiv \frac{I_{\mathrm{n,w}}}{I_{\mathrm{c}}} = \frac{I_{\mathrm{n,w}}}{D_{\mathrm{c}} s} \tag{A.25}$$

Similarly, Φ defines the asymptotic value of the dose as the exposure time tends to infinity. Substituting $\zeta_{\mathrm{w},1} = \zeta$ and $\zeta_{\mathrm{w},2} = \infty$ into Equation A.17,

$$\begin{aligned}\Omega_{\mathrm{w}}(\zeta) &= \Phi\left[10^{-(\zeta-\zeta)\eta} - 10^{-(\infty-\zeta)\eta}\right] \\ &= \Phi(1-0) \\ &= \Phi\end{aligned} \tag{A.26}$$

A.2.4 Dependence of $\Omega_{\mathrm{T}}(\zeta)$ on $\Omega_{\mathrm{T}}(\zeta+1)$

If we contrast the total doses at ζ and $\zeta+1$, we will find that the doses are interrelated. $\Omega_{\mathrm{T}}(\zeta)$ is given by Equation A.1:

$$\begin{aligned}\Omega_{\mathrm{T}}(\zeta) &= \sum_{n=\zeta}^{N} \Omega_{\mathrm{n}}(\zeta) \\ &= \Omega_{\zeta}(\zeta) + \sum_{n=\zeta+1}^{N} \Omega_{\mathrm{n}}(\zeta)\end{aligned} \tag{A.27}$$

Here, the sum has been split into two terms: first, the contribution from slice ζ and second, the contributions from all remaining slices. Looking more closely at the second term:

$$\begin{aligned}\Omega_{\mathrm{n}}(\zeta) &= \Phi_{\mathrm{n}}\left\{10^{-(n-\zeta)\eta} - 10^{-[(n+1)-\zeta]\eta}\right\}, \quad \zeta+1 \le n < N \\ &= \Phi_{\mathrm{n}}\left\{10^{-[n-(\zeta+1)]\eta} - 10^{-[(n+1)-(\zeta+1)]\eta}\right\} 10^{-\eta} \\ &= \Omega_{\mathrm{n}}(\zeta+1)10^{-\eta}\end{aligned} \tag{A.28}$$

Equation A.28 shows that the contribution of slice n (where $n \le \zeta$) to the dose at ζ is equivalent to the contribution of slice n to the dose at $\zeta+1$, multiplied by a factor of $10^{-\eta}$. Substituting back into Equation A.27,

$$\Omega_{\mathrm{T}}(\zeta) = \Omega_{\zeta}(\zeta) + \sum_{n=\zeta+1}^{N} \Omega_{\mathrm{n}}(\zeta+1)\, 10^{-\eta} \tag{A.29}$$

Considering the left term:

$$\begin{aligned}\Omega_\zeta(\zeta) &= \Phi_\zeta \left\{10^{-(\zeta-\zeta)\eta} - 10^{-[(\zeta+1)-\zeta]\eta}\right\} \\ &= \Phi_\zeta \left(1 - 10^{-\eta}\right)\end{aligned} \tag{A.30}$$

And the right:

$$\begin{aligned}\sum_{n=\zeta+1}^{N} \Omega_\mathrm{n}(\zeta+1)\, 10^{-\eta} &= 10^{-\eta} \sum_{n=\zeta+1}^{N} \Omega_\mathrm{n}(\zeta+1) \\ &= 10^{-\eta}\, \Omega_\mathrm{T}(\zeta+1)\end{aligned} \tag{A.31}$$

On recombination,

$$\Omega_\mathrm{T}(\zeta) = \Phi_\zeta \left(1 - 10^{-\eta}\right) + \Omega_\mathrm{T}(\zeta+1)10^{-\eta} \tag{A.32}$$

In Equation A.32, we find the relationship that will allow quick dose calculation and slice correction. Starting at the end of the part (i.e., $\zeta = N$) and moving upward slice-by-slice, we may calculate the cumulative dose in each layer sequentially by considering only the current layer and the preceding layer. Table A.1 gives expressions for Ω_T at several values of ζ.

A.3 Effect of Finite Contrast Ratio

A deeper examination of behavior while black pixels are projected will highlight the significance of the projector contrast ratio. The contrast ratio of a display system is defined as the ratio of intensities for white and black; this is a finite quantity since pure black (i.e., an irradiance of zero) is unachievable. Consider a point ζ in the part envelope with a corresponding grayscale pixel value—that is, the pixel value for slice $n = \zeta$—is zero. From Equation A.13, the total dose at this position depends on the minimum intensity and the total dose of the layer below:

$$\Omega_\mathrm{T}(\zeta) = \Phi_\mathrm{min}(1 - 10^{-\eta}) + \Omega_\mathrm{T}(\zeta+1)\, 10^{-\eta} \tag{A.33}$$

When the dose contribution from the minimum intensity matches the exponential decay from the dose at $\zeta + 1$, a constant dose is maintained:

$$\begin{aligned} \Omega_{\min}(\zeta) &= \Phi_{\min}(1 - 10^{-\eta}) + \Omega_{\min}10^{-\eta} \\ &= \Phi_{\min} \end{aligned} \tag{A.34}$$

This dose, $\Omega_{\min}$, acts as an effective minimum dose: if $\Omega_{\mathrm{T}} \geq \Omega_{\min}$ at position (x_0, y_0, z_0), then $\Omega_{\mathrm{T}} \geq \Omega_{\min}$ for all points $(x_0, y_0, z \leq z_0)$. The minimum dose is determined by the resin properties and the print speed as well as the contrast ratio of the projection system. For our printer, we have measured a minimum intensity of 1 mW cm^{-2}, resulting in a minimum dose of approximately 36 mJ cm^{-3} (varying with other parameters).

A.4 Equations for Target Dose Region Constraints

In a region of constant-intensity exposure, the dose at any point can be calculated if the dose at one point is known. If ζ_0 and Ω_0 are the known position and dose and Φ_0 is the constant intensity,

$$\Omega(\zeta) = \Omega_0 10^{-(\zeta_0 - \zeta)\eta} + \Phi_0 \left[1 - 10^{-(\zeta_0 - \zeta)\eta}\right] \tag{A.35}$$

For the constraint curves defining target dose regions, each curve has a constant intensity exposure ($\Phi_{\max}$ for constraint (ii) and $\Phi_{\min}$ for constraint (iii)), and the dose at the top and bottom edges are known (Ω_{c}). If the upper and lower edges of the feature are located at ζ_{U} and ζ_{L} (see Figure A.2),

$$\Omega_{\mathrm{ii}}(\zeta) = \Omega_c 10^{-(\zeta_{\mathrm{L}} - \zeta)\eta} + \Phi_{\max} \left[10^{-(\zeta_{\mathrm{L}} - \zeta)\eta}\right] \tag{A.36}$$

$$\Omega_{\mathrm{iii}}(\zeta) = \Omega_c 10^{-(\zeta_{\mathrm{U}} - \zeta)\eta} + \Phi_{\min} \left[1 - 10^{-(\zeta_{\mathrm{U}} - \zeta)\eta}\right] \tag{A.37}$$

The constraint curves, and thus the target dose region, are dependent on several

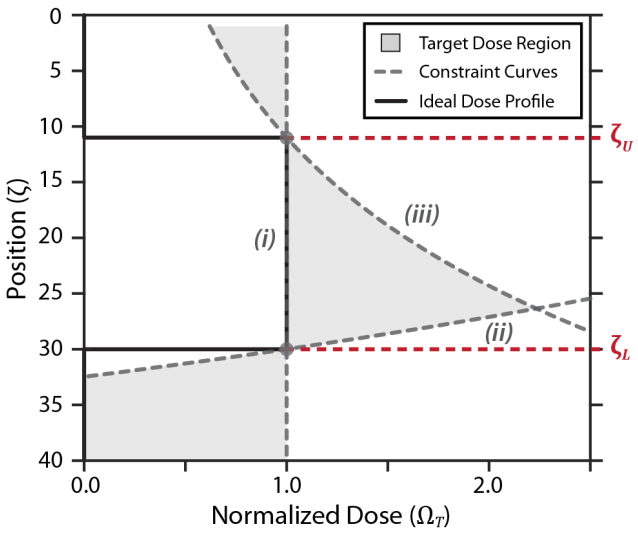

Figure A.2. Dose constraint curves *(i)* – *(iii)* and target dose region. ζ_{U} and ζ_{L} are the positions of the top and bottom of the feature, respectively.

system parameters. The relative effect of a change in each parameter is shown below in Figure A.3.

In Figure 2.3, we compare dose profiles with varying maximum doses; however, the chosen maximum dose may not be reached for some features. As is evident from Figure A.3, several factors determine the shape of the target dose region for a feature. While most parameters are constant throughout the print ($I_{\max}$, s, and h_{a}), the feature size may vary considerably. For a constant set of system parameters, each feature has a maximum achievable $\Omega_{\max}$ as a function of its height. To determine this value, Equations A.36 and A.37 are first equated to determine the point at which the curves meet.

$$\zeta^* = \frac{1}{\eta} \log_{10}\left[\frac{\Phi_{\max} - \Phi_{\min}}{(\Omega_{\mathrm{c}} - \Phi_{\min})10^{-\zeta_{\mathrm{U}}\eta} - (\Omega_{\mathrm{c}} - \Phi_{\max})10^{-\zeta_{\mathrm{L}}\eta}}\right] \tag{A.38}$$

Using Equation A.38, we can write the maximum dose (assuming the edges are at the critical dose) as a function of feature height:

$$\delta \equiv \zeta_{\mathrm{L}} - \zeta_{\mathrm{U}} \tag{A.39}$$

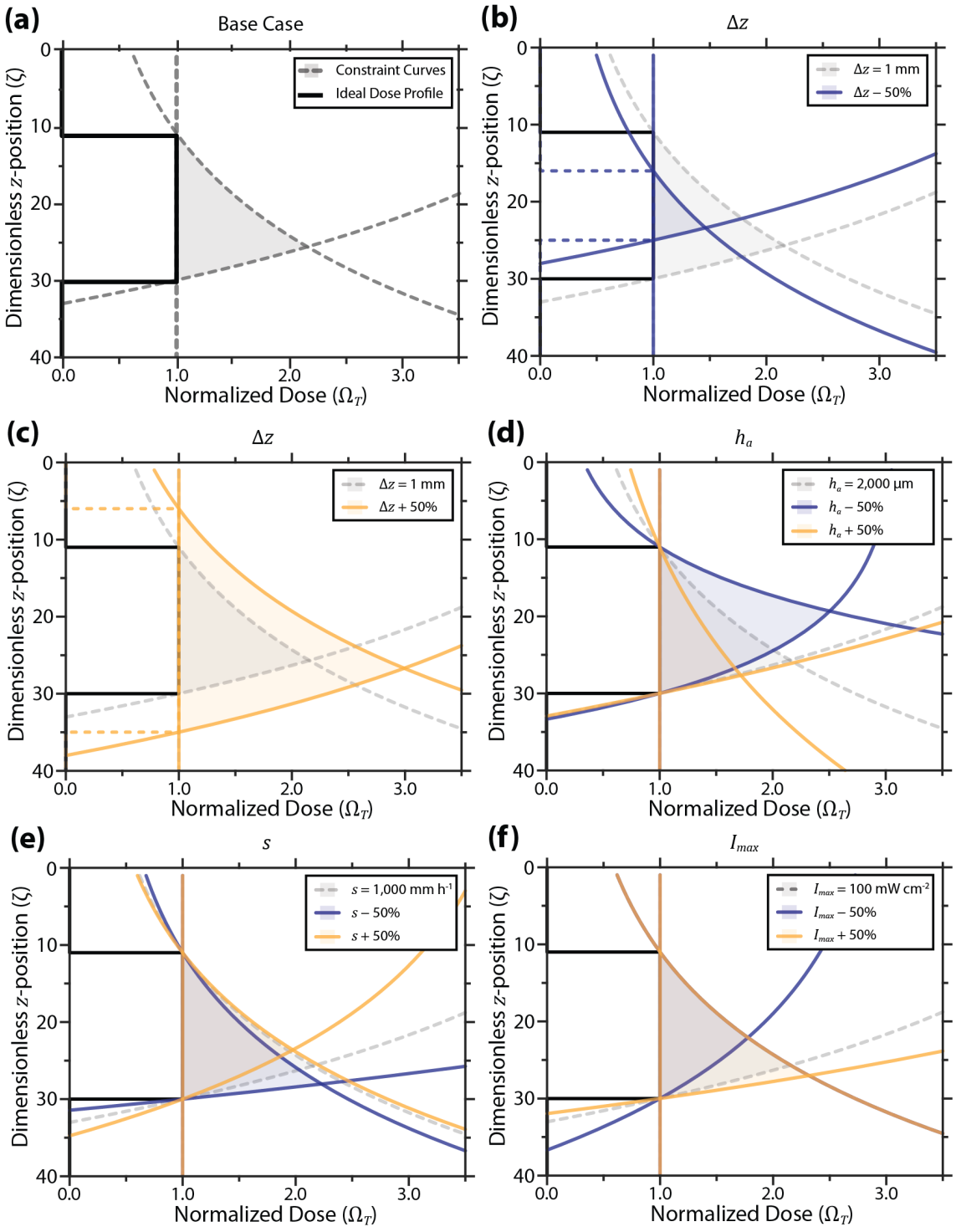

Figure A.3. Effect of increasing (yellow curves) and decreasing (blue curves) parameters by 50%: **(a)** Base case. $h_s = 50\,\mu m$, $\Delta z = 1\,mm$, $h_a = 2{,}000\,\mu m$, $s = 1{,}000\,mm\,h^{-1}$, and $I_{max} = 100\,mW\,cm^{-2}$. **(b)** Decreasing feature height. **(c)** Increasing feature height. **(d)** Varying absorbance height. **(e)** Varying print speed. From Equation A.9, varying the critical dose has an identical effect. **(f)** Varying the maximum projector intensity.

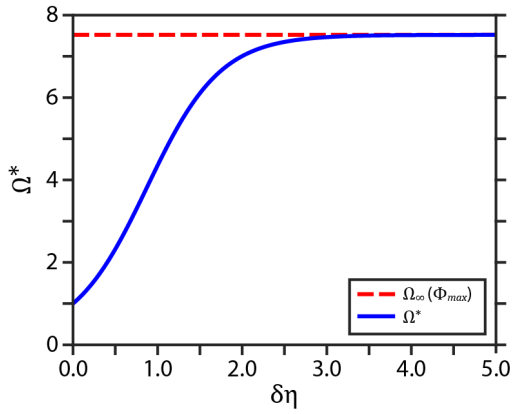

Figure A.4. Maximum dose as a function of $\delta\eta = (z_{\mathrm{L}} - z_{\mathrm{U}})h_{\mathrm{a}}^{-1}$. As the feature height increases, the maximum dose approaches the limit Ω_∞ described in Appendix A.4. Parameters: $h_{\mathrm{s}} = 50\,\mu\mathrm{m}$, $h_{\mathrm{a}} = 2{,}000\,\mu\mathrm{m}$, $s = 1{,}000\,\mathrm{mm\,h^{-1}}$, $I_{\max} = 120\,\mathrm{mW\,cm^{-2}}$, $I_{\min} = 2\,\mathrm{mW\,cm^{-2}}$.

$$\begin{aligned}
\zeta^* &= \frac{1}{\eta}\log_{10}\left[\frac{\Phi_{\max}-\Phi_{\min}}{(\Omega_{\mathrm{c}}-\Phi_{\min})10^{-\zeta_{\mathrm{U}}\eta}-(\Omega_{\mathrm{c}}-\Phi_{\max})10^{-(\zeta_{\mathrm{U}}+\delta)\eta}}\right] \\
&= \frac{1}{\eta}\log_{10}\left[\frac{\Phi_{\max}-\Phi_{\min}}{(\Omega_{\mathrm{c}}-\Phi_{\min})10^{-\zeta_{\mathrm{U}}\eta}-(\Omega_{\mathrm{c}}-\Phi_{\max})10^{-\delta\eta}}\frac{1}{10^{-\zeta_{\mathrm{U}}\eta}}\right] \\
&= \frac{1}{\eta}\log_{10}\left[\frac{\Phi_{\max}-\Phi_{\min}}{(\Omega_{\mathrm{c}}-\Phi_{\min})10^{-\zeta_{\mathrm{U}}\eta}-(\Omega_{\mathrm{c}}-\Phi_{\max})10^{-\delta\eta}}\right]-\frac{1}{\eta}\log_{10}\left(10^{-\zeta_{\mathrm{U}}\eta}\right) \\
&= \frac{1}{\eta}\log_{10}\left[\frac{\Phi_{\max}-\Phi_{\min}}{(\Omega_{\mathrm{c}}-\Phi_{\min})10^{-\zeta_{\mathrm{U}}\eta}-(\Omega_{\mathrm{c}}-\Phi_{\max})10^{-\delta\eta}}\right]+\zeta_{\mathrm{U}}
\end{aligned} \tag{A.40}$$

Substituting Equation A.40 into Equation A.37,

$$\Omega^* \equiv \Omega(\zeta^*) = \frac{(\Omega_{\mathrm{c}}-\Phi_{\min})(\Phi_{\max}-\Phi_{\min})}{(\Omega_{\mathrm{c}}-\Phi_{\min})-(\Omega_{\mathrm{c}}-\Phi_{\max})10^{-\delta\eta}}+\Phi_{\min} \tag{A.41}$$

Figure A.4 shows Ω^* as a function of feature height.

A.5 Optimizing D_{c} and $\Omega_{\max}$

Effective slice correction requires that correction parameters are optimized for the resin being used. Figure A.5 illustrates two limits on the maximum achievable dose for printing with Resin 1 at 750 mm $\mathrm{h^{-1}}$; these limits exist independently from the chosen value of $\Omega_{\max}$. As discussed in Appendix A.4, an infinitely long exposure at Φ asymptotically approaches the dose $\Omega_\infty(\Phi)$. Thus, the maximum intensity defines a maximum possible dose in the model: $\Omega_\infty(\Phi_{\max}) = \Phi_{\max}$. Figure A.5(a) shows the

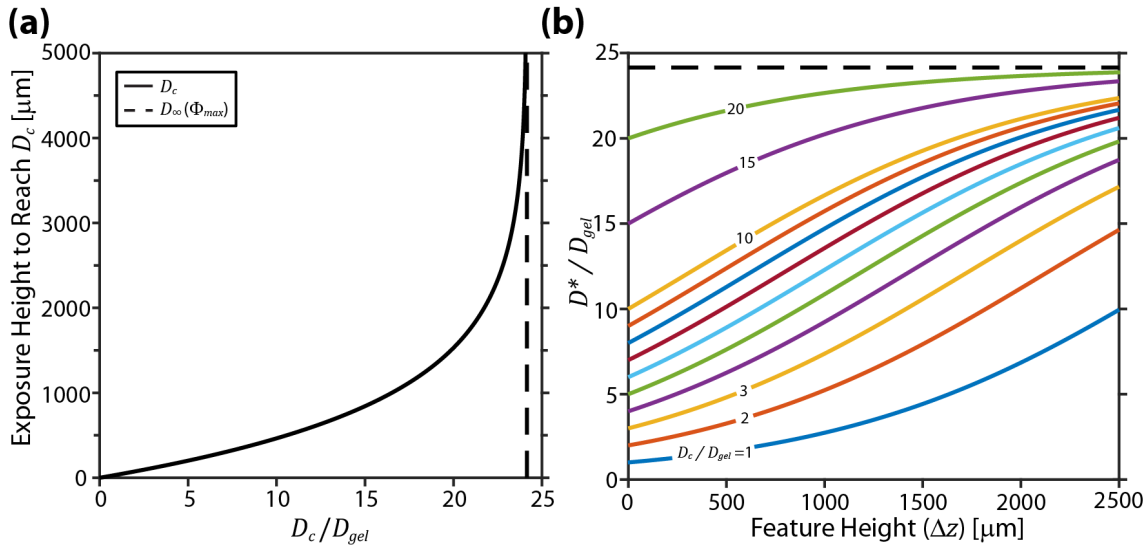

Figure A.5. Maximum dose limits for our presented optimization (Resin 1, $s = 750\,\mathrm{mm\,h^{-1}}$, $I_{\max} \approx 75\,\mathrm{mW\,cm^{-2}}$). **(a)** Exposure height to reach the critical dose starting from zero dose. Printing at a constant speed, larger height ranges must be exposed to reach higher doses. **(b)** The maximum possible dose for a feature of a given height, as determined by the dose constraint equations (Equation A.41 in Appendix A.4). When the correction is applied, the maximum dose within a feature is the minimum of D^* and the chosen $D_{\max}$.

distance that must be exposed at the maximum intensity before the critical dose is reached. This relationship suggests than certain feature-dense geometries may not be amenable to correction with these print settings; however, slower print speeds or higher light intensities may be used to compress the curve downward (for a constant exposure height, $D \propto Is^{-1}$).

For individual features, the maximum dose is the lesser of the prescribed $\Omega_{\max}$ and Ω^* as defined in Appendix A.4. Analogous to Figure A.4, Figure A.5(b) shows D^*/D_{gel} as a function of feature height for Resin 1 at $750\,\mathrm{mm\,h^{-1}}$ and several values of D_{c}.

In addition to optimizing the critical dose parameter D_{c}, we also conducted experiments investigating the effect of the maximum dose parameter $\Omega_{\max}$, with results shown in Figure A.6. Setting higher values of $D_{\max}$ makes the fidelity less sensitive

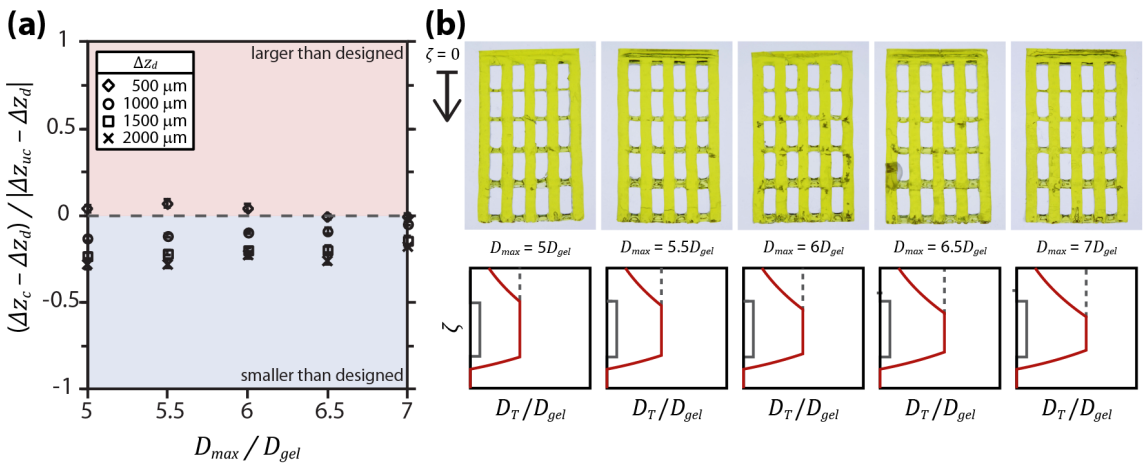

Figure A.6. Varying $D_{\max}$ with $D_c = 5D_{gel}$. **(a)** Ratio of height errors (corrected-to-uncorrected) for a range of feature sizes and values of $D_{\max}$. A ratio of zero corresponds to a perfectly corrected feature. Error bars indicate standard error. **(b)** Parts printed at 750 mm h^{-1} using slices corrected with $D_c = 5D_{gel}$ and different values for $D_{\max}$.

to feature size, though the effect is minor. Based on this result and the desire to maximize green strength, we chose to operate the correction with an unconstrained maximum dose ($\Omega_{\max} = \infty$).

A.6 Model and Correction for Non-Continuous Stereolithography

While the main body of this work relates to continuous stereolithography, we present here an adapted model and correction approach for use with traditional layer-by-layer stereolithography. Our dose model is similar to those previously reported [44, 45]. While grayscale has previously been used to improve x-y resolution [52], it has not, to our knowledge, been explored as a solution for cure-through. The compensation zone approach was partly developed to address cure-through artifacts on exterior features by adjusting the dimensions of the model through an optimization process [43, 48]. A compensation-zone-like approach was subsequently developed for internal voids [41]. Manual adjustments to account for cure-through have also been reported [49]. These references also provide background on the layer-by-layer

printing process for unfamiliar readers.

A.6.1 Derivation of Dose Model

As in the continuous case, the total dose at a point is the sum of contributions from all slices.

$$D_{\mathrm{T}}(z) = \sum_{n=0}^{N} D_{\mathrm{n}}(z) \tag{A.42}$$

$$\begin{aligned} \frac{\partial}{\partial t} D_{\mathrm{n}}(z,t) &= -\frac{\partial}{\partial z} I_{\mathrm{n}}(z,t) \\ &= \frac{\ln 10}{h_{\mathrm{a}}} I_{\mathrm{n,w}} 10^{-(nh_{\mathrm{s}}-z)h_{\mathrm{a}}^{-1}} \end{aligned} \tag{A.43}$$

For layer-by-layer exposure, each slice is exposed for time t_{e} while the build platform is stationary. For slices to which position z is not exposed ($n < zh_{\mathrm{s}}^{-1}$), $D_{\mathrm{n}}(z) = 0$. If z is exposed to slice n ($n \geq zh_{\mathrm{s}}^{-1}$), the dose is given by:

$$\begin{aligned} D_{\mathrm{n}}(z) &= \int_0^{t_e} \frac{\ln 10}{h_{\mathrm{a}}} I_{\mathrm{n,w}} 10^{-(nh_{\mathrm{s}}-z)h_{\mathrm{a}}^{-1}} \mathrm{d}t \\ &= \frac{\ln 10}{h_{\mathrm{a}}} I_{\mathrm{n,w}} 10^{-(nh_{\mathrm{s}}-z)h_{\mathrm{a}}^{-1}} t_{\mathrm{e}} \end{aligned} \tag{A.44}$$

$$D_{\mathrm{T}}(z) = \sum_{n=\lceil zh_{\mathrm{s}}^{-1} \rceil}^{N} \frac{\ln 10}{h_{\mathrm{a}}} I_{\mathrm{n,w}} 10^{-(nh_{\mathrm{s}}-z)h_{\mathrm{a}}^{-1}} t_{\mathrm{e}} \tag{A.45}$$

Dimensionless variables for the layer-by-layer model are identical to those used in the continuous model with the exception of dimensionless intensity, which is now

$$\Phi'_{\mathrm{n}} \equiv \frac{I_{\mathrm{n,w}}}{I'_{\mathrm{c}}} = \frac{I_{\mathrm{n,w}} t_{\mathrm{e}} \ln 10}{D_{\mathrm{c}} h_{\mathrm{a}}} \tag{A.46}$$

Substituting dimensionless variables into Equation A.45,

$$\Omega_{\mathrm{T}}(\zeta) = \sum_{n=\lceil \zeta \rceil}^{N} \Phi'_{\mathrm{n}} 10^{-(n-\zeta)\eta} \tag{A.47}$$

Equation A.47 can be used to calculate the total accumulated dose at any point in a part printed using layer-by-layer stereolithography.

A.6.2 Slice Correction

In non-continuous stereolithography, the exposure time is set such that the far edge of the current layer reaches the critical dose. In our notation, this position is $\zeta = n - 1$ for each slice n. Since the points of interest are integer values of ζ, we may perform a simplification analogous to Equation A.32 from the continuous case to assist in correction:

$$\Omega_{\mathrm{c}} = \Phi'_{\zeta+1}\, 10^{-\eta} + \Omega_{\mathrm{T}}(\zeta + 2)\, 10^{-2\eta} \tag{A.48}$$

As with the continuous case, the correction is performed starting at the end of the part ($\zeta = N$) and moving upward slice-by-slice. From Equation A.48, the intensity required to reach the critical dose can be determined for each layer within a designed feature.

We applied the dose model and slice correction for layer-by-layer stereolithography to a test model identical to that used in Figure 2.2 and 2.4. Figure A.7(a – d) shows the model results for uncorrected slices, while Figure A.7(e – h) shows the results for corrected slices. These results, along with the discussion below, show how slice correction can be used in combination with resin and printer optimization to minimize cure-through in non-continuous stereolithography.

For both corrected and uncorrected slices, a characteristic sawtooth pattern resulting from discontinuous build platform motion is evident in the dose profile. These discontinuities together with the nonzero background intensity of the projection system have the effect of preventing "perfect" correction using our method. If the top edge of a feature is just at the critical dose, there will be cure-through into the region just above it resulting from additional exposure at the minimum intensity. The height of the minimum cure-through region, z_{CT} (dimensionless: ζ_{CT}), is a function

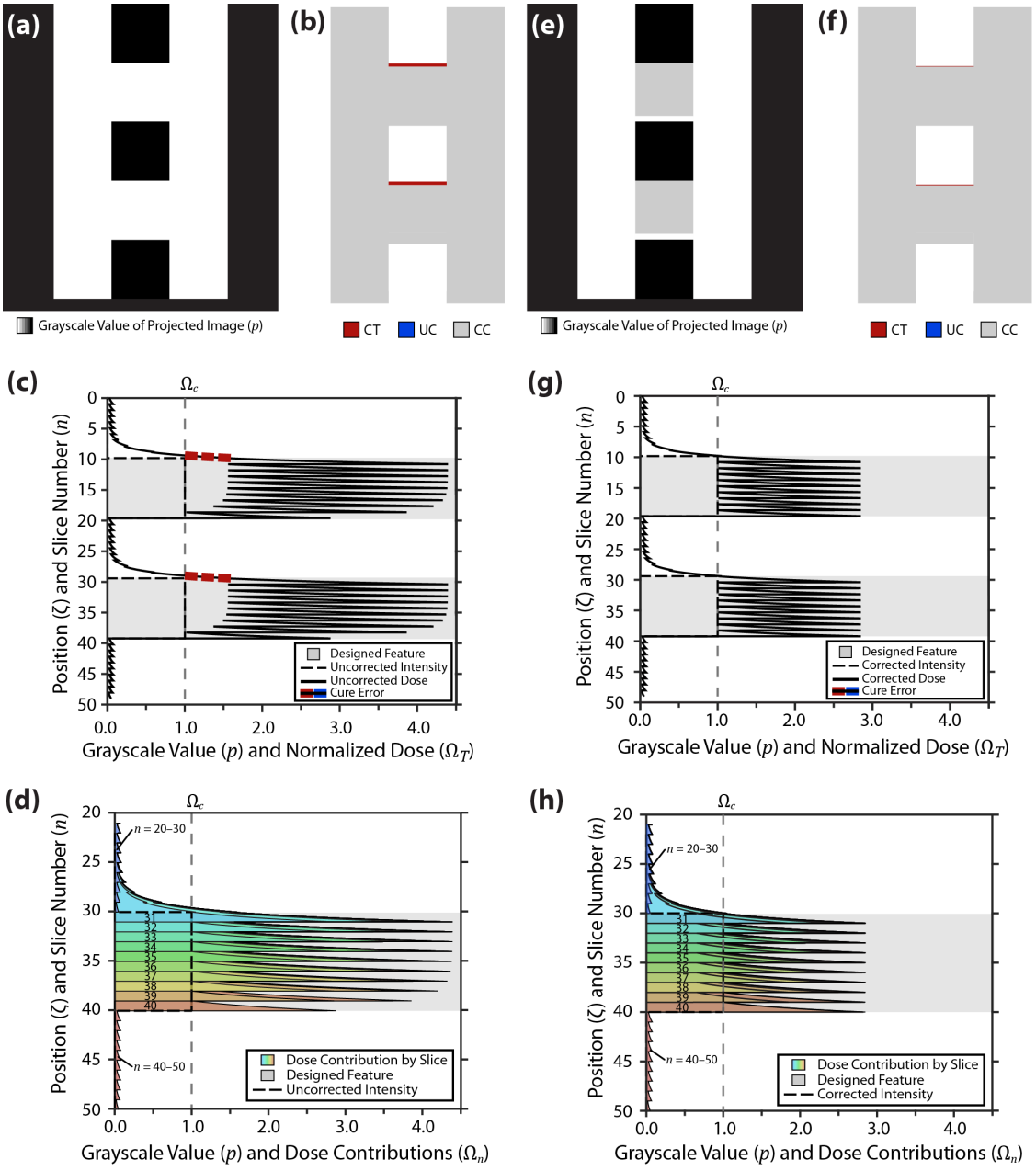

Figure A.7. Layer-by-layer printing of 3D model in Figure 2.2 (a). $D_c = 576\,\mathrm{mJ\,cm^{-3}}$, $h_s = 50\,\mu\mathrm{m}$, $h_a = 110\,\mu\mathrm{m}$, and $s = 1{,}000\,\mathrm{mm\,h^{-1}}$. **(a)** Vertical stack of uncorrected grayscale projections along the plane indicated in Figure 2.2(a). **(b)** Model prediction from slices in (a) showing areas with cure-through (CT, red). Gray regions of the part are correctly cured (CC). **(c)** Grayscale value and dose for the (x, y) position indicated by the dashed line in Figure 2.2(a). **(d)** Contributions of individual slices to the accumulated dose curve shown in (c) for $n = 21$ to $n = 53$. **(e—h)** Results for corrected slices.

of resin and system parameters and can be calculated. The dose at the top and bottom boundaries of the cure-through region is equal to Ω_c, and the projector is at the minimum intensity:

$$\Omega_c = \Phi'_{min} 10^{-\zeta_{CT}\eta} + \Omega_c \, 10^{-\zeta_{CT}\eta} \tag{A.49}$$

$$\zeta_{CT} = \frac{1}{\eta} \log_{10} \left(\frac{\Phi'_{min}}{\Omega_c + 1} \right) \tag{A.50}$$

$$z_{CT} = h_a \log_{10} \left(\frac{I_{min} t_e \ln 10}{D_c h_a} \right) \tag{A.51}$$

If the exposure time is chosen such that the back edge of a feature just reaches the critical dose when exposed at maximum intensity,

$$t_e = \frac{D_c}{I_{max} \, 10^{-h_s h_a^{-1}}} \frac{h_a}{\ln 10} \tag{A.52}$$

$$z_{CT} = h_a \log_{10} \left(\frac{I_{min}}{I_{max}} \, 10^{h_s h_a^{-1}} + 1 \right) \tag{A.53}$$

Thus, the size of the minimum cure-through region in layer-by-layer stereolithography is a function of the resin absorbance height, the layer height, and the projector contrast ratio. The amount of cure-through for a corrected model is reduced by using a high-contrast-ratio projection system and a small layer thickness. Once these parameters are set, the resin absorbance height can be optimized to minimize z_{CT} using Equation A.53. For the parameters used in Figure A.7, $z_{CT} \approx 5\,\mu m$.

Figure A.7 also highlights the dose heterogeneity inherent to non-continuous stereolithography. We can define the degree of dose heterogeneity ω as the ratio of maximum to minimum dose within a layer:

$$\begin{aligned} \omega &= \frac{\Omega_T(\zeta)}{\Omega_T(\zeta) \, 10^{-\eta}} \\ &= 10^{h_s h_a^{-1}} \end{aligned} \tag{A.54}$$

The degree of dose heterogeneity thus increases as the layer height increases and decreases as the absorbance height increases. For the hypothetical resin in Figure A.7, $\omega = 2.848$.

APPENDIX B

Kinetic Curing Model for Uninhibited and Photoinhibited Stereolithography

B.1 Calibration Data for Blue and UV Intensities

Intensity calibration data for the Ember are shown in Figure B.1. Calibration data for the characterization of Custom Resin 1 are shown in Figure B.2; calibration data for the characterization of Custom Resin 2 is available in Ref. [18].

B.2 Comparing Volume- and Area-Based Dose Models

Optical dose is generally given units of energy per unit area (e.g., $\mathrm{mJ\,cm^{-2}}$); however, a volumetric dose with units of energy per unit volume (e.g., $\mathrm{mJ\,cm^{-3}}$) is sometimes appropriate. This is often the case for photopolymerization-based 3D printing, where volumes of material are exposed and the energy absorbed per unit volume seems an apt metric (note that the historical use of optical dose is in applications where there is no appreciable attenuation of light intensity through the exposed medium, such as photography and thin-film photolithography). In the model presented, we have used the area-based dose because we generally found that the critical areal dose (the threshold for curing) remains constant as nonreactive light absorbers are added to the formulation while the critical volumetric dose does not. Since the critical dose is used as a measure of reactivity, not light attenuation, we believe this

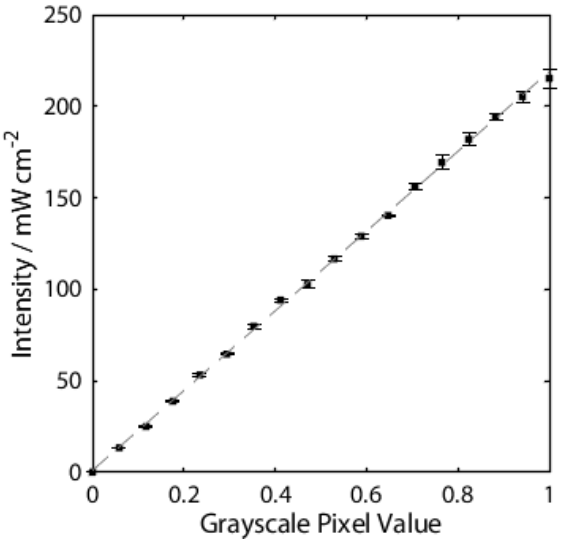

Figure B.1. Incident UV intensity versus grayscale value for the Ember 3D printer. The grayscale value for a given pixel is defined as the `[R,G,B]`/255 where `R` = `G` = `B`. $p = 1$ corresponds to white, and $p = 0$ corresponds to black.

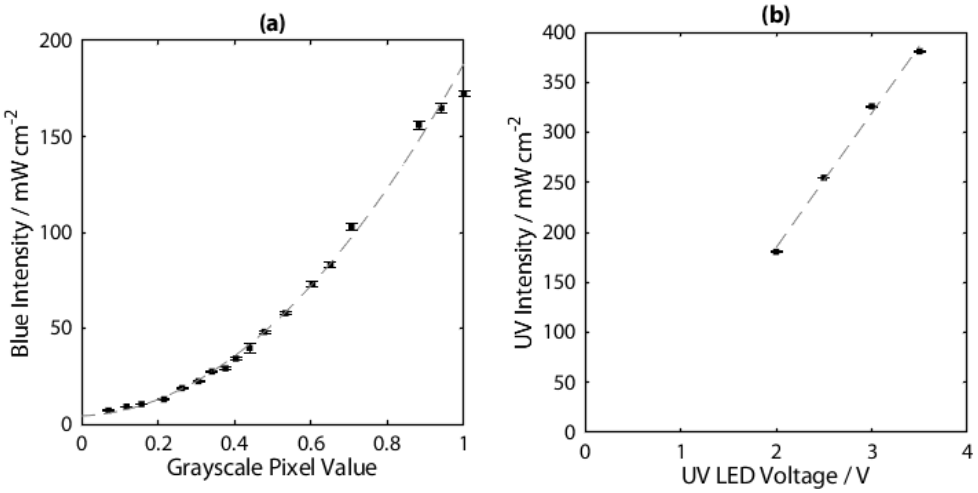

Figure B.2. Calibration data for blue and UV intensities for the two-color printer. While lines of best fit are included, only points where the intensity was explicitly measured were used in characterization experiments. **(a)** Incident blue intensity, $I_{b,0}$, versus grayscale value, p. The grayscale value for a given pixel is defined as the `[R,G,B]`/255 where `R` = `G` = `B`. $p = 1$ corresponds to white, and $p = 0$ corresponds to black. **(b)** Incident UV intensity, $I_{uv,0}$, versus analog control voltage, V_{uv}.

choice is appropriate for the comparisons made in this work. Below, we present volumetric forms of the key equations, where the subscript A indicates an areal variable and the subscript V indicates a volumetric variable.

For the uninhibited model:

$$D'_A(z) = \left(I_0 e^{-z/h_a}\right)^m t \tag{B.1}$$

$$D'_V(z) = \left(I_0 h_a^{-1} e^{-z/h_a}\right)^m t \tag{B.2}$$

$$z_c = \frac{h_a}{m} \ln\left(\frac{I_0^m t}{D'_{A,c}}\right) \tag{B.3}$$

$$z_c = \frac{h_a}{m} \ln\left[\frac{(I_0 h_a^{-1})^m t}{D'_{V,c}}\right] \tag{B.4}$$

For the photoinhibited model:

$$D'_A(z) = \left(I_{b,0} e^{-z/h_b} - \beta I_{uv,0} e^{-z/h_{uv}}\right)^m t \tag{B.5}$$

$$D'_V(z) = \left(I_{b,0} h_b^{-1} e^{-z/h_b} - \beta I_{uv,0} h_{uv}^{-1} e^{-z/h_{uv}}\right)^m t \tag{B.6}$$

Thus,

$$D'_{V,c} = \frac{D'_{A,c}}{h_b^m} \qquad \beta_V = \frac{h_{uv}}{h_b}\beta_A \tag{B.7}$$

B.3 Initiation Point in Photoinhibited Resin

The time and position at which curing initiates in the photoinhibited system can be determined from the dose equation. After rearranging Equation 3.22 to solve for the time at which a point reaches the critical dose, the initiation point is the minimum of this equation—the minimum time at which any resin has gelled.

$$D'_c = \left(I_{b,0} e^{-z_c/h_b} - \beta I_{uv,0} e^{-z_c/h_{uv}}\right)^m t \tag{B.8}$$

$$t(z_c) = D'_c \left(I_{b,0} e^{-z_c/h_b} - \beta I_{uv,0} e^{-z_c/h_{uv}}\right)^{-m} \tag{B.9}$$

$$\frac{\partial t}{\partial z_c} = mD_c' \left(I_{b,0}e^{-z_c/h_b} - \beta I_{uv,0}e^{-z_c/h_{uv}}\right)^{-(m+1)} \times \left(I_{b,0}h_b^{-1}e^{-z_c/h_b} - \beta I_{uv,0}h_{uv}^{-1}e^{-z_c/h_{uv}}\right) = 0 \tag{B.10}$$

Equation B.10 has three solutions. The first parenthetical term is equal to zero for $z_c \to \infty$ and at the steady-state dead zone position $z_{f,\infty}$; the second parenthetical term is equal to zero for $z_c \to \infty$ and at the initiation point z_0. Thus,

$$z_0 = \frac{\ln\left(\frac{\beta I_{uv,0}h_{uv}^{-1}}{I_{b,0}h_b^{-1}}\right)}{h_{uv}^{-1} - h_b^{-1}} \tag{B.11}$$

t_0 can subsequently be found by substituting Equation B.11 back into Equation B.9. The initiation point, then, is found to depend on the intensity ratio (rather than the independent values of I_b and I_{uv}), the inhibition constant, and the blue and UV absorbance heights. Comparing the equation for the initiation point (Equation B.11) with that for the steady-state dead zone (Equation 3.25), their similarity is apparent. In fact,

$$z_0 = z_{f,\infty} + \ln\left(\frac{h_b}{h_{uv}}\right) \tag{B.12}$$

This relationship is clear when the two quantities are plotted, as shown in Figure B.3.

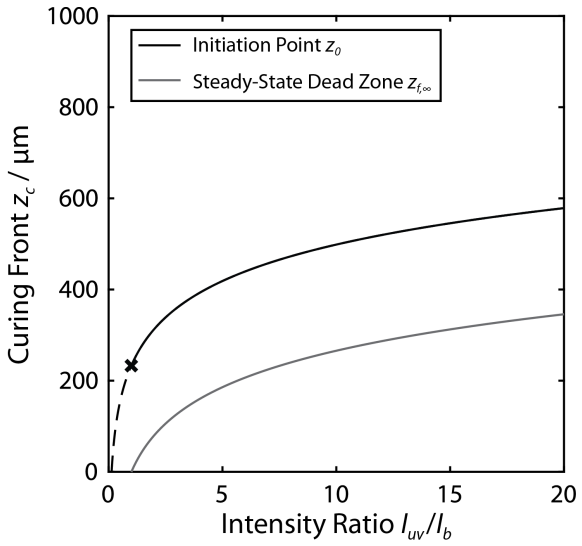

Figure B.3. Comparing initiation point z_0 and steady-state dead zone $z_{f,\infty}$ in photoinhibited model. Note that below the intensity ratio where $z_{f,\infty} = 0$ (also indicated by **x** on the z_0 line), no dead zone exists, and continuous printing is thus not possible.

APPENDIX C

Resin Flow and Dead Zone Uniformity in Photoinhibited Continuous Stereolithography

C.1 Materials and Methods for Two-Color Continuous Printing

C.1.1 Materials

Resin for two-color continuous 3D printing was formulated as a mixture of oligomer, reactive diluent, initiator, inhibitor, and light absorbers, with a composition given in Table C.1. The oligomer used was a proprietary acrylate blend CN991 (Sartomer), with 1,6-hexanedioldiacrylate (HDDA, TCI America) as a reactive diluent. DL-Camphorquinone (CQ, Fisher Scientific) and ethyl 4-(dimethylamino)benzoate (EDAB, ACROS Organics) were used as the blue-light initiator and co-initiator, respectively. 2,2'-Bis(2-chlorophenyl)-4,4',5,5'-tetraphenyl-1,2'-biimidazole (*o*-Cl-HABI, Hampford Research Inc.) was used as the UV-light inhibitor. Resins were prepared by dissolving CQ, EDAB, and *o*-Cl-HABI in a small amount of tetrahydrofuran (THF, ACROS Organics) and combining with the oligomer and reactive diluent. Solvent was removed by evaporation under airflow followed by degassing under vacuum. Uncured resin is rinsed away in cured height and dead zone experiments using isopropanol (IPA, laboratory grade, Fisher Scientific).

Parameters in the resin curing model (Equation 4.1) were determined via cured height and dead zone height characterization experiments. Methods for these have

Table C.1. Resin formulation.

Component	Function	Concentration (wt.%)
CQ	photoinitiator	1.9
EDAB	co-initiator	0.94
o-Cl HABI	photoinhibitor	2.8
Tinuvin 328	UV absorber	0.46
Epolight 5675	blue light absorber	0.004
CN991	oligomer	55.7
HDDA	reactive diluent	37.2

been described elsewhere (see Chapter III or Refs. [15, 18]). For the resin used in this work, $D_c' = 64\,(\mathrm{mW\,cm^{-2}})^{0.99}\,\mathrm{s}$, $h_b = 408\,\mu\mathrm{m}$, $\beta = 0.73$, $h_{uv} = 37.8\,\mu\mathrm{m}$, and $m = 0.99$.

C.1.2 Two-Color 3D Printing

Two-color continuous stereolithography was performed using a previously described custom 3D printer [15]. Blue light is produced from a DLP projector (Optoma ML750), which has been modified by removing the red and green channels. UV light is produced from a light emitting diode (Thorlabs, M365LP1) and passes through an adjustable collimation adapter (Thorlabs, SM2F) and an aspheric condenser lens (Thorlabs, ACL50832U). Blue and UV light is superimposed using a longpass dichroic mirror (Thorlabs, DMLP425L), and the setup is controlled using a custom LabVIEW virtual instrument.

C.1.3 Calibration Data for Blue and UV Intensities

Intensity calibration data for the two-color printer is shown in Figure C.1. For each light source, a calibration curve for incident light intensity was produced using a digital radiometer (International Light Technologies, ILT2400) with a UV-Vis GaAsP detector (International Light Technologies, SED005/U) and a 10× attenuation filter (International Light Technologies, QNDS2). Blue intensity (460 nm) was calibrated

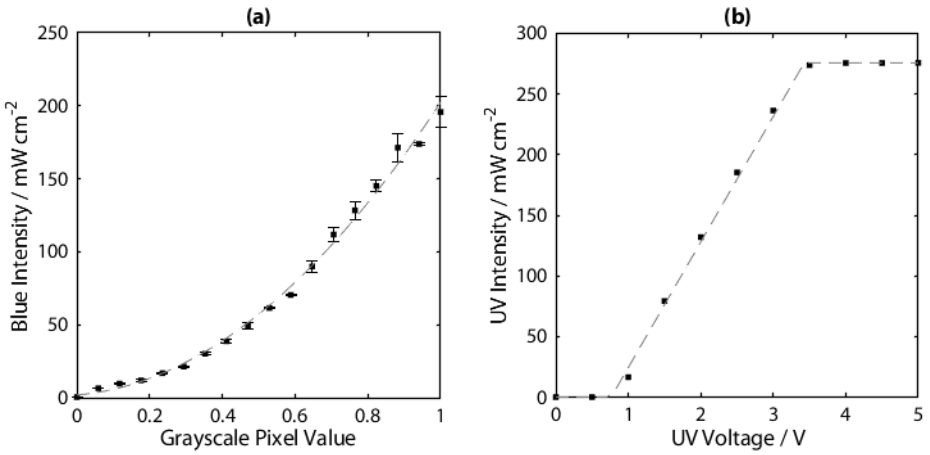

Figure C.1. Calibration data for blue and UV intensities for the two-color printer. **(a)** Incident blue intensity, $I_{b,0}$, versus grayscale value, p. The grayscale value for a given pixel is defined as $[\mathtt{R}, \mathtt{G}, \mathtt{B}]/255$ where $\mathtt{R} = \mathtt{G} = \mathtt{B}$. $p = 1$ corresponds to white, and $p = 0$ corresponds to black. **(b)** Incident UV intensity, $I_{uv,0}$, versus analog control voltage, V_{uv}.

as a function of grayscale pixel value and LED input voltage, and UV intensity (365 nm) was calibrated as a function of LED input voltage.

C.2 Separation Force and Build Platform Position

If the Stefan Equation (Equation 4.6) describes the separation force between a surface and the window, the force scales with $R^4 h^{-3}$. Thus as the build platform rises, the separation force between the build platform and the window decreases. At a certain point, the forces resulting from the part radius and dead zone height become more significant than forces resulting from the build platform radius and build platform position:

$$\frac{-3\pi\mu S R_p^4}{2z_f^3} \geq \frac{-3\pi\mu S R_{BP}^4}{2z_{BP}^3} \tag{C.1}$$

$$z_{BP} \geq \left(\frac{R_{BP}^4}{R_p^4/z_f^3}\right)^{1/3} \tag{C.2}$$

The gap between the build platform and window (z_{BP}) at which these forces are equal is shown in Figure C.2 assuming a dead zone height z_f of 100 µm.

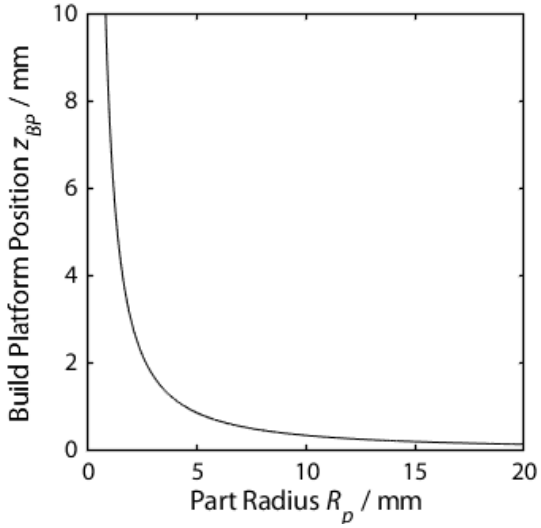

Figure C.2. Gap between the build platform and window at which forces resulting from the part radius and dead zone height become more significant than forces resulting from the build platform radius and build platform position. $R_{BP} = 25\,\text{mm}$ and $z_f = 100\,\mu\text{m}$.

C.3 Dead Zone Calculations

To calculate the average dead zone height (shown in Figure 4.3), results are extracted from COMSOL and analyzed in MATLAB. D' data is extracted from COMSOL on an interpolated $5\,\mu\text{m}$ grid at the desired time point, and the MATLAB function `contourc` is used to interpolate the coordinates of the $D' = D'_c$ contour (i.e., the curing front). Along the contour, the partial derivatives of dose $\partial D'/\partial r$ and $\partial D'/\partial z$ are extracted from COMSOL. These partial derivatives are then used to find the angle of the gradient vector, which is normal to the contour line:

$$\theta = \arctan\left|\frac{\partial D'/\partial z}{\partial D'/\partial r}\right| \tag{C.3}$$

Points on the contour with $\theta \leq 10^\circ$ are classified as part of the dead zone. This threshold was chosen to give results similar to those that result from manual analysis. The average and standard deviation of the z-coordinates for these points are taken and are the values that appear in Figure 4.3 and C.3.

This method is imperfect: it sometimes ignores regions that should clearly be

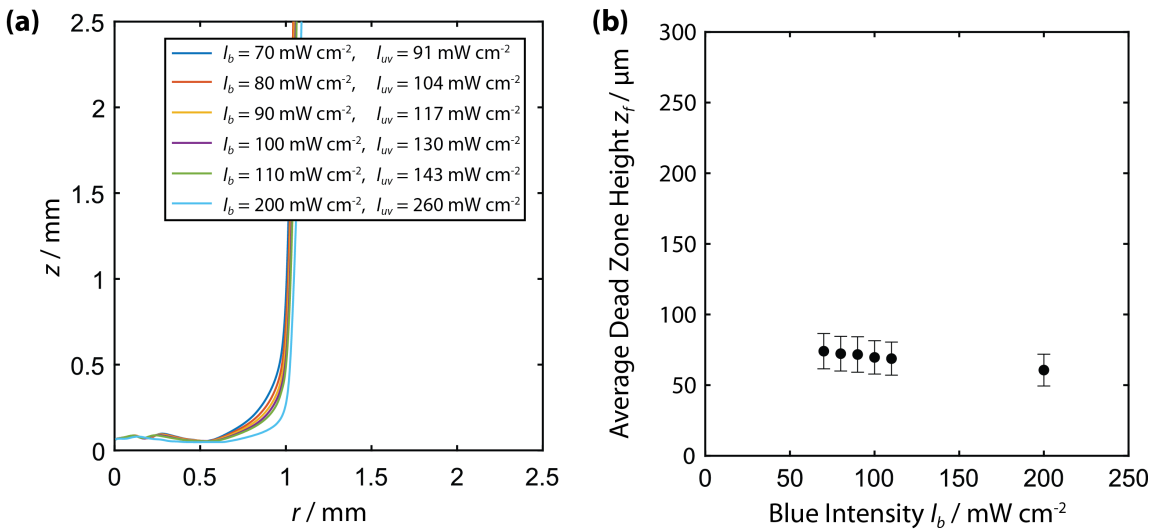

Figure C.3. Curing front position with varying blue and UV intensity at constant intensity ratio. The overall shape and uniformity of the curing front is affected by blue (and UV) intensity, even as the intensity ratio is held constant. Other parameters are held constant at $S = 300\,\mathrm{mm\,h^{-1}}$ and $R_p = 1\,\mathrm{mm}$. The curing front is identified as the $D' = D'_c$ contour. Error bars indicate dead zone uniformity and are calculated as the standard deviation of z-coordinate values for points in the dead zone curing front (see Appendix C.3). **(a)** Curing front and **(b)** average dead zone height for varying blue and UV intensities at a constant ratio of $I_{uv}/I_b = 1.3$.

considered part of the dead zone, and the ambiguous curved edge region does not offer clear cutoff points even if done manually. However, we have found this approach to generally agree with "eyeball" analyses of the curing front images.

C.4 Effect of Blue Intensity on Curing Front Profile at Constant Intensity Ratio

Figure C.3 shows the effect of changing I_b and I_{uv} together at a constant ratio of $I_{uv}/I_b = 1.3$. The effect on the dead zone uniformity is minor overall. While curvature on the edge of the part is reduced as the intensities increase, the dead zone from the center to the beginning of the curved edge does not change significantly, even as the intensities are doubled to $I_b = 200\,\mathrm{mW\,cm^{-2}}$ and $I_{uv} = 260\,\mathrm{mW\,cm^{-2}}$. As shown in Figure C.3(b), even as the average dead zone height slightly decreases (due primarily to flattening at the edge), the standard deviation (i.e., uniformity) remains consistent.

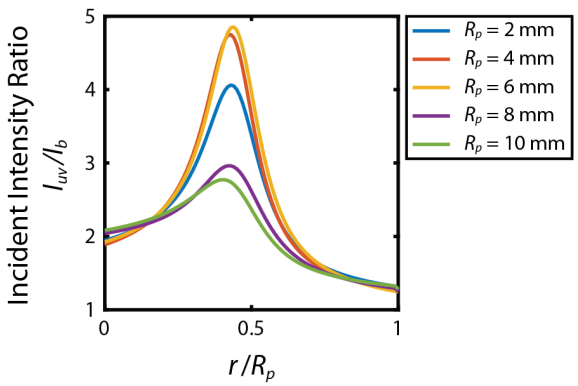

Figure C.4. UV/Blue intensity ratio for variable I_b and I_{uv} optimization. While the shape of the blue and UV intensity functions is similar and the functions for each part radius appear nearly identical, the intensity ratio is not constant with r/R_p, and the intensity ratio function varies for different part radii.

C.5 Intensity Ratio for Variable Blue/Variable UV Optimization

Although the similar curve shapes for the variable blue and UV intensity functions (Figure 4.4(c)) suggest that the UV/blue intensity ratio I_{uv}/I_b might remain constant throughout the part, it in fact varies considerably (Figure C.4); furthermore, the peak intensity ratio ranges from approximately 2.8 for $R_p = 10\,\text{mm}$ to 4.9 for $R_p = 6\,\text{mm}$. The latter effect may be an artifact of imperfect optimization since there is no clear trend in the peak intensity ratio as part radius increases and the differences among the actual intensity curves are quite small. However, the former effect (variation within parts) persists across part radii, with each intensity ratio curve having a similar form.

C.6 Rectangular Symmetry Optimization Model

The rectangular symmetry optimization model, shown in Figure C.5(b), is identical to the axisymmetric steady-state optimization model (Figure 4.1(c)) except that it uses a line of rectangular symmetry rather than radial symmetry. The model is thus assumed to extend infinitely along the axis normal to the simulation cross-

section (i.e., out of the page). While the axisymmetric model is useful for simulating parts or features with a circular (or approximately circular) cross-section, this model is appropriate for parts or features where one dimension of the cross-section is significantly longer than the other.

Figure C.5(c) shows the optimized intensity functions for a 10 mm half-width cross-section (variable blue/constant UV); the resulting dose at the part outlet for these optimized intensities is shown in Figure C.5(d). Figure C.5(e) shows the exposure image resulting from the optimized intensity profile. Compared to the axisymmetric model constrained to variable blue and constant UV (Figure 4.4(b)), the rectangular symmetry model achieves better dead zone uniformity overall—particularly near the center ($x = 0$ or $r = 0$). Since the current printer setup is not ideal for parts with a high aspect ratio cross-section (those where the rectangular symmetry model is most applicable), an image such as that shown in Figure C.5(f), in which the ends are replaced with the optimized axisymmetric intensity function, might be more appropriate for print tests.

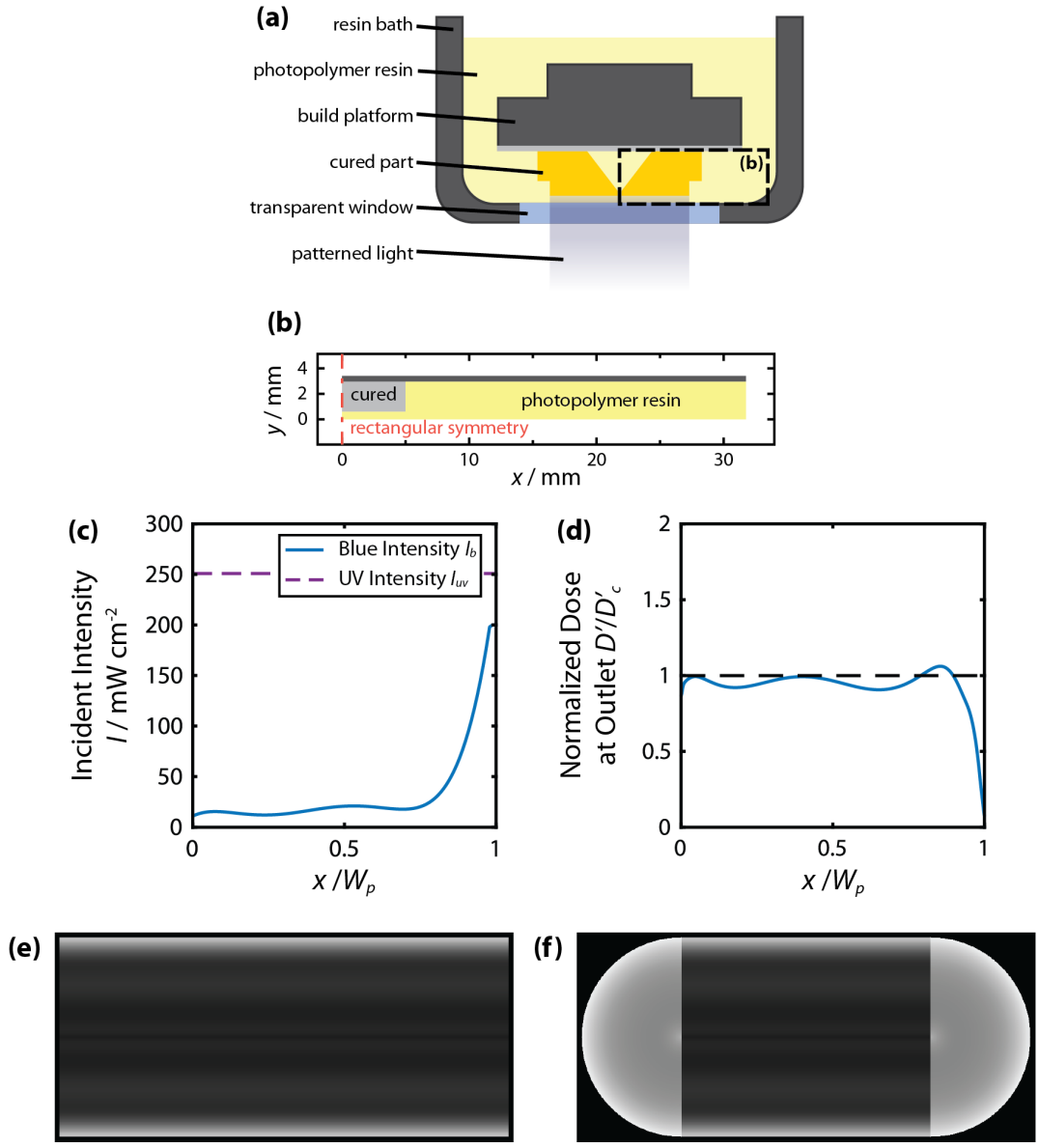

Figure C.5. Geometry and optimization results for rectangular symmetry model. **(a)** Diagram of two-color continuous stereolithography. Dashed lines indicate the region of the resin bath included in the COMSOL geometry. **(b)** Geometry for the steady-state, rectangular symmetry model, which is used for intensity optimization. **(c)** Optimized blue and UV intensity for a 10 mm half-width cross-section (W_p). The incident blue intensity is allowed to vary with x and is capped at 200 mW cm^{-2}; the incident UV intensity is constant and is capped at 275 mW cm^{-2}. **(d)** Dose at the part outlet normalized to the critical dose for the optimization in (c). **(e)** Image generated from optimized intensity function in (c). **(f)** Proposed combination of cylindrical and rectangular solutions to ensure curing of edges.

BIBLIOGRAPHY

BIBLIOGRAPHY

[1] ASTM International, "ISO/ASTM52900-15 Standard Terminology for Additive Manufacturing – General Principles – Terminology," 2015.

[2] ASME, "Stereolithography: The First 3D Printing Technology," tech. rep., The American Society of Mechanical Engineers, 2016.

[3] C. W. Hull, "Apparatus for Production of Three-Dimensonal Objects By Stereolithography," 1984.

[4] C. R. Deckard, "Method and Apparatus for Producing Parts by Selective Sintering," 1989.

[5] S. S. Crump, "Apparatus and Method for Creating Three-Dimensional Objects," 1992.

[6] A. Bertsch, S. Zissi, J. Y. Jézéquel, S. Corbel, and J. C. André, "Microstereophotolithography using a liquid crystal display as dynamic mask-generator," *Microsystem Technologies*, vol. 3, pp. 42–47, Feb. 1997.

[7] C. Sun, N. Fang, D. M. Wu, and X. Zhang, "Projection micro-stereolithography using digital micro-mirror dynamic mask," *Sensors and Actuators, A: Physical*, vol. 121, pp. 113–120, May 2005.

[8] Y.-M. Huang and C.-P. Jiang, "On-line force monitoring of platform ascending rapid prototyping system," *Journal of Materials Processing Technology*, vol. 159, pp. 257–264, Jan. 2005.

[9] Y. Pan, C. Zhou, and Y. Chen, "A Fast Mask Projection Stereolithography Process for Fabricating Digital Models in Minutes," *Journal of Manufacturing Science and Engineering*, vol. 134, pp. 1–9, Oct. 2012.

[10] F. Liravi, S. Das, and C. Zhou, "Separation force analysis based on cohesive delamination model for bottom-up stereolithography using finite element analysis," in *25th Annual International Solid Freeform Fabrication Symposium*, vol. 1, pp. 1432–1451, 2014.

[11] Y. Pan, H. He, J. Xu, and A. Feinerman, "Study of separation force in constrained surface projection stereolithography," *Rapid Prototyping Journal*, vol. 23, pp. 353–361, Mar. 2017.

[12] J. R. Tumbleston, D. Shirvanyants, N. Ermoshkin, R. Janusziewicz, A. R. Johnson, D. Kelly, K. Chen, R. Pinschmidt, J. P. Rolland, A. Ermoshkin, E. T. Samulski, and J. M. DeSimone, "Continuous liquid interface production of 3D objects," *Science*, vol. 347, pp. 1349–1352, Mar. 2015.

[13] A. R. Johnson, C. L. Caudill, J. R. Tumbleston, C. J. Bloomquist, C. Luft, and J. M. Desimone, "Single-Step Fabrication of Computationally Designed Microneedles by Continuous Liquid Interface Production," *PLOS ONE*, vol. 11, no. 9, p. e0162518, 2016.

[14] R. Janusziewicz, J. R. Tumbleston, A. L. Quintanilla, S. J. Mecham, and J. M. Desimone, "Layerless fabrication with continuous liquid interface production," *Proceedings of the National Academy of Sciences*, vol. 113, no. 42, pp. 11703–11708, 2016.

[15] M. P. de Beer, H. L. van der Laan, M. A. Cole, R. J. Whelan, M. A. Burns, and T. F. Scott, "Rapid, continuous additive manufacturing by volumetric polymerization inhibition patterning," *Science Advances*, vol. 5, p. eaau8723, Jan. 2019.

[16] D. A. Walker, J. L. Hedrick, and C. A. Mirkin, "Rapid, large-volume, thermally controlled 3D printing using a mobile liquid interface," *Science*, vol. 366, pp. 360–364, Oct. 2019.

[17] X. Li, H. Mao, Y. Pan, and Y. Chen, "Mask Video Projection-Based Stereolithography With Continuous Resin Flow," *Journal of Manufacturing Science and Engineering*, vol. 141, Aug. 2019.

[18] M. P. de Beer, *Advances in Additive Manufacturing and Microfabrication*. PhD thesis, University of Michigan, 2020.

[19] D. Dendukuri, P. Panda, R. Haghgooie, J. M. Kim, T. A. Hatton, and P. S. Doyle, "Modeling of Oxygen-Inhibited Free Radical Photopolymerization in a PDMS Microfluidic Device," *Macromolecules*, vol. 41, pp. 8547–8556, Nov. 2008.

[20] T. F. Scott, B. A. Kowalski, A. C. Sullivan, C. N. Bowman, and R. R. McLeod, "Two-Color Single-Photon Photoinitiation and Photoinhibition for Subdiffraction Photolithography," *Science*, vol. 324, pp. 913–917, May 2009.

[21] H. L. van der Laan, M. A. Burns, and T. F. Scott, "Volumetric Photopolymerization Confinement through Dual-Wavelength Photoinitiation and Photoinhibition," *ACS Macro Letters*, vol. 8, pp. 899–904, Aug. 2019.

[22] Z. D. Pritchard, M. P. de Beer, R. J. Whelan, T. F. Scott, and M. A. Burns, "Modeling and Correcting Cure-Through in Continuous Stereolithographic 3D Printing," *Advanced Materials Technologies*, vol. 4, p. 1900700, Dec. 2019.

[23] T. D. Ngo, A. Kashani, G. Imbalzano, K. T. Nguyen, and D. Hui, "Additive manufacturing (3D printing): A review of materials, methods, applications and challenges," *Composites Part B: Engineering*, vol. 143, pp. 172–196, June 2018.

[24] O. Oderinde, S. Liu, K. Li, M. Kang, H. Imtiaz, F. Yao, and G. Fu, "Multifaceted polymeric materials in three-dimensional processing (3DP) technologies: Current progress and prospects," *Polymers for Advanced Technologies*, vol. 29, pp. 1586–1602, June 2018.

[25] R. D. Pedde, B. Mirani, A. Navaei, T. Styan, S. Wong, M. Mehrali, A. Thakur, N. K. Mohtaram, A. Bayati, A. Dolatshahi-Pirouz, M. Nikkhah, S. M. Willerth, and M. Akbari, "Emerging Biofabrication Strategies for Engineering Complex Tissue Constructs," *Advanced Materials*, vol. 29, p. 1606061, May 2017.

[26] A. K. Gaharwar, L. M. Cross, C. W. Peak, K. Gold, J. K. Carrow, A. Brokesh, and K. A. Singh, "2D Nanoclay for Biomedical Applications: Regenerative Medicine, Therapeutic Delivery, and Additive Manufacturing," June 2019.

[27] K. Kim, B. Kim, and C. H. Lee, "Printing Flexible and Hybrid Electronics for Human Skin and Eye-Interfaced Health Monitoring Systems," *Advanced Materials*, vol. 32, p. 1902051, Apr. 2020.

[28] D. Cao, Y. Xing, K. Tantratian, X. Wang, Y. Ma, A. Mukhopadhyay, Z. Cheng, Q. Zhang, Y. Jiao, L. Chen, and H. Zhu, "3D Printed High-Performance Lithium Metal Microbatteries Enabled by Nanocellulose," *Advanced Materials*, vol. 31, p. 1807313, Apr. 2019.

[29] D. Shahriari, G. Loke, I. Tafel, S. Park, P. H. Chiang, Y. Fink, and P. Anikeeva, "Scalable Fabrication of Porous Microchannel Nerve Guidance Scaffolds with Complex Geometries," *Advanced Materials*, vol. 31, p. 1902021, July 2019.

[30] Y. Yang, X. Song, X. Li, Z. Chen, C. Zhou, Q. Zhou, and Y. Chen, "Recent Progress in Biomimetic Additive Manufacturing Technology: From Materials to Functional Structures," *Advanced Materials*, vol. 30, p. 1706539, Sept. 2018.

[31] A. Velasco-Hogan, J. Xu, and M. A. Meyers, "Additive Manufacturing as a Method to Design and Optimize Bioinspired Structures," *Advanced Materials*, vol. 30, p. 1800940, Dec. 2018.

[32] G. Etienne, I. L. H. Ong, and E. Amstad, "Bioinspired Viscoelastic Capsules: Delivery Vehicles and Beyond," *Advanced Materials*, vol. 31, p. 1808233, July 2019.

[33] R. D. Farahani, M. Dubé, and D. Therriault, "Three-Dimensional Printing of Multifunctional Nanocomposites: Manufacturing Techniques and Applications," July 2016.

[34] L. Hirt, A. Reiser, R. Spolenak, and T. Zambelli, "Additive Manufacturing of Metal Structures at the Micrometer Scale," *Advanced Materials*, vol. 29, p. 1604211, May 2017.

[35] H. Wang, J. Shen, D. J. Kline, N. Eckman, N. R. Agrawal, T. Wu, P. Wang, and M. R. Zachariah, "Direct Writing of a 90 wt% Particle Loading Nanothermite," *Advanced Materials*, vol. 31, p. 1806575, June 2019.

[36] D. W. Yee, M. L. Lifson, B. W. Edwards, and J. R. Greer, "Additive Manufacturing of 3D-Architected Multifunctional Metal Oxides," *Advanced Materials*, vol. 31, p. 1901345, Aug. 2019.

[37] W. Yang, J. Yang, J. J. Byun, F. P. Moissinac, J. Xu, S. J. Haigh, M. Domingos, M. A. Bissett, R. A. Dryfe, and S. Barg, "3D Printing of Freestanding MXene Architectures for Current-Collector-Free Supercapacitors," *Advanced Materials*, vol. 31, p. 1902725, Sept. 2019.

[38] N. Kleger, M. Cihova, K. Masania, A. R. Studart, and J. F. Löffler, "3D Printing of Salt as a Template for Magnesium with Structured Porosity," *Advanced Materials*, vol. 31, p. 1903783, Sept. 2019.

[39] M. Ratto and R. Ree, "Materializing information: 3D printing and social change," *First Monday*, vol. 17, July 2012.

[40] J. Choi, R. B. Wicker, S.-H. Cho, C.-S. Ha, and S.-h. Lee, "Cure depth control for complex 3D microstructure fabrication in dynamic mask projection microstereolithography," *Rapid Prototyping Journal*, vol. 15, pp. 59–70, Jan. 2009.

[41] P. F. O'Neill, N. Kent, and D. Brabazon, "Mitigation and control of the overcuring effect in mask projection micro-stereolithography," in *AIP Conference Proceedings*, vol. 200012, p. 200012, 2017.

[42] A. I. Shallan, P. Smejkal, M. Corban, R. M. Guijt, and M. C. Breadmore, "Cost-effective three-dimensional printing of visibly transparent microchips within minutes," *Analytical Chemistry*, vol. 86, pp. 3124–3130, Mar. 2014.

[43] A. S. Limaye and D. W. Rosen, "Compensation zone approach to avoid print-through errors in mask projection stereolithography builds," *Rapid Prototyping Journal*, vol. 12, pp. 283–291, Oct. 2006.

[44] H. Gong, M. Beauchamp, S. Perry, A. T. Woolley, and G. P. Nordin, "Optical approach to resin formulation for 3D printed microfluidics," *RSC Advances*, vol. 5, no. 129, pp. 106621–106632, 2015.

[45] H. Gong, B. P. Bickham, A. T. Woolley, and G. P. Nordin, "Custom 3D printer and resin for 18 μm $\times$ 20 μm microfluidic flow channels," *Lab on a Chip*, vol. 17, pp. 2899–2909, Aug. 2017.

[46] S. Zissi, A. Bertsch, J. Y. Jézéquel, S. Corbel, D. J. Lougnot, and J. C. André, "Stereolithography and microtechniques," *Microsystem Technologies*, vol. 2, pp. 97–102, Mar. 1995.

[47] C. Sun and X. Zhang, "Experimental and numerical investigations on microstereolithography of ceramics," *Journal of Applied Physics*, vol. 92, pp. 4796–4802, Oct. 2002.

[48] A. Limaye and D. Rosen, "Process planning method for mask projection microstereolithography," *Rapid Prototyping Journal*, vol. 13, pp. 76–84, Apr. 2007.

[49] M. J. Männel, L. Selzer, R. Bernhardt, and J. Thiele, "Optimizing Process Parameters in Commercial Micro-Stereolithography for Forming Emulsions and Polymer Microparticles in Nonplanar Microfluidic Devices," *Advanced Materials Technologies*, vol. 4, p. 1800408, Jan. 2019.

[50] Z. Wang, H. Liang, and A. V. Dobrynin, "Computer Simulations of Continuous 3-D Printing," *Macromolecules*, vol. 50, pp. 7794–7800, Oct. 2017.

[51] S. Sarkar and S. Lin-Gibson, "Computational Design of Photocured Polymers Using Stochastic Reaction-Diffusion Simulation," *Advanced Theory and Simulations*, vol. 1, p. 1800028, July 2018.

[52] C. Zhou, Y. Chen, and R. A. Waltz, "Optimized Mask Image Projection for Solid Freeform Fabrication," *Journal of Manufacturing Science and Engineering*, vol. 131, pp. 1–12, Dec. 2009.

[53] Creative Tools Sweden AB, "#3DBenchy – The jolly 3D printing torture-test."

[54] A. Nosek, "Easter Eggs by Antonin_Nosek - Thingiverse."

[55] P. F. Jacobs, *Rapid Prototyping & Manufacturing: Fundamentals of Stereolithography*. Dearborn, Michigan: Society of Manufacturing Engineers, 1 ed., 1992.

[56] B. E. Kelly, I. Bhattacharya, H. Heidari, M. Shusteff, C. M. Spadaccini, and H. K. Taylor, "Volumetric additive manufacturing via tomographic reconstruction," *Science*, vol. 363, pp. 1075–1079, Mar. 2019.

[57] G. I. Peterson, J. J. Schwartz, D. Zhang, B. M. Weiss, M. A. Ganter, D. W. Storti, and A. J. Boydston, "Production of Materials with Spatially-Controlled Cross-Link Density via Vat Photopolymerization," *ACS Applied Materials & Interfaces*, vol. 8, pp. 29037–29043, Oct. 2016.

[58] Y. Wang, D. Xue, and D. Mei, "Projection-Based Continuous 3D Printing Process With the Grayscale Display Method," *Journal of Manufacturing Science and Engineering*, vol. 142, pp. 1–10, Feb. 2020.

[59] X. Kuang, J. Wu, K. Chen, Z. Zhao, Z. Ding, F. Hu, D. Fang, and H. J. Qi, "Grayscale digital light processing 3D printing for highly functionally graded materials," *Science Advances*, vol. 5, p. eaav5790, May 2019.

[60] L. M. Leben, J. J. Schwartz, A. J. Boydston, R. J. D'Mello, and A. M. Waas, "Optimized heterogeneous plates with holes using 3D printing via vat photo-polymerization," *Additive Manufacturing*, vol. 24, pp. 210–216, Dec. 2018.

[61] J. W. Wydra, N. B. Cramer, J. W. Stansbury, and C. N. Bowman, "The reciprocity law concerning light dose relationships applied to BisGMA/TEGDMA photopolymers: Theoretical analysis and experimental characterization," *Dental Materials*, vol. 30, pp. 605–612, June 2014.

[62] C. Hofstetter, S. Orman, S. Baudis, and J. Stampfl, "Combining cure depth and cure degree, a new way to fully characterize novel photopolymers," *Additive Manufacturing*, vol. 24, no. August, pp. 166–172, 2018.

[63] J. H. Lee, R. K. Prud'homme, and I. A. Aksay, "Cure depth in photopolymerization: Experiments and theory," *Journal of Materials Research*, vol. 16, no. 12, pp. 3536–3544, 2001.

[64] J. T. Cabral, S. D. Hudson, C. Harrison, and J. F. Douglas, "Frontal Photopolymerization for Microfluidic Applications," *Langmuir*, vol. 20, pp. 10020–10029, Nov. 2004.

[65] K. Taki, "A Simplified 2D Numerical Simulation of Photopolymerization Kinetics and Oxygen Diffusion–Reaction for the Continuous Liquid Interface Production (CLIP) System," *Polymers*, vol. 12, p. 875, Apr. 2020.

[66] J.-t. Lin, D.-c. Cheng, K.-t. Chen, and H.-w. Liu, "Dual-Wavelength (UV and Blue) Controlled Photopolymerization Confinement for 3D-Printing: Modeling and Analysis of Measurements," *Polymers*, vol. 11, p. 1819, Nov. 2019.

[67] P. J. Flory, "Polymerization of Unsaturated Monomers by Free Radical Mechanisms," in *Principles of Polymer Chemistry*, ch. 4, pp. 106–177, Ithaca, NY: Cornell University, 1953.

[68] R. Dessauer, "The Invention of Dylux® Instant-Access Imaging Materials and the Development of HABI Chemistry-A Personal History," in *Advances in Photochemistry* (D. C. Neckers, T. Wolff, and W. S. Jenks, eds.), vol. 28, ch. 4, pp. 129–261, Hoboken, NJ: John Wiley & Sons, Apr. 2005.

[69] M. Atai, M. Ahmadi, S. Babanzadeh, and D. C. Watts, "Synthesis, characterization, shrinkage and curing kinetics of a new low-shrinkage urethane dimethacrylate monomer for dental applications," *Dental Materials*, vol. 23, no. 8, pp. 1030–1041, 2007.

[70] A. Medellin, W. Du, G. Miao, J. Zou, Z. Pei, and C. Ma, "Vat Photopolymerization 3D Printing of Nanocomposites: A Literature Review," *Journal of Micro and Nano-Manufacturing*, vol. 7, Sept. 2019.

[71] A. Naderi, N. Bhattacharjee, and A. Folch, "Digital Manufacturing for Microfluidics," *Annual Review of Biomedical Engineering*, vol. 21, pp. 325–364, June 2019.

[72] A. V. Nielsen, M. J. Beauchamp, G. P. Nordin, and A. T. Woolley, "3D Printed Microfluidics," *Annual Review of Analytical Chemistry*, vol. 13, pp. 45–65, June 2020.

[73] N. A. Chartrain, C. B. Williams, and A. R. Whittington, "A review on fabricating tissue scaffolds using vat photopolymerization," *Acta Biomaterialia*, vol. 74, pp. 90–111, July 2018.

[74] J. W. Halloran, "Ceramic Stereolithography: Additive Manufacturing for Ceramics by Photopolymerization," *Annual Review of Materials Research*, vol. 46, pp. 19–40, July 2016.

[75] J. C. Najmon, S. Raeisi, and A. Tovar, "Review of additive manufacturing technologies and applications in the aerospace industry," in *Additive Manufacturing for the Aerospace Industry*, pp. 7–31, Elsevier, 2019.

[76] Q. Wang, Y. Sun, B. Guo, P. Li, and Y. Li, "CFD analysis and prediction of suction force during the pulling-up stage of the continuous liquid interface production process," *AIP Advances*, vol. 9, no. 1, 2019.

[77] K. W. Morton, *Numerical Solution of Convection-Diffusion Problems*. Boca Raton: CRC Press, 1996.